University of Alberta

Development and application of quantitative iron MRI in multiple sclerosis

by

Andrew James Walsh

A thesis submitted to the Faculty of Graduate Studies and Research in partial fulfillment of the requirements for the degree of

Doctor of Philosophy

Biomedical Engineering

Fall 2013
Edmonton, Alberta

Dedications

To my wife:

Thank you for always being there for me. You are my love and inspiration.

To my parents:

Thank you for supporting me throughout my long academic path. You taught me how to balance work and life and how to strive for excellence. You encouraged me to pursue my interests, even when difficult, and assisted me when you could.

Abstract

Magnetic resonance imaging (MRI) is a valuable imaging modality and is commonplace in diagnosing, evaluating, and understanding the pathobiology of many neurological disorders. Current methods are helpful in the diagnosis of multiple sclerosis (MS) but fail to provide useful longitudinal information. Furthermore, current clinical MRI methods are limited in the research setting for evaluating the breadth of pathophysiology and focus on classical inflammation, demyelination, and gliosis. Techniques that are sensitive to iron have the potential to uncover new features including iron involvement in lesions, neurodegeneration, or altered metabolism. This thesis explores technical aspects of phase imaging and R2* mapping using high field MRI and their utility in evaluating brain iron in MS.

MR phase images are generated through post-processing of gradient echo MRI acquisitions. Measurements from phase images using a standard high pass method could be used to locally quantify iron which is of interest in MS. However measurements in deep grey matter can be influenced by several factors including filter strength, structure shape, and location of background measurement. These factors were assessed in simulation and in control subjects and the best parameters are suggested.

A new phase processing method is presented which uses the derivative of the spatial gradient to locally correct background phase. The contrast from lesions in MS patients was improved and less filtering effects were apparent in deep grey matter and in simulation.

The contribution from tissue iron to quantitative MRI measurements is unclear, especially in neurological disorders. The relationship between iron staining and MRI

relaxation and phase measurements in postmortem subjects is evaluated where R2* mapping demonstrated the highest correlation to iron compared to R2 mapping, fast spin echo imaging, and phase imaging. Furthermore, a single MRI method could not consistently demonstrate the iron status of MS lesions.

A wide variation in normal brain iron content presents difficulties in establishing pathological iron changes in individual MS patients therefore longitudinal analysis of iron sensitive MRI was assessed. Changes relative to controls were found in several deep grey matter regions which strongly correlate to physical disability.

Acknowledgements

Thank you Dr. Alan Wilman for being such a fantastic supervisor and great supporter. You are truly special and are willing to go the extra mile for students. I not only gained in-depth technical MRI knowledge from you but learned broader aspects of how to conduct excellent research.

I would like to express my appreciate to Dr. Derek Emery for his guidance throughout my PhD and for his ongoing encouragement. Thank you for teaching me about clinical radiology and how to be an effective researcher.

Thank you Dr. Gregg Blevins for teaching me about multiple sclerosis. The projects that I worked on would not have been a success without your ongoing commitment.

Dr. Kenneth Warren and Ingrid Katz have a long and distinguished history of research at the University of Alberta and it was my privilege to work with Dr. Warren on some of his final projects. Thank you for teaching me about multiple sclerosis pathology.

Thank you Dr. Edward Johnson and Dr. Jian-Qiang Lu for contributing their neuropathology expertise to various projects. Your knowledge of neuropathology is truly exemplary.

I appreciate the help from Peter Seres and Karim Damji in teaching me how to operate and troubleshoot various MRI systems in the Peter S. Allen MR Research Centre.

Thank you to the various graduate students in Dr. Wilman's lab and the BME department for allowing me to bounce ideas around and for the thought provoking

discussions.

Thank you to Cassandra Hirt and Cathy Walsh for their editorial expertise and advice.

I would like to thank all of the volunteer subjects and patients with multiple sclerosis who donated their time. Without their assistance, my research would not be possible.

Table of Contents

List of Tables

List of Figures

List of Symbols

a	distance to sphere center	6
APC	antigen presenting cells	25
ATP	adenosientriphosphate	38
B	magnetic field	6
B_0	main magnetic field strength	4
B_1	RF transmit magnetization	12
$\text{base}_{\text{const}}$	baseline constant	65
base_{i}	baseline internal	65
BBB	blood brain barrier	25
BFG	background field gradient	14
BVEC	brain vascular endothelial cell	37
CAUD	caudate nucleus	33
CD	cluster of differentiation glycoprotein	25
CNR	contrast to noise ratio	16
CNS	central nervous system	22
CSF	cerebrospinal fluid	23
DMT1	divalent metal transporter	37
d	water diffusion coefficient	8
EAE	experimental autoimmune encephalomyelitis	36
$\text{edge}_{\text{const}}$	edge constant- of phase grey matter	65
edge_{i}	inner edge - of phase grey matter	65
EDSS	Kurtzke expanded disability status scale	22
FDG	fludeoxyglucose	36
FDRI	field dependent relaxation imaging	18
FLAIR	fluid attenuated inversion recovery	17
fMRI	functional magnetic resonance imaging	35
FOV	field of view	10
FT	fourier transform	16
G	linear magnetic gradient strength in mT/m	10
G_c	autocorrelation function	2
GABA	gamma-aminobutyric acid	36

RN red nucleus 33
ROI region of interest 61
ROS reactive oxygen species 42
RRMS relapsing remitting multiple sclerosis 22
S signal in rotating reference frame 10
SAR specific absorption rate 10
SE spin echo 10
SHARP sophisticated harmonic artifact reduction for phase data 17
SNc substantia nigra pars reticulata 31
SNr substantia nigra pars compacta 31
SNR signal to noise ratio 10
SPMS secondary progressive multiple sclerosis 22
STEAM stimulated echo acquisition mode for imaging 18
STN subthalamic nucleus 31
SWI susceptibility weighted imaging 17
T_1 longitudinal relaxation time 2
T_2 irreversible transverse relaxation time 2
T_2' reversible transverse relaxation time 4
$T_2^\star$ total transverse relaxation time 2
TE echo time 11
$\mathrm{Tf_r}$ transferin receptor 37
Th T helper cell 25
Thal thalamus 33
TNF tumor necrosis factor 26
TR repetition time 11
v volume of spheres 4
V total volume 4
VA ventral anterior nucleus 31
VL ventral lateral nucleus 31
VM ventral medial nucleus 31
w frequency 2
w_r frequency at surface of ferritin sphere 8
Wd K-space window function 16
α flip angle 11
χ susceptibility 4
γ gyromagnetic ratio 4
$\hbar$ Planck's constant 4
τ time 2

τ_c	correlation time	2
θ	phase angle	6

Chapter 1

Introduction

1.1 Overview

Magnetic resonance imaging (MRI) is an essential tool in both the clinical setting and for medical research purposes. It allows a non-invasive approach to uncovering various features of the human body, both structurally and functionally, which would otherwise be undetectable. MRI is especially useful for neuroimaging where soft tissue contrast is unparalleled.

Multiple sclerosis (MS) is a disease that affects the central nervous system with features of inflammation, demyelination, and neuronal degeneration. This disease is particularly difficult to study because animal models are limited and human tissue is difficult to obtain. MRI is a useful tool to investigate this disease because various contrast mechanisms can be exploited to evaluate different pathological processes. Brain iron is of particular interest because it may contribute to disease progression and may be a biomarker of disability.

This thesis includes a collection of four papers that investigate iron sensitive MRI methods and their use in MS. The papers represent a logical evolution from improvement on existing imaging techniques, establishing their ability to image iron in MS, and application of these methods to longitudinally evaluate iron in a patient study. An introductory chapter explains necessary background information about MRI, MS, and iron pathology.

1.2 MRI

MRI contrast is generated differently for various types of imaging methods but generally relies on altering one or several parameters of the MRI system. Since the focus of this work relates to brain iron and MS, MRI methods involving quantitative relaxation and phase susceptibility imaging will be discussed thoroughly. As well, other methods that relate to iron imaging or highlight other features of MS deserve

mention to represent the breath of techniques available and to justify the choice of methods used.

1.2.1 Physical Determinants of Contrast in MRI

Most MRI methods, especially those used for clinical purposes, rely on tissue relaxation differences to distinguish pathologies and tissue type. Relaxation consists of both longitudinal and transverse components where perturbed magnetization approaches equilibrium along the magnetic field and in a perpendicular orientation respectively [1]. Longitudinal relaxation is an energetic process where interactions occur between spins and the surrounding lattice whereas transverse relaxation is primarily due to spin-spin interactions which result in irreversible spin dephasing. Furthermore, reversible dephasing can occur in the transverse plane from spatially dependent static background magnetic fields which locally alter the strength of the main magnetic field and cause slight changes in precession. These relaxation processes all occur at exponential rates with the constants T_1, T_2 , and $T_2^\star$ each of which depends on various tissue characteristics.

A mathematical approach is required to understand how relaxation times vary with different magnetic field strengths, susceptibility sources, and tissue type. Individual spins move and interact with magnetic moments from other nuclear dipoles or local fields, resulting in rapid and random microscopic magnetic field variation. An autocorrelation, $G_c(\tau)$, of these magnetic field fluctuations over time results in a statistical function that describes how similar the magnetic field is from one time (τ) to another later time. The Fourier transform of the autocorrelation function results in a power spectral density function, $J(w)$, which describes the relative proportion of spins experiencing fluctuations in magnetic fields at different frequencies (w).

$$G_c(\tau) = e^{\frac{-\tau}{\tau_c}} \tag{1.1}$$

$$G_c(\tau) \Leftrightarrow J(w) \tag{1.2}$$

$$J(w) = \frac{\tau_c}{1 + w^2\tau_c^2} \tag{1.3}$$

T_1 and T_2 relaxation can be described in terms of the power spectral density function according to the following equations for homogeneous solutions [2]

$$T_2 = \frac{1}{R_2} = \frac{2K_p}{3J(0) + 5J(w_0) + 2J(2w_0)} \tag{1.4}$$

$$T_1 = \frac{K_p}{J(w_0) + 4J(2w_0)} \tag{1.5}$$

The constant K_p contains factors independent of temperature and frequency which are related to dipolar coupling. As well, these equations predict T_2 as being shorter than T_1 for proton Nuclear Magnetic Resonance (NMR).

Correlation time is an average measure of tissue fluidity. Increased correlation time occurs when individual spins remain in the same magnetic environment for a longer average time. For example in myelinated tissue, boundaries exist which restrict water motion leading to less diffusion and a higher correlation time. More specifically, the correlation time is the time needed for the root mean square deflection of the spins' magnetism to be 1 radian through motion including vibration, rotation, and diffusion.

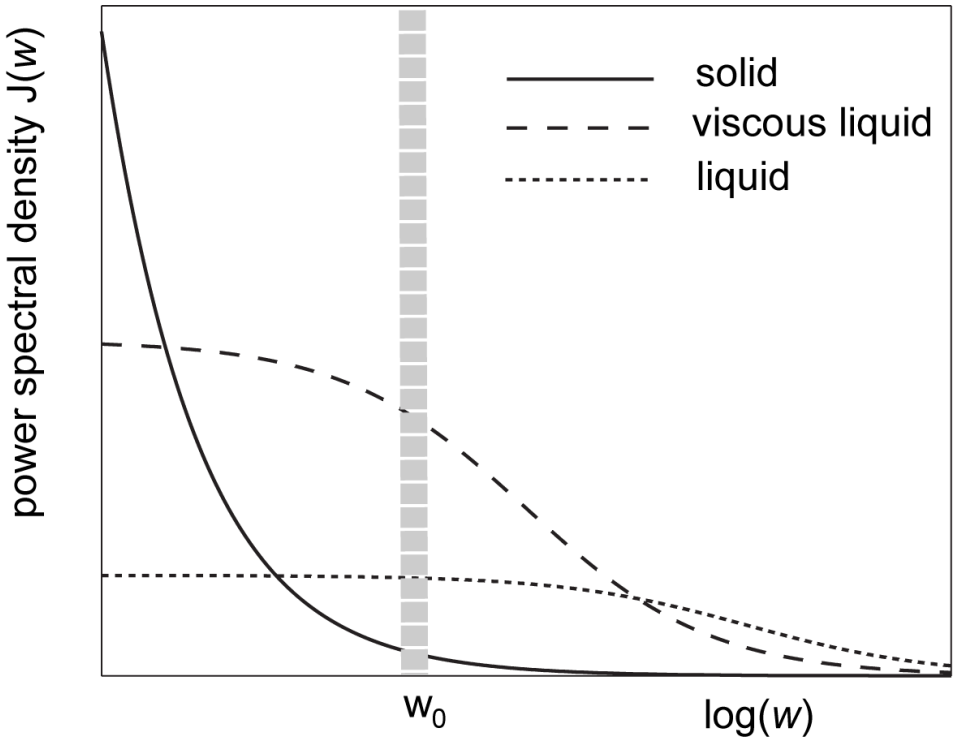

Figure 1.1: Power spectral density functions for a liquid, viscous liquid, and solid. Relaxation rates are dependent on the power spectral density at the Larmor frequency.

Biological tissues are mostly compartmentalized with regions of water separated by boundaries including cell membranes and connective tissue. If exchange occurs between the compartments, more complicated relaxation occurs than in homogeneous materials. If the compartments exchange protons faster than the relaxation rate, the two compartments have a single relaxation rate which is the average of the

two. However, if the rate is slower than relaxation, relaxation becomes multiexponential.

T_1 relaxation is further modulated by internuclear separation (r) which again is important in biological tissues as heterogeneity is expected [3].

$$\frac{1}{T_1} \propto \frac{\gamma^4 \hbar^2 \tau_c}{r^6} \tag{1.6}$$

Paramagnetic atoms have the effect of increasing the total power of the magnetic fields experienced by nuclei as they diffuse which results in a larger area under the power spectral density curve. As a result, both T_1 and T_2 times would be locally reduced.

T_2' is a type of transverse relaxation dependent on static background fields which microscopically add or subtract from the main magnetic field. This results in dephasing of the transverse magnetization which could be reversed provided the spins do not move and experience a new magnetic environment. These background fields can arise from any effect that causes local loss of spin coherence such as microscopic susceptibility differences endogenous to tissue, air tissue interfaces, and motion from flow. $T_2^\star$ relaxation is dependent on both the static background component, T_2', and the irreversible T_2 component of relaxation.

$$T_2^\star = \frac{1}{R_2^\star} \frac{1}{\frac{1}{T_2'} + \frac{1}{T_2}} \tag{1.7}$$

For a distribution of microscopic spheres the R_2' ($\frac{1}{T_2'}$) can be modelled by:

$$R_2' = \frac{2\pi}{9\sqrt{3} N \frac{v}{V} \gamma \Delta\chi Bo} \tag{1.8}$$

where the number of spheres (N) is small $N>>1$, the volume of each sphere (v) must be small compared to the voxel volume (V) $v<<V$, and the density of states satisfies a Lorentzien [4]. Although many biological tissues are often not homogeneous, this equation is useful in predicting changes in R_2' based on the change in volume, number, or susceptibility of cellular components such as ferric iron containing proteins.

A different type of contrast can be utilized in MRI by measuring the phase (or angle) of the complex spins within a region as opposed to the transverse spin magnitude. This relies on a different physical concept which is due to subtle changes in the regional precession frequency of spins due to susceptibility differences, chemical shift, motion, or proton exchange [5].

Susceptibility (χ) is a property of a material in which magnetization (M) is induced within the material when placed in a magnetic field (H). This induced

magnetization can add to or subtract from the magnetic field that the object is in.

$$M = \chi H \tag{1.9}$$

Table 1.1: Magnetic susceptibility of biological substances

Substance	susceptibility (ppm)
Water	-9.05
Lipids	-10
Ferritin[a]	520
Deoxyhemoglobin	-6.56

[a]Fully loaded with iron.

Susceptibility can be diamagnetic, paramagnetic, superparamagnetic, or ferromagnetic, each of which adds to or subtracts from the applied magnetic field through different mechanisms [1]. Water has a susceptibility of -9.05ppm and is used as a reference within the body. When added to tissue, which mostly consists of water, diamagnetic materials make the local susceptibility more negative while materials of other susceptibility types make it more positive. Diamagnetism is caused by slight shifts induced in circulating electrons within an atom or molecule when placed in a magnetic field as defined by Lenz's law. The change in angular speed induces a magnetic field opposite to the applied magnetic field. An increase in the magnetic field results in a linear change in the induced field in diamagnetic materials because the electron speed (or induced current) is increased. Since diamagnetism is not dependent on spin populations aligning with the field, there is no temperature effect.

The phenomenon of paramagnetism is caused by unpaired electrons within an atom. An unpaired electron has an associated dipole magnetic field which produces an atomic moment. These moments are randomly distributed at equilibrium but in the presence of a magnetic field, they align parallel and antiparallel to B_o according to the Boltzman distribution due to thermal motion, similar to nuclear magnetic moments. Because the atomic moment is much larger than the nuclear moment, the surrounding local field can deviate from the applied field. Therefore, paramagnetic materials induce a field shift which is proportional to the applied magnetic field. Since all atoms or molecules possess electron clouds, diamagnetism is a property associated with all atoms and when electrons pair within an orbital, the spin magnetic moments are canceled and paramagnetism no longer dominates. Ferromagnetic materials produce a magnetic field that is not dependent on B_o. This is due to spin-spin coupling where all nuclear spins within the system are permanently

aligned below a critical temperature. Superparamagnetism is somewhat similar to ferromagnetism in that all of the domains align but only during the application of an external magnetic field, regardless of the magnetic field strength, while still over a critical magnetic and temperature threshold.

Susceptibility differences can cause changes in the phase (θ) of the transverse magnetization by adding to or subtracting from the main magnetic field (B_0) according to:

$$\theta = -\gamma \int \Delta B(t) \mathrm{d}\tau \tag{1.10}$$

However this relationship is somewhat simplistic because the field distribution external to an object with different susceptibility will be perturbed from the object's induced magnetization which depends both on the susceptibility of the object and the shape of the object. This is due to Gauss's law of magnetism, which states that magnetic monopoles do not exist and magnetic flux through a Gaussian surface is zero. These field equations can be analytically solved for simple shape such as spheres and cylinders while more complicated structures can be solved with numerical models. For example the equations for the magnetic field measured from a sphere with radius (a) and at a distance from the sphere center (r) with external susceptibility (χ_e) are [1]:

$$fieldshift_{internal} = \frac{1}{3}\chi_e B_0 \tag{1.11}$$

$$fieldshift_{external} = \frac{\Delta\chi}{3}\frac{a^3}{r^3}(3cos^2\theta - 1)B_0 + \frac{1}{3}\chi_e B_0 \tag{1.12}$$

There are other contrast mechanisms, as opposed to relaxation or susceptibility, that could be important for evaluating tissue changes in multiple sclerosis including: diffusion, magnetization transfer, and chemical shift. Diffusion contrast relies on creating a signal difference due to moving spins into regions with a different resonance frequency by the application of spatially varying magnetic gradients [6]. Magnetization transfer imaging relies on the transfer of magnetization from macromolecular protons to hydration layer protons, which produce saturation of the magnetization, effectively reducing the signal [7]. Hydrogen spectroscopy can evaluate the area under individual chemical peaks which resonate at a slightly different frequency (<10ppm) from water [3] and this can show changes in different tissue components such as myelin, axons, or glial cells. The details of these methods can be found elsewhere but their mention is warranted for comparison to MRI relaxation and phase contrast methods.

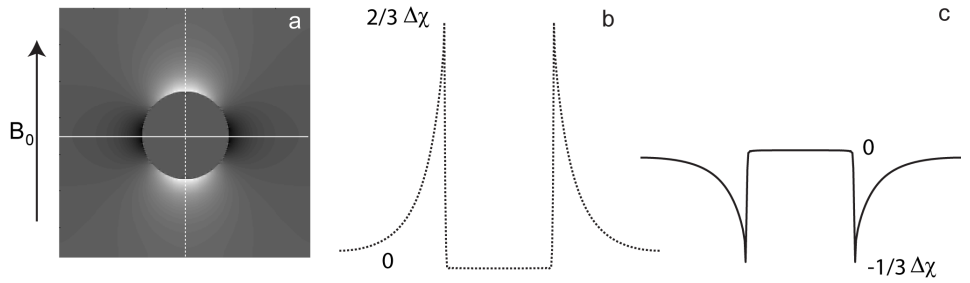

Figure 1.2: a) Simulated sagittal image of the magnetic field perturbation from a sphere with susceptibility difference $\Delta\chi$ from the background with the background susceptibility $\chi_e = 0$. b) profile of the magnetic field perturbation parallel to B_0. c) profile of the magnetic field perturbation perpendicular to B_0.

1.2.2 MRI Contrast in Neurological Disease

Although the pathology of MS will be discussed in a later section, the physical determinants of contrast in MRI can be exploited to study various components of the disease. Several tissue changes in MS that can be evaluated using MRI relaxation or phase contrast mechanisms include edema, cellular loss, and iron accumulation [8].

Iron in the body can take one of two atomic forms, ferrous or ferric, and iron atoms can be incorporated into different molecules. The atomic form of iron and how the atoms are incorporated into molecules will have different effects on relaxation. Ferric iron has an unpaired electron and is paramagnetic while ferrous iron has paired electrons and is slightly diamagnetic. As well, ferrous iron in the brain is thought to be primarily unbound with a much lower concentration compared to ferric iron. Ferric iron can be incorporated into several proteins including ferritin, hemosiderin, and low molecular weight proteins. Ferritin is the major storage molecule for iron in the body yet the structure, biology, and magnetic properties of iron-loaded ferritin are still not fully understood. Since most brain iron is stored in ferritin (in the absence of intracranial blood and breakdown products), the discussion of iron effects in MRI images will focus on ferritin.

In general, tissue iron causes an increase in R_2 relaxation by increasing the total area under the power spectral density curves [9]. However, ferritin has a somewhat unusual effect on R_2. There is a linear relationship between R_2 and ferritin iron concentration with possibly non-exponential relaxation when ferritin is in high abundance [10]. The outer sphere theory that relates R_2 relaxation to ferritin predicts a quadratic decrease in T_2 with field strength as protons diffuse

locally near the spatially varying magnetic field created by a ferritin sphere with volume fraction v/V, radius r, frequency shift w_r, and water diffusion coefficient d [11].

$$\frac{1}{T_2} = R_2 = \frac{4}{9} v/V \Delta w_r^2 \frac{r^2}{d} \tag{1.13}$$

However, experimental evidence from ferritin solutions show a linear dependence of R_2 on field strength [9]. The proton exchange model attempts to explain this observation [12]. It proposes that protons on the surface of ferritin exchange with bulk water, where a different magnetic field is experienced, thereby increasing R_2. As well, this model provides an explanation for pH changes that are observed with relaxation measurements of ferritin. However, these models are not sufficient to explain in vivo iron relaxation because they assume a homogeneous distribution of ferritin. A biexponential decay or other non exponential patters can be observed in tissues that have compartmentalized of ferritin or very high concentrations of ferritin [10]. Evidence of in vivo compartmentalization is demonstrated by a larger slope between R_2 and B_0 than predicted with the proton exchange model, which can be explained by iron clustering. The linear change of R_2 in relation to B_0 for iron containing tissues is supportive of relaxation due to ferritin and hemosiderin rather than low molecular weight iron containing complexes, which would demonstrate a quadratic relationship [13].

R_2 is not specific for iron, especially in MS, as inflammation, edema, cellular loss, and demyelination can result in decreased R_2, which can occur concurrently with iron accumulation. R_2 decreases because water is less constrained, increasing the correlation time in equation 1.4. R_2 relaxation differs in grey matter and white matter in part because of water and myelin concentration. There is a 12% difference in water content between white matter (72%), and grey matter (84%) [14] . Grey matter has less myelin compared to white matter with even further variability between specific brain regions as measured with myelin water fraction [15]. These range from 0.02-0.05 (MWF) in grey matter to 0.08-0.16 (MWF) in white matter.

Since T_1 relaxation occurs from fluctuating magnetic fields at a relatively short distance, the effect of ferritin on T_1 relaxation is minimal because the protein shell around iron atoms separates the local magnetic field from nearby water protons [16]. However other iron containing proteins such as deoxyhemoblobin or exogenous substances with unpaired electrons such as gadolinium can have substantial effects on T_1 relaxation.

Edema, cellular loss and demyelination result in an increase in T_1 because there is less matrix in which to exchange energy. The correlation time will be decreased because the protons will experience a dissimilar environment, resulting in a T_1 in-

crease (eqn 1.5).

$T_2^\star$ is more sensitive for iron than T_2. The T_2' component of $T_2^\star$ creates a larger spatial influence on relaxation which can capture the effects of punctate ferritin iron sources [14]. $T_2^\star$ of iron may show non-exponential decay in certain circumstances; if a small number of dipoles are present, in vascular networks, or with macroscopic background fields [17]. This is due to the relationship between voxel geometry and field inhomogeneity. In addition, non-exponential decay can occur in the presence of myelin [18] due to separate, non exchanging regions of water. $T_2^\star$ can be further influenced by tissue anisotropy and head angle to the main magnetic field [19] which is important for highly organized tissue.

Ferric iron, being paramagnetic, causes a negative phase shift in the local transverse magnetization vector. This effect is independent of water concentration, unlike relaxation methods. Iron concentration has a linear relationship with phase as demonstrated in (Eqn 1.10). However other sources of susceptibility in neurological disease can cause shifts in transverse magnetization phase [20]. Diamagnetic myelin loss results in an overall negative phase shift in transverse magnetization, similar to iron accumulation. Furthermore, accumulation of diamagnetic calcium can be a feature of neurological disease, particularly in tumours, and this causes a positive phase shift, which is in opposition to iron accumulation. As well, vascular changes such as decreased oxygenation or focal hemorrhages result in positive changes in susceptibility from increased deoxyhemoglobin and hemosiderin concentration which causes negative phase shifts.

Other contrast mechanisms could be affected in neurological disease that result from demyelination, inflammation, and degeneration. These biological processes result in increased diffusion, decreased MTR, changes in chemical peaks, and a lower MWF [8]. Similar to phase or relaxation MRI, these other contrast methods are not specific to one pathological disease process.

1.2.3 Imaging

Contrast mechanisms are essential to distinguish different tissues and identify pathology in MR images but the received signal must be processed in a way to spatially localize these changes for visualization and quantification. Spins are spatially localized by applying orthogonal linear gradients in a specified order then utilizing the Fourier relationship between frequency and location.

An image is obtained using the inverse Fourier transform where the complex transverse spin vector ($M(x, y)$) at a location is related to the time domain signal ($S(t)$) mathematically by

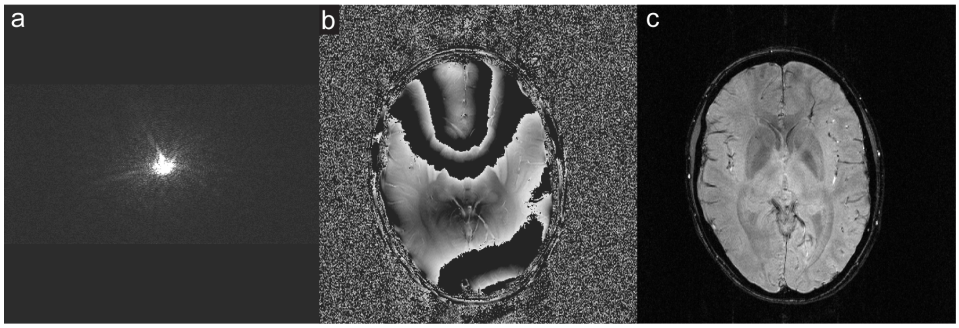

Figure 1.3: a) K-space data is directly acquired during the imaging process (magnitude shown). b) Phase image of Fourier transform of K-space data. c) Magnitude image of Fourier transformed K-space data. Data collected using a 2D gradient echo imaging sequence from a 3T imaging system.

$$S(t) = \int_x \int_y M_{xy}(x,y) \mathrm{e}^{-i(k_x \cdot x + k_y \cdot y)} \, \mathrm{d}x \, \mathrm{d}y \tag{1.14}$$

$$k = \gamma \int G \, \mathrm{d}t \tag{1.15}$$

K-space data (eqn 1.15) are obtained by applying gradients with amplitude (G), RF pulses, and acquiring data in a specific order with differing timing parameters; this combination is called a pulse sequence. Discrete sampling is required where the sampling intervals are related to the field of view (FOV) through:

$$\mathrm{FOV} = \frac{1}{\Delta K} \tag{1.16}$$

The combination of parameters for each sequence will impact contrast, signal to noise ratio (SNR) , imaging time, specific absorption rate (SAR) , and resolution. In terms of the pulse sequence components, these include the type of RF pulse used, the strength and duration of gradient application, timings between excitation and acquisition, and timings between each excitation. As well, the classification of pulse sequence will have a large effect on the final image.

This thesis focuses on specific applications of gradient echo (GRE) and spin echo (SE). For the purposes of detecting and quantifying iron pathology in MS, gradient echo imaging can be utilized to generate $T_2^\star$ images, $T_2^\star$ maps, and phase images while spin echo imaging can generate T_2 weighted images and T_2 maps.

Not only are pulse sequence parameters important in generating an image but post-processing is required to achieve the final result. Post processing can involve re-

construction of undersampled data, combination of data from multiple receiver coils, noise filtering, intensity normalization and specific algorithms related to quantitative imaging. Effectively combining data from different receive coils can involve different methods that utilize receiver sensitivity profiles, noise covariance, or both [21]; phase images require additional consideration such as a dual echo approach [22] as slight phase differences between receivers must first be corrected. This work utilizes two approaches for receiver combination: sum of squares and coil sensitivity estimation. A sum of squares method leads to excess noise in regions with poor sensitivity but is the simplest approach. Images can also be constructed by estimating coil sensitivities from low pass filtered image data. Undersampling collects a subset of k-space and utilizes the complex conjugate nature of the frequency domain for reconstruction. K-space from MRI does not have exact complex conjugate symmetry because of physical factors including eddy currents and motion. Therefore estimations are required to generate the missing data. Some methods in this work utilize Homodyne reconstruction in the phase encode direction to improve imaging time.

$T_2^\star$ weighted images are generally acquired with gradient echo imaging [17]. A single RF pulse tips the longitudinal magnetization into the transverse plane. Gradients are used to spatially dephase spins in the phase encoding direction. The readout gradient is applied during signal acquisition where spins experience different magnetic fields and precess at different frequencies. This process acquires one line of k-space. Other lines of k-space in the phase encoding direction are acquired with the application of a different strength of phase encode gradient (eqn 1.20. In this scheme, an echo is generated in the center of the readout with the prior application of a refocusing lobe of equal area. Further lobes can potentially be applied to both the slice select gradient and the dephasing readout lobe for flow compensation. For $T_2^\star$ contrast, the repetition time (TR) must be sufficiently long for most of the longitudinal magnetization to recover in order to avoid T_1 weighting (eqn 1.18). Alternatively, the flip angle (α) can be reduced to shorten the TR and still achieve adequate recovery of longitudinal magnetization, thus reducing overall scan time with a reduction in the magnitude of the transverse signal. As well, a long TE for adequate dephasing of signal is required for generation of $T_2^\star$ contrast (25-50ms at 1.5T and 7-20ms at 4.7T). With a reduced flip angle, optimal signal is achieved by relating the TR to the Ernst angle, for a spoiled gradient echo, which ranges from $15-35^\circ$ at 1.5T and $8-15^\circ$ at 4.7T.

$$\alpha = cos^{-1}(\frac{\mathrm{TR}}{T_1}) \tag{1.17}$$

To eliminate the refocusing of persistent transverse magnetization, spoiler gra-

dients are used in the slice select and readout directions which cause a 2π or greater dephasing across each voxel. RF spoiling is also commonly implemented by changing the phase of the RF transmission (B_1) and receiver pulse by typically 117° with each excitation. Phase encode rewinding ensures that magnetization phase is only encoded from individual excitations and is not the product of several excitations. Gradient echo sequences have the advantage of low tissue power deposition because of reduced flip angles and few RF pulses.

$$M = M_0 \frac{1 - e^{-\frac{\mathrm{TR}}{T_1}}}{1 - cos(\alpha)e^{-\frac{\mathrm{TR}}{T_1}}} sin(\alpha) e^{-\frac{\mathrm{TE}}{T_2^*}} \tag{1.18}$$

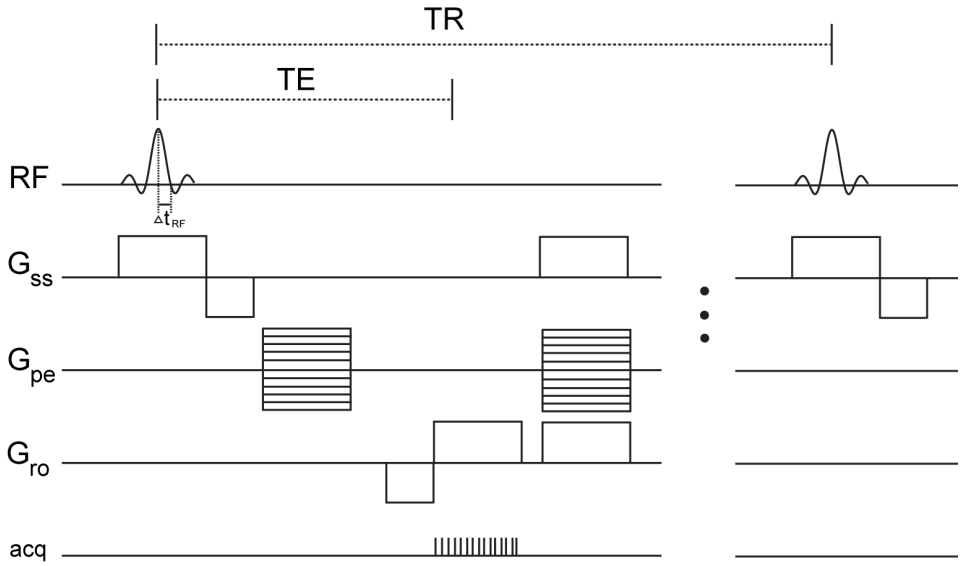

Figure 1.4: Pulse sequence diagram for gradient echo sequence. The RF pulse bandwidth is generally predetermined and the amplitude is calculated in conjunction with the slice select gradient amplitude. The phase encoding gradient, G_{pe}, is incremented with each TR for full FOV coverage. The spoiling gradients must be large enough to dephase spins at least 2π across each voxel. Phase gradients are rewound after each acquisition to prevent unwanted phase accrual over multiple readouts. Multiple slices can be acquired during each TR provided there is time to apply the same gradient order in a different slice.

Generally, the field of view, readout bandwidth, and timing parameters are chosen and appropriate gradient strengths and timings are calculated given certain relationships. Different parameters will be chosen for different purposes and tradeoffs must be considered. If fast imaging is to be performed, gradients will generally have large amplitude to reduce imaging time at the cost of having a high readout bandwidth (BW_{sample}). However for increased SNR, a lower gradient amplitude with a lower readout bandwidth will be chosen at the cost of imaging time and a modified point spread function.

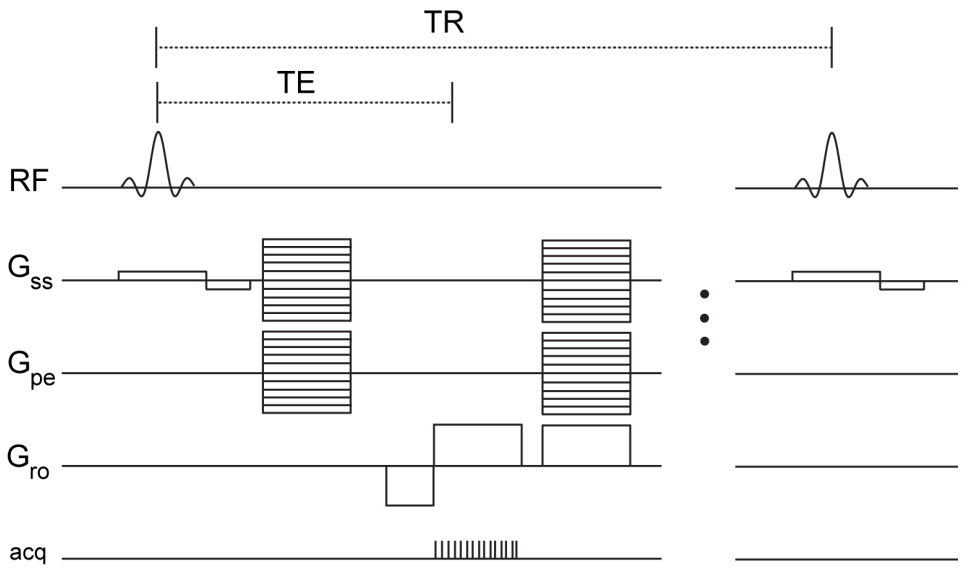

Figure 1.5: Pulse sequence diagram for a 3D gradient echo sequence. Generally, the flip angle is reduced compared to 2D gradient echo so the TR can be reduced for faster imaging. There must be adequate phase encoding steps in the slice select direction for proper Fourier transformation. The gradient amplitude during slice select is lower compared to 2D acquisition because a larger volume is typically excited.

$$\frac{1}{\Delta t} = \mathrm{BW}_{\mathrm{sample}} \geq \gamma \cdot \mathrm{G}_{\mathrm{ro}} \cdot \mathrm{FOV}_{\mathrm{ro}} \tag{1.19}$$

$$\Delta \mathrm{G}_{\mathrm{pe}} \leq \frac{1}{\gamma \cdot \mathrm{FOV}_{\mathrm{pe}} \cdot \tau} \tag{1.20}$$

$$\mathrm{BW}_{\mathrm{RF}} = \gamma \cdot \mathrm{G}_{\mathrm{ss}} \cdot \Delta \mathrm{z} \tag{1.21}$$

With MRI, distortion is introduced into the final image through the convolution of a point spread function. This is represented as a multiplication of a modulation transfer function by the ideal k-space representation of the object data. Ideally, the modulation transfer function would be non existent, which represents a delta function in image space, resulting in no distortion. Deviations from the ideal modulation transfer function can result from signal decay over the readout gradient or modulation in signal amplitude due to signal decay from multiple phase encode lines in k-space during the same excitation (applicable to FSE, and EPI). Gradient echo imaging generally does not have substantial modulations to the point spread function. This is because the readout bandwidth is generally high enough to mitigate significant modulation over one readout provided $T_s < T_2^\star$ [1]. As well, multiple phase encode lines are not acquired from one excitation.

$T_2^\star$ mapping collects a series of gradient echo images and mathematically estimates the $T_2^\star$ value in each voxel. This can be accomplished by acquiring k-space data using a multi-echo readout from the same excitation and phase encoding one line in k-space. Alternatively, separate acquisitions of entire images can be performed with different echo times (TE). One issue of $T_2^\star$ mapping is unwanted dephasing effects from air tissue interfaces or vessels. Techniques have been proposed to minimize effects from air tissue interfaces by gradient compensation[23], tailored RF pulses [24], or post-processing[25]. Gradient compensation is achieved by varying the amplitude of the refocusing slice select lobe over several acquisitions and combining the multiple resultant images. Similarly, tailored RF pulses improve coherence at the echo time by manipulating magnetization phase in the slice select direction. However these methods may require long acquisition times, poor resolution, and/or limited slice coverage. Alternatively, post processing techniques can be implemented which have no additional cost to time, resolution, or SNR. These methods model the magnetization behaviour to correct for susceptibility induced signal losses. Most methods assume signal loss due to dephasing effects from a linear gradient through a rectangular voxel[25]. The predicted result is a sinc modulation in signal intensity which can be spatially calculated with the acquisition of a background field gradient map (BFG). This map can be obtained by calculating the phase differences between two phase images with echo times differing by several msec [26].

$$\mathrm{S} = \mathrm{sinc}\left(\frac{\gamma\, BFG\, \Delta x, y, z\, TE}{2}\right) \tag{1.22}$$

However, this correction method is imperfect and could artificially modulate signal contribution from other susceptibility sources within the brain such as high iron containing deep grey matter structures, if a slowly varying spatial profile is produced. A simple means for mitigating dephasing effects from air tissue interfaces is reduction of voxel volume, provided there is adequate SNR and imaging time can be prolonged. The dimension along the strongest macroscropic background gradient has the largest contribution and is generally the slice thickness for axial imaging. Reduction in voxel volume will not decrease dephasing effects caused by microscopic dephasing sources such as ferritin or hemosiderin assuming a relatively homogeneous distribution throughout voxels.

Estimating the $R_2^\star$ signal decay can be accomplished with several approaches. The simplest method involves a single exponential least squares regression of individual voxels from all the images over the range of TEs acquired. However with later echo times, noise can strongly influence the signal and fitting can become unreliable. To overcome this, the later echoes could have less weighting in the regression

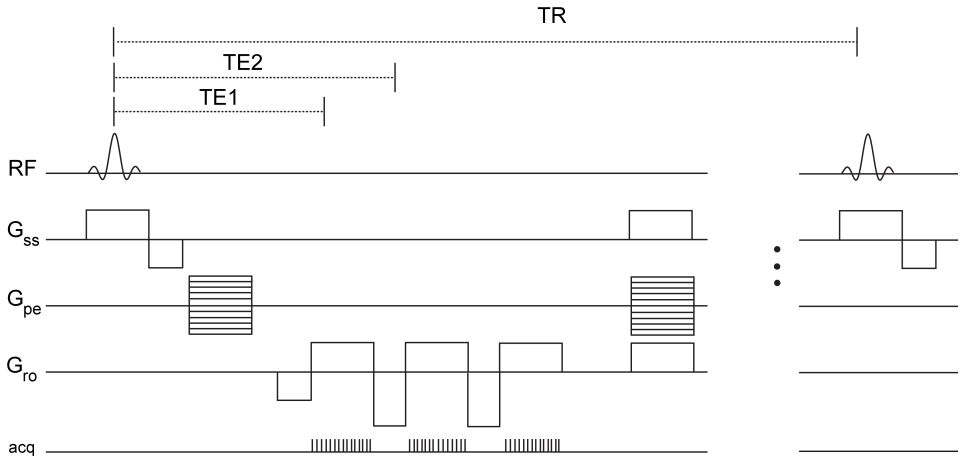

Figure 1.6: Pulse sequence diagram for a multi echo gradient echo sequence. Multiple echoes can be collected from the same excitation provided there is adequate signal in addition to readout gradient compensation to ensure echos occur in the centre of each readout. Lack of compensation will result in a cumulative linear shift in k-space at each echo resulting in a progressive phase ramp in image space with increasing echo time.

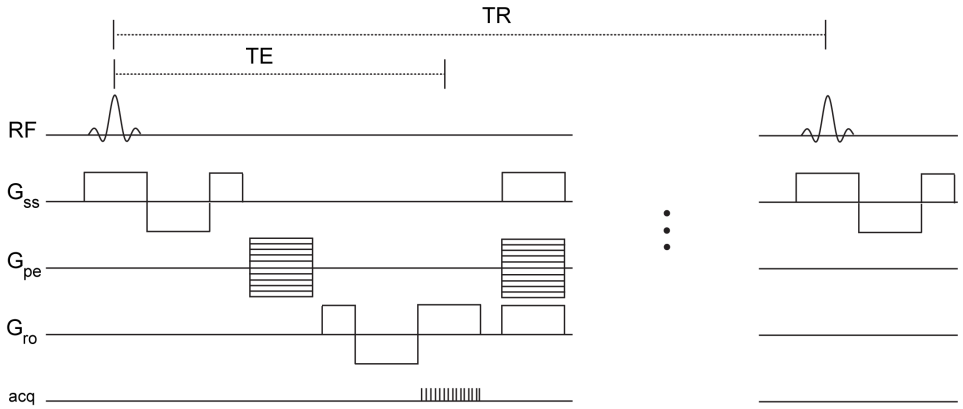

Figure 1.7: Pulse sequence diagram for a 2D gradient echo sequence with flow compensation. Phase can accumulate as spins move across linear gradients leading to improper spatial encoding. Extra lobes on the slice select and readout gradients remove phase accumulation for moving spins with constant velocity.

or could be excluded in the fitting process.

Phase imaging generally acquires one image at one echo time however combination of phase images from several echo times can result in improved SNR and signal contrast. The complex phase within a gradient echo image is given in equation 1.10. Therefore, images from different field strength can be appropriately compared by accounting for linear scaling factors. This is unlike quantitative relaxation methods where T_1, T_2 and $T_2^\star$ have a more complicated relationship with field strength. Although contrast scales proportionately with field strength, contrast to noise (CNR)

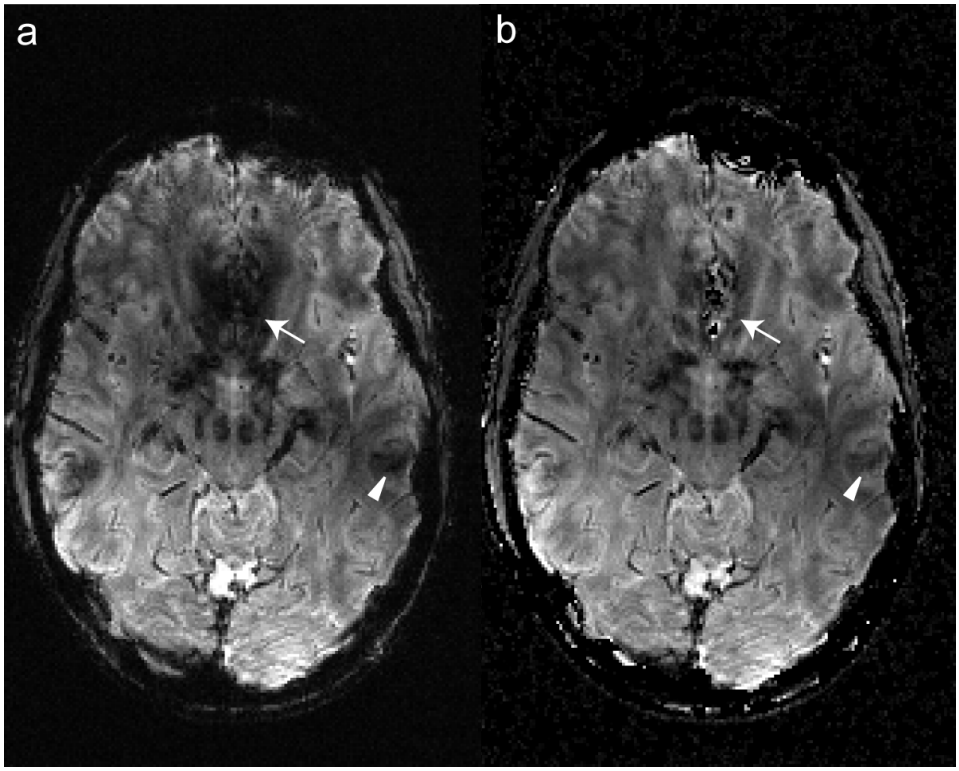

Figure 1.8: a) Uncorrected $T_2^\star$ weighted gradient echo image and b) corrected $T_2^\star$ weighted gradient echo image using background compensation assuming linear gradient through each voxel. Dephasing effects from paranasal air tissue interface (arrow) and dephasing effects from external auditory canal (arrow head).

is superior with increased magnetic field[17]. Equation 1.23 demonstrates this relationship with the standard deviation of the magnitude noise (σ_{mag}), TE, $T_2^\star$, ΔB, γ. Parameter K includes T_1, spin density, flip angle, and B_0.

$$CNR_{phase} = \gamma \cdot \Delta B \cdot \mathrm{TE} \cdot \mathrm{SNR}_{mag} = \frac{\gamma \cdot \Delta B \cdot \mathrm{TE} \cdot K \cdot e^{-\frac{\mathrm{TE}}{T_2^\star}}}{\sigma_{mag}} \tag{1.23}$$

Phase imaging requires background field removal through post processing techniques. The background field arises from the large susceptibility difference that occurs at air tissue interfaces and the geometry of the regional anatomy. The most simplistic method of removing the background field utilizes a high pass filter by dividing the inverse Fourier Transform FT^{-1} of the original complex raw data (D_K) by the inverse Fourier Transform of this same complex data multiplied by a window function (Wd_k) in k-space (eqn 1.24).

$$\theta = \mathrm{angle}\left(\frac{\mathrm{FT}^{-1}[D_k]}{\mathrm{FT}^{-1}[D_k \,\mathrm{x}\, Wd_k]}\right) \tag{1.24}$$

However this can lead to phase suppression in larger brain structures and may not adequately remove phase wraps in areas close to air tissue interfaces. Both of these issues can be troublesome when obtaining quantitative phase measurements. Other heuristic phase removal methods have utilized moving window functions or high order polynomial fitting. Newer methods including sophisticated harmonic artifact reduction for phase data (SHARP)[27] and projection onto dipole fields (PDF)[28] attempt to model the background field through the use of Gauss's Law by utilizing the property of zero magnetic flux through a closed surface.

Phase contrast relies on different mechanisms compared to relaxation. The phase within an object is dependent on the shape of the object while relaxation contrast does not. As well, phase imaging shows field perturbations external to an object. Both of these features in phase imaging can create difficulties with quantitative measures, making the measurements dependent on features other than tissue susceptibility. Furthermore, the choice of background field removal can have different effects on phase contrast. Reference phase measurements are commonly used to compensate for external phase effects and filtering issues however the choice of reference location could also influence quantitative measurements.

Susceptibility weighted imaging (SWI) is an interesting imaging method because it combines magnitude and processed phase information from one or more gradient echo acquisition [29]. It is seeing increased use clinically, particularly in diseases with iron deposition. Current uses include evaluation of stroke, cerebral amyloid angiopathy, trauma, venous anomalies, tumours, and multiple sclerosis [20]. Generally, a phase mask is created by applying a high pass filter to a raw phase image and retaining only negative phase values. The mask is subsequently multiplied several times, generally four, into the magnitude image.

Spin echo sequences are the primary clinical method employed for routine neuroimaging. These include T_2 weighted fast spin echo, T_1 imaging, T_1 contrast enhanced imaging, and fluid attenuated inversion recovery (FLAIR) imaging. Generally these sequences utilize one or more 180° refocusing RF pulse preceded by a 90° excitation pulse and gradients for slice, phase, and readout encoding similar to gradient echo imaging.

Fast spin echo imaging uses multiple refocusing pulses after each excitation pulse where multiple lines of k-space are acquired with each excitation. The effective echo is obtained when the center of k-space is sampled in the phase encoding direction. As well, the order of phase encoding should be appropriately chosen as a point spread function due to T_2 relaxation over the readout train.

T_2 mapping is similar to $T_2^\star$ mapping in that the signal decay is fit in individual voxels over multiple echo times. The major advantage of T_2 mapping is that spin refocusing negates effects from static field inhomogeneity. However notable limitations

include less specificity for iron, a need for precise refocusing pulses, and excessive SAR which is proportional to the square of the magnetic field strength. Because there are multiple RF pulses between signal acquisition, echo refocusing can lead to unwanted spin and stimulated echos. Several compensation mechanisms have been proposed including increasing the width of the refocusing slice, discarding the first echo, varying crusher gradients to isolate specific spin echo pathways, or mathematical modelling stimulated echo behaviour. This is of particular importance at high field where RF homogeneity is lacking.

Although not used in this thesis, other pulse sequences can exploit different contrast mechanisms which could be useful for studying multiple sclerosis. Diffusion imaging uses additional gradient pulses around 180° refocusing RF pulses which cause signal loss that is proportionate to the motion of spins. Magnetization transfer imaging indirectly examines macromolecular tissue content by relating signal to the quantity of bound protons in tissue. Off resonant pulses are applied which saturate bound protons. These protons exchange with free protons resulting in a reduced magnetization of free water. There are several methods of hydrogen spectroscopy including single voxel techniques such as Stimulated Echo Acquisition Mode for imaging (STEAM) and Point Resolved Spectroscopy (PRESS) or spectroscopic imaging which can investigate the relative concentration of different molecules in the brain. These methods acquire signal in the absence of gradients which allows the determination of chemical peaks through an extra dimension of the Fourier transform. Chemical peaks occur because individual protons within molecules have a slightly different resonant frequency due to electron shielding. Myelin water fraction (MWF) imaging is a T_2 relaxation method that utilizes a multiexponential model requiring many echoes [30]. Different exponentials are sorted into bins where the fastest component of T_2 relaxation is attributed to myelin 20-50ms.

Additional methods have been proposed for evaluating iron including Magnetic Field Correlation Imaging (MFC) , Direct Saturation Imaging, and Field Dependent Relaxation Imaging (FDRI) , however their use is limited. FDRI measures the difference in R_2 between different field strengths and has a very high sensitivity to iron [31]. MFC imaging uses a series of asymmetric spin echoes which should be independent from the dipolar mechanism seen in phase imaging [32]. Direct Saturation Imaging uses off resonance saturation pulses similar to magnetization transfer rate (MTR) imaging however the signal intensity is reduced because of the local iron environment which alters T_2 [33].

1.2.4 High Field

High field MRI systems are generally defined as MRI systems with the main magnetic field being greater than 3.0 T. High field has distinct differences compared to

lower field systems and by carefully weighing a variety of factors, specific applications can greatly benefit from the use of high field. In keeping other parameters equal, imaging characteristics can be compared between field strengths. With increasing magnetic field strength; SNR increases, SAR increases, T_1 increases, spectral dispersion increases, susceptibility dispersion increases, and RF homogeneity decreases. Aside from the characteristics of images, several technical considerations are associated with high field MRI including more sophisticated hardware design (RF coils, gradient coils, and main magnetic field coils), increased cost, and greater fringe fields.

SNR linearly increases with field strength based on the Boltzmann distribution of proton alignment parallel and antiparallel to the main magnetic field, larger EMF generated in the RF receiver, and increased noise [34]. This can allow for a decrease in image acquisition time because either less signal recovery or a lower flip angle is required for equivalent SNR compared to lower field. For applications that require image averaging, proportionately fewer acquisitions are necessary for equivalent SNR with increased field strength. Alternatively, higher resolution images could be obtained with equivalent SNR compared to images from lower field. However SNR benefits are spatially dependent with increased magnetic field strength because of increased RF inhomogeneity effects.

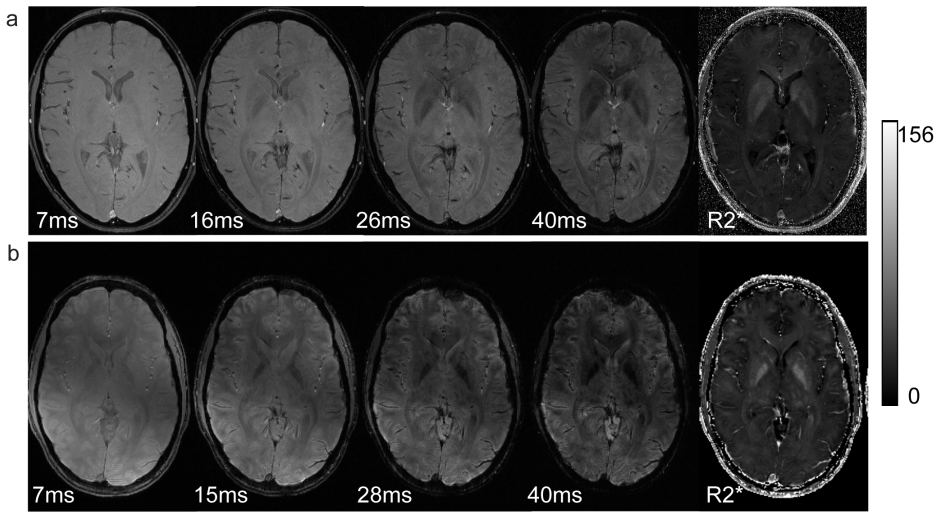

Figure 1.9: Gradient echo images and $R_2^\star$ map from a) 3.0T (2D sequence TR= 500ms FA=70° resolution = 512x256) and b) 4.7T (3D sequence TR=44ms FA=10°). $R_2^\star$ increases in iron rich brain regions with field strength.

RF inhomogeneity arises from electromagnetic constructive and destructive interference at different spatial locations within the head due to different path lengths between coil elements [35]. Inhomogeneity is increased at high magnetic field due

to a smaller RF wavelength that approaches the dimensions of the head. The wavelength is on the order of meters in a vacuum but due to the dielectric effect in the brain, the wavelength is further reduced. This can lead to a 40% reduction in excitation at the the edge of the head compared to the center. For several methods, such as $R_2^\star$ mapping or phase imaging, this has little effect except for an uneven distribution of signal to noise. However for non-quantitative methods such as FSE or GRE magnitude imaging, this effect can result in hyperintense and hypointense regions within an image which are not dependant on tissue characteristics. A double angle method can be used to determine the spatial variation of flip angles for potential correction.

In phase imaging, contrast to phase noise increases with field strength (eqn 1.23). Furthermore, optimal tissue contrast between two tissue types is achieved when the echo time is equivalent to the average $T_2^\star$ of these two tissues. Therefore the echo time will be shorter at higher field which will reduce overall imaging time. However, air and tissue have substantially different susceptibilities, thus the deleterious field effects that result are more pronounced at high magnetic field.

SAR is the amount of RF power deposition per weight of tissue. It depends on the square of the magnetic field keeping all other parameters equal (eqn 1.25).

$$\text{SAR} = \frac{\text{Joules of RF energy per second}}{\text{kg of body weight}} \tag{1.25}$$

$$\text{Power} \propto \frac{B_0^2 \alpha}{T_{rf} \cdot \text{TR}} \tag{1.26}$$

There are safety limits to overall RF power body deposition as well as different limits to specific body parts. SAR must be limited to less than 4 W/kg for the entire body and less than 3.2 W/kg averaged over the head. RF profiles may not be uniform within the head, especially with high magnetic field, where focusing effects can result in regional anatomy receiving higher energy deposition. The negative consequences of this have not fully been explored especially at ultrahigh field systems. To limit SAR at high field a number of pulse sequence parameters can be altered (eqn 1.26) including lengthening TR intervals, using different RF pulse shapes, maintaining lower flip angles, and using lower bandwidth RF pulses [1].

T_1 increases at high field thus TR should be longer for comparable contrast in T_2 imaging for more complete longitudinal recovery. Furthermore, less T_1 contrast is evident in T_1 weighted images at higher magnetic field for most brain tissue. Specific applications can benefit from this feature of high field including background tissue contrast suppression with gadolinium agents which have a much faster T_1 compared to brain tissue.

At high field, spectral dispersion is problematic for routine proton imaging be-

cause of increased water fat separation.

$$w = \gamma B(f_1 - f_2) \tag{1.27}$$

To maintain water and fat signal within one slice, higher bandwidth RF pulses are needed resulting in an increased SAR. There are applications that benefit from spectral dispersion including spectroscopy methods. Spectral resolution is increased with higher magnetic field as spectral dispersion increases allowing the separation of chemical peaks which would otherwise be indistinguishable.

$$B_{seen} = (1 + \chi)B_0 \tag{1.28}$$

Multiple RF coil arrangements for signal reception can have added benefits compared to a single receiver, particularly at high field [35]. Parallel acquisition techniques can decrease SAR by reducing the number of excitation pulses although with a reduction in SNR. Alternatively, multiple receiver coils can be used to improve SNR by utilizing certain coil combination methods. This is particularly useful for locations in the center of the brain which are spatially distant from the reception coils, making adequate signal to noise in these regions difficult to achieve at low field strength. Multiple coil arrangements are useful for imaging techniques that require a strong SNR such as $R_2^\star$ mapping or phase imaging of deep brain structures. Both of these sequences use comparatively long echo times and local iron can decrease the transverse signal amplitude. This can create problems in estimating $R_2^\star$ from longer echos or in measuring phase as average transverse magnetization angle can become uncertain with small amplitude.

Magnetization transfer effects are more pronounced at high field and can decrease signal when many slices are acquired with large flip angles[34]. This can be problematic for incidental magnetization effects where large flip angles are used in multi-slice imaging.

MRI is an expensive imaging modality partially because of specific and complicated hardware requirements which are more costly at high magnetic field. With increasing field strength, gradient coils are susceptible to more torque and require different design considerations. As well, the main magnetic field requires more rigid control over temperature to maintain superconductance as superconductivity is a function of current, temperature, and material. Physical parameters of a birdcage coil including the resonator length, inductance, and capacitance are matched to the higher frequency needed at high field while still retaining adequate homogeneity and frequency output.

High field MRI can greatly benefit quantitative MRI methods such as $R_2^\star$ mapping or phase imaging with improved image resolution, higher SNR, and higher iron

sensitivity. In these applications, the advantages of high field appear to outweigh the deleterious aspects.

1.3 Multiple Sclerosis

Multiple sclerosis is a disease of the central nervous system (CNS) with features of focal demyelination, inflammation, and neuronal degeneration. The cause of this disease remains unknown and treatment options offer minimal benefit for slowing disease progression in the relapsing remitting phase and no confirmed benefit in the secondary progressive phase. It is currently believed that MS begins as an inflammatory autoimmune disorder mediated by autoreactive T lymphocytes.

1.3.1 Epidemiology

MS affects young adults with higher rates in females compared to males by a ratio of 2.3:1 [36]. MS prevalence has a geographic variance which could depend on several factors. Higher frequency areas include Europe, Canada, northern United States, New Zealand and southeast Australia with prevalence of more than 100 per 100000. This difference is explained in part by racial differences with a higher proportion of white populations in these regions. It has been postulated that vitamin D from sunlight exposure could be protective however there is new evidence to show that latitude does not influence MS incidence in Europe or North America [36]. An infectious stimulus of the immune system could play a role in the development of the disease [37] and it has been shown that the risk of MS increases after Epstein Barr Virus infection and Varicella Zoster Virus exposure. There are a host of genetic factors that are linked to the development of MS but a single gene is not causative in the disease. The risk of MS increases with certain alleles of HLA-DRB1 locus on MHC II which encodes for an important protein involved in T-cell activation and cell signalling. The risk of developing MS in dizygotic twins is the same as for siblings (3-5%) which indicates that intrauterine factors are unlikely to contribute while the risk for monozygotic twins is 20-39%.

There are four subtypes of MS which are: relapsing remitting, primary progressive, secondary progressive, and progressive relapsing [38]. Of initially diagnosed cases, RRMS constitutes 85-90%, PPMS makes up about 10%, and PRMS makes up less than 5%. On average, RRMS will convert to SPMS after 10 years. Primary progressive MS has a more rapid disease progression on average and a more steady progression of disability compared to a relapsing remitting course.

There are several clinical measures of disease severity with the most common being the Kurtzke expanded disability status scale (EDSS) [38] or frequency of relapse. Others measures include the MS functional composite (MSFC), MS severity

score (MSSS), and cognitive batteries. The EDSS evaluates disability due to MS on a scale from 0-10 where 0 is normal and 10 is death due to MS. Scores ranging from 0-4 represent dysfunction in various functional systems including the pyramids, cerebellum, brainstem, sensory system, bowel and bladder, visual system, and cerebrum. Scores above 4 represent mainly ambulatory dysfunction. Problems exist with using this scale to evaluate disability because it is nonlinear, EDSS above 4 is often reported by history and not objectively evaluated, and inter and intra rate variations are common. MSFC evaluates ambulation, cognitive function and upper limb function using standardized methods that are easy to administer and have a high inter and intra observer reliability [39]. It has advantages of being highly reliable and generates scores on a continuous scale. The MSSS utilizes EDSS but modifies the scores based on the length of disease, which has been shown to more accurately represent disease progression and severity [40]. Two commonly used cognitive batteries are the Minimal Assessment of Cognitive Function in MS and the Brief Repeatable Neuropsychological Battery. Each of these batteries contain tests that assess processing speed, learning, memory, executive function, and language.

1.3.2 Diagnosis and Monitoring

Multiple sclerosis is primarily a clinical diagnosis with no individual clinical, laboratory, or imaging findings that are unique to the disease. Diagnosis criteria have changed over time but consistently rely on objectively proving dissemination in space and time of demyelinating CNS lesions with no other known cause. The Poser criteria were introduced in the early 1980s and used clinical characteristics and laboratory studies including CSF analysis, evoked potentials and neuroimaging. However MRI has improved considerably over 20 years while the Poser criteria have not been updated. In 2001, the McDonald criteria were introduced and utilized clinical MRI findings to supplement or replace criteria for showing dissemination in space or time. The most recent revisions to the McDonald criteria [41] aim to simplify the diagnostic approach while retaining a high sensitivity and specificity. Dissemination in space is demonstrated on MRI by one or more T_2 lesions in at least two of four regions (periventricular, juxtacortical, infratentorial, or spinal cord) or by a second clinical attack implicating a different site in the CNS. Dissemination in time is demonstrated on MRI by the presence of asymptomatic gadolinium enhancing and non-enhancing lesions, or a new T_2 or gadolinium enhancing lesion, or by the development of a second clinical attack. Criteria to diagnose progressive MS requires one year of progression, plus two of three: dissemination in space, dissemination in space in the spinal cord, elevated oligoclonal bands or IgG index in CSF.

Common presenting symptoms in MS include sensory symptoms in limbs or

face, visual loss, diplopia, motor weakness, gait disturbance, impaired coordination, bladder and bowel dysfunction, and pain. Several pathoneumonic symptoms exist including Lhemitte's sign and internuclear ophthalmoplegia (INO) which can aid in diagnosis. Relapses are generally defined as acute onset of clinical dysfunction that peaks within days and is not less than one day. This is followed by remission during which symptoms and sign resolve to a variable extent. Because initial and ongoing symptoms can be highly variable, MRI is essential in ruling out other pathology and confirming the diagnosis but falls short of appropriate longitudinal monitoring which could potentially be used for treatment and management decisions with better MRI methods.

There are no guidelines for following MS with MRI after a diagnosis is confirmed however routine imaging is generally performed yearly, or at the time of a relapse [42]. Standard protocols examine size and number of T_2 enhancing lesions as well as number, size, and morphology of T_1 enhancing lesions. Protocols will generally include the following imaging methods: sagittal and axial FLAIR, sagittal and axial T_2 weighted, axial T_1 weighted with and without contrast, proton density, and spinal T_2 weighted if there is clinical concern of spinal cord abnormalities. Conventional MRI correlates poorly to clinical status for several reasons [8]: strategic lesions can cause significant disability yet lesion load may appear small on MRI, MRI can depict inflammation but the immune system has both destructive and reparative functions in MS, neurodegeneration is not well visualized and is difficult to evaluate, and adaption with reorganization of the CNS cannot be observed. Treatment decisions are generally based upon clinical progression however it has been suggested that monitoring lesions load with imaging could be beneficial [42]. As a general rule, no new lesions results in maintenance of current treatment, few new lesions may results in a change in treatment, and many new lesions should prompt a change in treatment. However these recommendations are subjective and it is often difficult to evaluate new lesions if baseline lesion load is high. Because MRI is costly and time consuming, new methods of evaluating disease progression and response to treatment are needed that are both sensitive and specific to CNS dysfunction.

There are no imaging findings that are unique to MS but some findings are highly characteristic of the disease. Every lesion is believed to have T_1 contrast enhancement at some point. Therefore, if no enhancing lesions are observed over time, this should prompt the consideration of another diagnosis. As well, lesions are common in the corpus callosum and spinal cord therefore absences of lesions in these locations should prompt further investigation. MS lesions can have certain morphology which often show Dawson fingers where inflammation extends along vasculature and generally the size of lesions range from <1mm to several centimetres. WM abnormalities are the most apparent finding with clinical MRI therefore

many prior studies have focused on the evaluation of WM lesions in comparison to disability. However these studies showed poor correlation to disease. New MRI methods are required to appropriately follow the disease over time by examining other CNS locations and aspects of the disease other than WM inflammation and demyelination.

1.3.3 Pathology

Tissue pathology that occur in MS can be described by either the cells are affected or what processes occur at different disease stages. As with clinical features, the pathology in MS is quite heterogeneous which possibly reflects different mechanisms of tissue damage. Although many aspects of the disease seem to be mediated by the immune system, the cause of MS remains unknown. The general pathological features associated with MS are demyelination, inflammation and neuronal degeneration.

Cells

T cells seem to be a main mediator of pathology and many therapeutic agents aim to modify their function [43]. Both CD4 T cells, and CD8 T cells propagate the inflammatory immune response and potentiate cellular damage. Dysfunctional CD4 T cells in MS include Th1 and more recently discovered Th17 cells which both stimulate the inflammatory response and produce proinflamatory cytokines, and potentially Th2 cells which promote humoral immunity and have anti-inflamatory effects. Compared to Th1 cells, Th17 cells cross the blood brain barrier (BBB) more efficiently, cause more damage to the BBB, and cause more damage to neurons. CD8 cells cause direct cellular damage by releasing perforin and granzyme, lymphotoxin, and activating the FAS receptor. Release of cytokines from CD8 T cells can result in damage to glial cells, axons, and promotion of BBB dysfunction. Unlike CD8 cells which have a nonspecific immune response, CD4 cells have antigen specific targeting and in MS are thought to target MBP, PLP and MOG. CD4 cells could be stimulated to target self antigens because of molecular mimicry from other foreign antigens or through dysfunctional negative selection in the thymus. Antigen presenting cells (APCs) are needed to activate CD4 cells in both the periphery and subsequently in the CNS. Dendridic cells are major APC in the CNS but microglia, astrocytes and B cells can also present antigens. Antigen presentation can activate Th1 cells and Th17 cells into a pro-inflamatory state where pro-inflamatory cytokines are produced including INF-gamma and IL-17 IL-21 and IL-22 . Conversely, antigen presentation can also trigger an anti-inflammatory response by causing Th2 cells to produce IL-4 and IL-13. Interferon treatment in MS aims to convert the pro-inflamatory response

dominated by Th1 and Th17 cells to an anti inflammatory response dominated by Th2 cells. As well, glatiramer acetate therapy aims to block the presentation of antigens to T cells through competitive binding.

The BBB is a special endothelial lining of the CNS vasculature and is an important barrier to both pathogens in healthy individuals and auto reactive inflammatory cells in MS. It differs from other vascular endothelial linings because of tight junctions between cells and specialized transporters which tightly regulate the immune cells and other substances that can enter the CNS. Immune cells pass through this barrier in three steps; rolling, activation and arrest on the endothelium. ICAM-1 and VCAM-1 are adhesion molecules that assist in rolling and can be upregulated with inflammation. Integrins are proteins which allow cells to enter into the CNS and one of the disease modifying therapies in MS, Nataluzimab, blocks the binding of these proteins to immune cells. Chemokines, primarily made by astrocytes, are expressed to attract T-cells and macrophages across the BBB, and can be upregulated in states of stress or inflammation.

B cells are less commonly associated with MS disease activity but could contribute to pathology [44]. They can form follicles in the meninges which have been associated with more rapid disease progression. B cells produce immunoglobulin and complement components and can potentially produce an immune response towards a specific target: MOG or MBP. However they may also have a non specific inflammatory response by upregulating general immunoglobulin production secondary to WM injury. In a pro-inflamatory state, they can produce TNF and lymphotoxin and may also be important in the anti-inflamatory state by producing IL-10. Mature B-cells express CD20, particularly in follicles, which is a target of Rituximab.

Peripheral macrophages and microglial cells are traditionally thought to have a secondary response in MS pathology where their action is primarily scavenging myelin and other cellular debris. However they may have an earlier or different role in MS pathogenesis which could precede lymphocyte infiltration [45]. They are thought to mediate damage with the production of proteolytic and lipolytic enzymes, complement components, cytotoxic cytokines, and NO and free radicals. Macrophages cells phagocytize opsonized and nonopsonized myelin and contain various lipoproteins at different stages of inflammation, which can be used to classify postmortem MS lesions.

Oligodendrocytes and their associated myelin sheaths that encircle axons are lost over the course of the disease. Myelin provides a variety of support to axons including a mechanism for saltatory conduction through nodes of Ranvier, physical protection, and trophic support. After acute focal inflammation, surviving oligodendrocytes can undergo repair where new myelin sheath is generated through cellular protrusions. Alternatively, oligodendrocytes can be replenished from nearby pre-

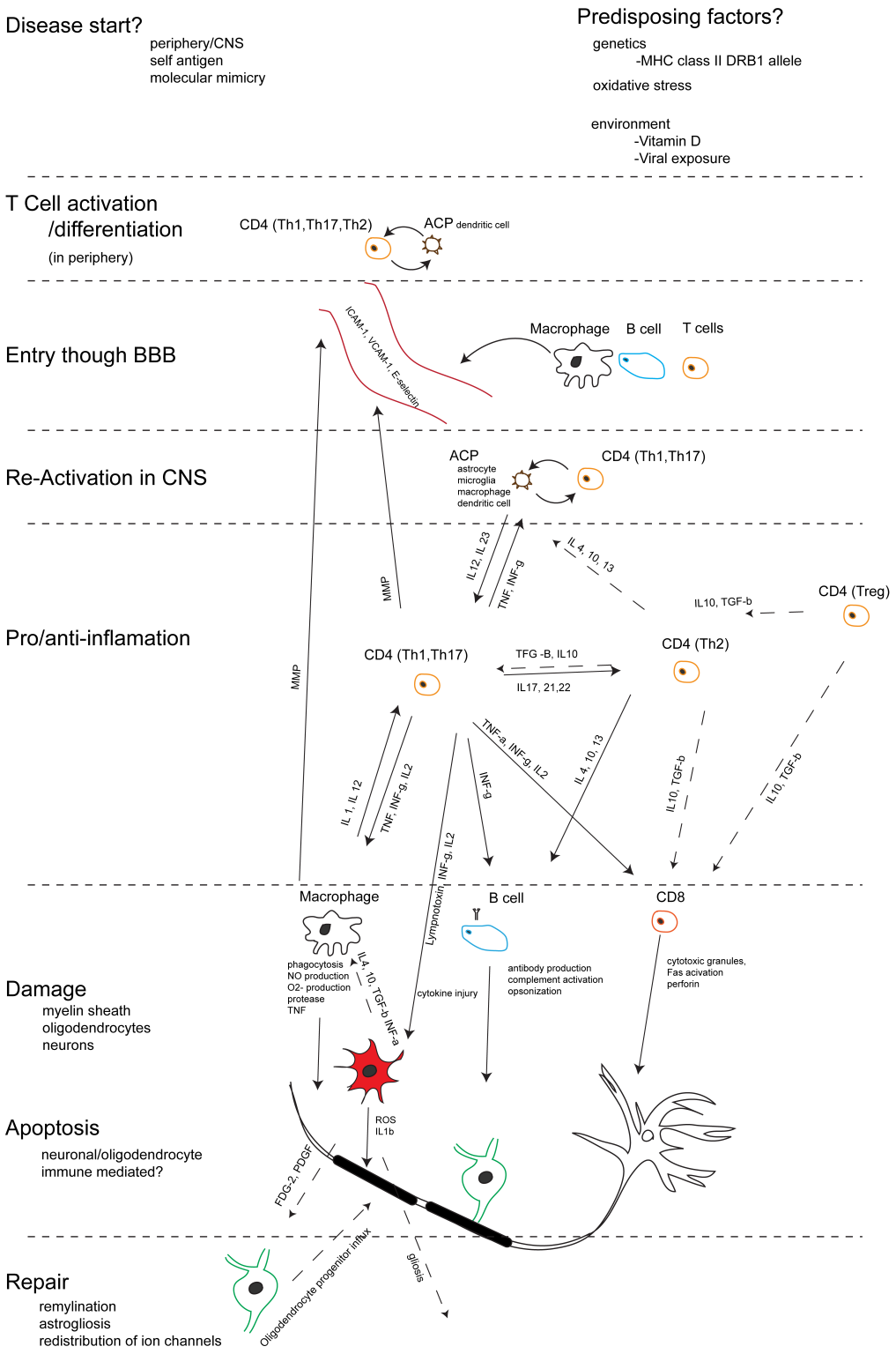

Figure 1.10: Illustration of immune mediated pathology in MS

cursor cells that are stimulated to differentiate and propagate. Damage to myelin and oligodendrocytes primarily arises from pro-inflammatory cytokines, oxidative

stress and excitotoxicity. This includes TNF, lymphotoxin, compliment, and perforin. Damage is incurred from both CD8 cells and macrophages but could also result from intrinsic dysfunction.

Astroctyes have several biological functions including supporting the BBB, maintaining ion balances and transporting various substances through the CNS. They can become reactive due to any inflammatory process [38]. Histologically this involves enhancement of the cytoplasm, increased cellular protrusions, and increased GFAP expression which functions to aid in cell communication and BBB function. Reactive astrocytes can contain myelin debris, express histocompatibility antigens, and contain lysosomal enzymes which are features suggestive of active involvement in the disease process. In chronic MS tissue, astrocytes form a dense fibrillary network to fill in the absence of other cells. Interestingly, astrocytes can even be damaged in severe lesions.

Neuronal dysfunction is an increasingly studied feature in MS [44]. In MS, fewer axons are present both within plaques and in normal appearing white matter (NAWM) tissue. Decreased density of axons likely occurs over the course of the disease beginning with early axonal loss during acute inflammation. With myelin loss, naked axons are susceptible to damage from ROS, and proteases. There are a number of mechanisms for neuronal and axonal injury in MS including direct damage by CD8 cells, macrophages, glutamate excitotoxicity, and antibody mediated injury. Later in the disease, neurodegeneration can result from non inflammatory factors such as mitochondrial dysfunction, glutamate mediated excitotoxicity, loss of trophic support from absent myelin or synapses, and energy imbalance from ion channel redistribution and channel dysfunction.

General cellular stresses in MS can lead to accelerated disease. These stresses include loss of trophic support, altered perfusion and decreased oxygen utilization, dysfunctional mitochondria, and decreased brain metabolism. These, in combination with depletion of antioxidants such as glutathione, make the brain more susceptible to iron-catalyzed oxidative damage.

Pathology Types

Pathologically, MS can be classified by lesion type or general tissue changes based on disease stage; either progressive or relapsing [46]. Bo and Trapp developed a staging system based on postmortem samples, that classifies lesions into active, chronic active, and chronic inactive. Lassman and Bruck, classify lesions, based on in vivo biopsied samples, into 5 types; early active, late active, inactive, early remyelinating, and late remyelinating.

Early lesions demonstrate infiltration of magrophages and microglia containing

MOG and MAG then later MBP and PLP. There are fewer oligodendroctes and more oligodendrocyte precursors with decreased myelin density compared to normal white matter. As well, acute axonal transport deficiencies are indicated by APP accumulation. Generally, these early lesions are hypercellular with inflammatory cells including magrophages and lymphocytes. Chronic lesions are hypocellular with few mature oligodendrocytes, astrocytes form a gliotic scar, and axonal loss can be up to 70%. The abundance of T cells and macrophages is decreased as well. Chronic active lesions, a type of lesions temporally connecting early and chronic lesions, have a central region that displays a chronic phenotype with a border that shows an active phenotype.

Four patters of lesion development have been identified, each of which may represent different pathogenesis [47]. Type 1 lesions show inflammation and demyelination with the presence of immune cells dominated by T-cells and macrophages. Type 2 lesions have the same features as type 1 lesions but additionally demonstrate immunoglobulin and complement deposition. Type 3 lesions show a loss of myelin in a proximal distribution along oligodendrocyte processes. Type 4 lesions are rare but appear to be mediated through primary oligodendrocyte dystrophy and subsequently an absence of remyelination.

Grey matter lesions are becoming increasingly recognized as a pathological feature of MS [47]. However, they are difficult to study in vivo as detection is difficult with standard MRI. Histologically, cortical GM lesions are less inflammatory with fewer T-cells and macrophages compared to WM lesions. There are three types of cortical GM lesions: type 1 lesions span the GM and WM boundary, type 2 lesions are confined within the cortex, and type 3 lesions form below the pial layer of the meninges on the surface of the cortex. Ectopic B cell follicles in type 3 lesions have been associated with more rapid overall disease progression however these are especially difficult to study with MRI because of partial volume effects with CSF near the cortical surface. Grey matter lesions are more common in progressive forms of MS, but they can develop in the earliest stages of RRMS as well. Furthermore, these lesions correlate more strongly with cognitive disability compared to white matter lesions.

Progressive MS exhibits different tissue characteristics compared to the relapsing remitting phase. There is seemingly little inflammation on MRI yet histologically, inflammation and demyelination are still abundantly present. Diffuse T cell infiltration, microglial activation, axonal transport disruptions, and widespread leakage of the BBB are important features of the progressive phase in opposition to relatively punctate changes in the relapsing remitting phase. Despite these differences, it seems that the myelin repair mechanism is similar to that of RRMS. Clinical features that differentiate the progressive from the relapsing phase may arise from

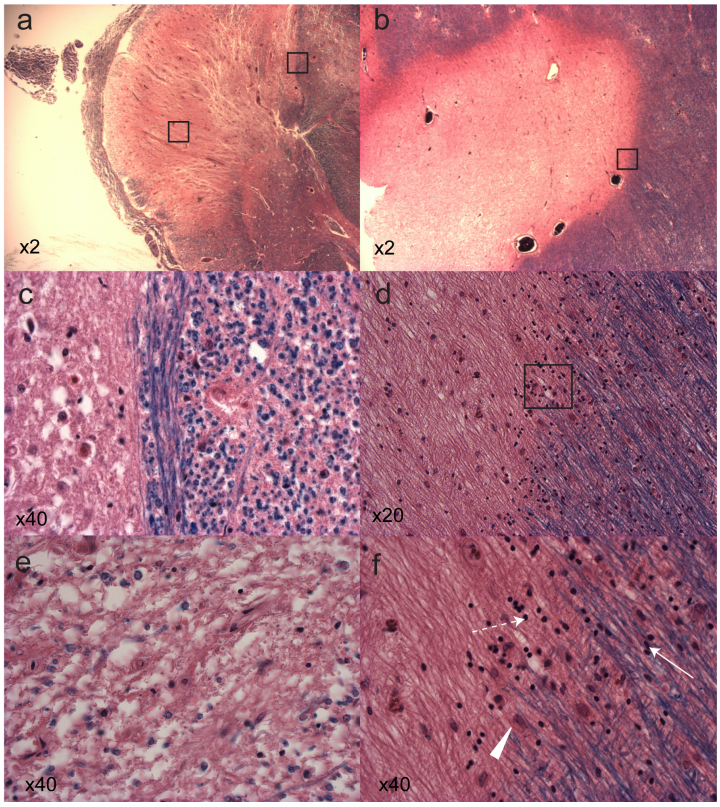

Figure 1.11: Chronic inactive MS spinal cord lesion (a,c,e) and chronic active MS cerebral lesion (b,d,f) stained with H/E and LFB. The chronic inactive lesion displays a hypocellular center (a,e) with absence of myelin staining and inflammatory cells with a clearly defined plaque border (a,c) with few inflammatory cells and sparing of myelin outside of the lesion. The chronic active lesion has a hypocellular center (b,d) with a hypercellular border (d,f) and a non distinct myelin edge indicating active inflammation and demyelination. The hypercellular border (f) shows cells displaying morphology consistent with MS including reactive astrocytes (arrowhead), lymphocytes (dotted arrow), and elongated microglia (arrow). All magnifications are further multiplied by 10x.

exhaustion of repair and neuroplastic mechanisms or though a parallel degenerative process.

Deep grey matter dysfunction is becoming an increasingly recognized aspect of pathology in MS yet many questions remain unanswered. This will be discussed extensively in different sections: Deep Grey Matter and Iron.

Though there are many pathophysiologic processes in MS which can be classified based on various features, a full understanding of the disease is elusive as access to human brain tissue is rare. MRI offers opportunities to examine some features of the disease, with new research methods becoming increasingly specific to individual disease processes. Conventional MRI methods that focus on lesions are the mainstay of clinical use, trial outcomes, and some research areas because the methods are

robust, features of MS are generally distinguishable, and a large amount of data has been accumulated over time. Yet many lesion centric MRI measurements show poor correlation to clinical disease progression or to specific biomarkers. MRI methods cannot observe intricate features of the disease such as cytokines, antibodies, and changes in individual cell populations but new methods are becoming more specific for certain pathological features such as macrophage tagging with SPIO, MWF mapping of myelin, and methods for imaging iron. The end goal of research in these imaging areas is to develop more specific methods of studying the disease.

1.4 Deep Grey Matter

1.4.1 Deep Grey Matter Function

There are several subcortical grey matter nuclei including the basal ganglia, thalamus, red nucleus, and dentate nucleus [48]. The basal ganglia structures include the striatum (caudate nucleus and putamen), globus pallidus, subthalamic nucleus, substantia nigra, and amygdala. These nuclei contain neuronal cell bodies with afferent and efferent connections to other parts of the CNS including the cortex, brainstem, other subcortical nuclei, and the spinal cord. Each nuclei contains few to several different types of neurons and different types of neurotransmitter receptors.

The basal ganglia is responsible for regulating motor function, different aspects cognition, procedural learning, and emotional functions [49]. There are many parallel loops in the basal ganglia where the overall function can be modelled as a segregated circuit with some loop overlap. Feedback often modulates cortical areas or nuclei related to the input origin after processing in specific areas of the basal ganglia. Five major parallel circuits have been identified: a motor circuit, an oculomotor circuit, a dorsolateral prefrontal circuit, a lateral orbitofrontal circuit, and an anterior cingulate circuit. There are two major output nuclei of the basal ganglia which include the internal segment of the globus pallidus and substantia nigra pars reticulata whereas the main input is the striatum (putamen and caudate) and subthalamic nucleus. All of the intrinsic and output projections of the basal ganglia are GABAergic and inhibitory except for the excitatory glutamatergic subthalamic nucleus efferent projections. The motor loop in the striatum is linked to the output nuclei through direct and indirect pathways which originate from different striatal projection neurons and whose action is dependent on the cortical inputs. The indirect pathway disinhibits the inhibitory output of the basal ganglia while the direct pathway has the opposite effect.

Areas of input into the striatum can be divided roughly into three territories including sensorimotor, associative or cognitive, and limbic regions. Cortical input connections arise from related cortical areas with the neurotransmitter glutamate.

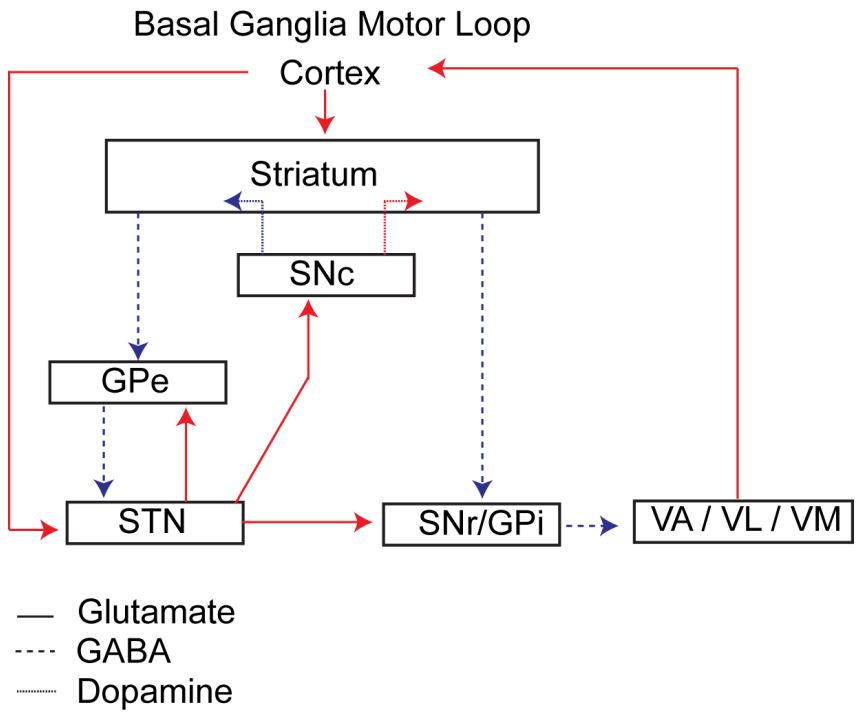

Figure 1.12: Figure of the motor loop in the basal ganglia showing the direct and indirect pathways (red = excitatory, blue = inhibitory). Striatum = caudate nucleus and putamen, SNc = substantia nigra pars compacta, SNr=substantia nigra pars reticulata, GPe= external segment of globus pallidus, GPi= internal segment of globus pallidus, STN = subthalamic nucleus, VA = ventral anterior nucleus, VL = ventral lateral nucleus, VM = ventral medial nucleus (VA,VL,VM within the thalamus)

Several regions of the thalamus are inputs to the striatum with neurotransmitters glutamate and aspartate. The centromedian nucleus of the thalamus projects to sensorimotor areas of the striatum, the parafasicular nucleus projects to associative areas of the striatum, and the ventral lateral nuclei overlap with corticostriate projections. A dopaminergic input arises from the midbrain nuclei including the substantia nigra pars compacta and ventral tegmental area. Other inputs to the striatum arise from the raphe nuclei (serotonergic) and the locus coeruleus (NA). There are several clinical findings of specific dysfunction to one input into the basal ganglia. Areas of the caudate nucleus head receive afferents from the prefrontal cortex and dysfunction in this area, as observed in Huntington's disease, causes cognitive deficits. Areas of the putamen receive afferents from the motor and somatosensory cortecies and dysfunction in this area causes positive motor symptoms such as chorea. Loss of dopaminergic neurons in the SNc in Parkinson's disease results in negative motor signs and negative changes in affect. As well, the ventral striatum receives afferents from the limbic system and hippocampus and local dysfunction leads to changes in affect. Since many basal ganglia structures form

inner loops with each other, dysfunction in one nuclei can have a cascading effect of function to one or several additional nuclei.

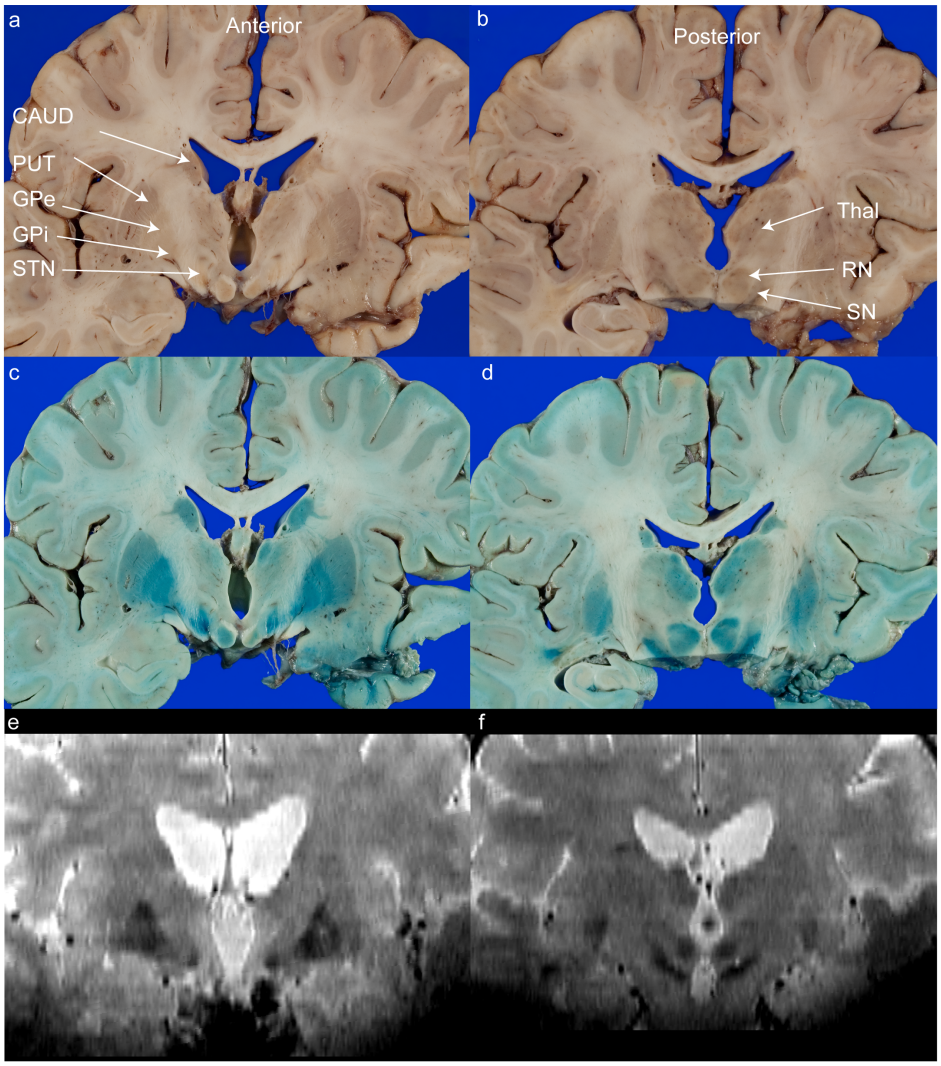

Figure 1.13: Coronal section of human brain through the deep grey matter (a,b), iron staining of the same section (c,d), and T_2 weighted Fast Spin Echo high field MRI of deep grey matter regions (e,f).

The internal loops of these circuits connect to various basal ganglia regions. Both segments of the globus pallidus receive GABAergic input from the striatal neurons with the direct motor pathway innervating the GPi and the indirect motor pathway innervating the GPe. As part of the indirect pathway, the subthalamic nucleus receives afferents from the GPe, in addition to cortical afferents, and projects to the GPi and SNr. The SNc provides dopaminergic input into the striatum and receives minor reciprocal afferents. The SNr and GPi contains GABAergic neurons and both provide the output of the basal ganglia. In addition, the SNr is responsible for the functioning of some eye movements and involvement in cognitive processing

in addition to its role in movement.

Major output afferents project to thalamic nuclei including the ventral anterior, ventral lateral, dorsomedial, and intralaminar nuclei. These thalamic nuclei link basal ganglia output to the motor, supplementary motor, premotor, prefrontal, and limbic cortices. Other basal ganglia output targets include the mesencephalic pedunculopontine nucleus (locomotion, arousal, sleep, motivation, attention, and learning), the habenular nucleus (connects to the limbic system), and the superior colliculus (head and eye movements).

The thalamus is a particularly complicated structure with many anatomically and functionally distinct divisions in contrast to basal ganglia structures which have more diffuse regions [50] [51]. All sensory information into the cortex (excluding the olfactory system) passes through the thalamus. There are two different types of thalamic afferents; specific inputs have afferents mostly from ascending spinal cord pathways and project to the cortex, while regulatory inputs, which are the more prevalent type, influence how signals are processed. These come from either cortical or brainstem areas and are cholinergic, noradrenergic or serotonergic. The functional divisions of the thalamus can be classified as relay or association nuclei. Relay nuclei receive a well-defined input bundle and project to a specific cortical area. Association nuclei project to cortical association areas and are important for gating information between cortical areas. Inputs arise from the cerebral cortex and subcortical structures.

The red nucleus is located in the rostral midbrain and is involved primarily in cerebellar circuitry [51]. The red nucleus receives afferents from deep cerebellar nuclei and the cerebral cortex. The parvocellular region receives contralateral afferents from the dentate nucleus. The magnocellular region gives rise to the rubrospinal tract and receives contralateral afferents from the cerebellar cortex, the premotor cortex, and ipsilateral afferents from the precentral cortex. It is thought to have a role in normal arm swinging and shoulder movements by facilitating flexor motor tone.

These subcortical nuclei contain a higher concentration of iron, mostly in the form of ferritin, compared to other CNS locations and most accumulate iron at different rates, during normal aging [14] [52]. In neurologic disease, a higher concentration of iron has been demonstrated in both pathological analysis and with MRI methods in these deep grey nuclei. Only recently, mostly through MRI techniques, has iron been implicated in deep grey matter in multiple sclerosis.

There is a wide range of iron concentrations reported for all structures which could result from different techniques used to analyze iron (ASS, ICP, Colorimetry) or because iron content is variable throughout normal subjects.

Table 1.2: Normal range of iron content in deep grey matter

Structure	Iron Range (Fe/g ww)
globus pallidus	81-370
substantia nigra	45-185
red nucleus	194
putamen	76-164
caudate	56-117
thalamus	93
white matter	15-42

1.4.2 Deep Grey Matter Pathology in Multiple Sclerosis

Direct dysfunction of the basal ganglia and other subcortical nuclei are difficult to clinically evaluate in MS because lesions in white matter often mask or mimic pathology in deep grey matter. Therefore MRI has been used to evaluate structural changes in the deep grey matter in conjunction with physical, cognitive, and psychological testing to determine functional changes of these structures. Deep grey matter structures show differences in iron content, neurodegeneration, and other pathology that might not cause direct disability in MS but could represent a marker of overall disease activity. Many of these features can be indirectly evaluated with different MRI methods.

In MS, the basal ganglia and other deep grey matter structures are mostly investigated with MRI with few studies using animal models, postmortem human tissue, or nuclear medicine examinations. MRI studies conclude that different features including atrophy, diffusion, fMRI, NMR, and relaxation changes are correlated with clinical outcomes such as cognition, disease duration, and EDSS. It has been speculated that increases in R_2 and $R_2^\star$ relaxation measurements are related to iron accumulation, atrophy is related to glial or neuronal loss, and diffusion/isotropic increases are related to cellular loss, edema, or demyelination. Furthermore, many of these MRI measures have relationships to one another which could indicate that various pathological processes are closely related or perhaps causative.

Throughout various studies, many deep grey matter structures have shown differences compared to control subjects with MRI measurements. However the most commonly involved structures are the caudate nucleus and putamen which could be due to dysfunction of afferent connections from the cortex, which when damaged, could precipitate pathology through a loss of trophic support, excitotoxicity or other factors. Atrophy is the most commonly studied aspect of the deep grey matter with MRI possibly because T_1 weighted sequences have high contrast at clinical magnetic field strength, are fast to obtain, and segmentation software is readily available. Few MRI studies examine the substantia nigra and red nucleus, possibly because cognitive outcomes are the most common functional comparison and these

structures are not traditionally associated with cognition. As well, automatic brain segmentation methods do not segment these structures because they are not visible with T_1 imaging so there may be an overall study bias.

While grey matter histologic examination is gaining interest in MS, the focus remains on cortical grey matter. Deep grey matter lesions are markedly different from cortical lesions with the former having a stronger inflammatory profile [53]. Deep grey matter demeylination is frequent, especially in the caudate nucleus and thalamus with less inflammatory cells, less axonal damage, and less gliosis compared to WM lesions [54]. Interestingly, deep grey matter lesions may be initiated and propagated through different mechanisms compared to both WM lesions and cortical GM lesions. As well, neuronal loss associated with lesions seems to be more pronounced in the deep grey matter than in the cortical grey matter and could be due to primary or secondary mechanisms including retrograde degeneration, transynaptic mechanisms, or immune cytotoxicity [55].

Nuclear medicine studies examine FDG in deep grey structures. These studies compare glucose metabolism between patients and controls as well as examine correlations between glucose metabolism and fatigue or memory. Glucose metabolism is reduced in the thalamus, cerebellum and parietal cortex in patients with MS [56]. As well, glucose hypometabolism correlates with memory dysfunction in the thalamus [57]. Fatigue is associated with reduced glucose metabolism the prefrontal cortex, supplemental motor area, and putamen, all of which could be associated with each other through basal ganglia circuitry [58].

Animal studies can provide a more complete investigation of basal ganglia pathophysiology in MS as invasive procedures are possible. There are changes in cannabinoid receptors in the deep grey matter in EAE which are associated with motor behaviour, cognition, learning and memory [59]. As well, cuprizone injections into the basal ganglia in mice show increased fatigue, cognitive dysfunction, and movement disturbances which represent the demyelinating aspect of deep grey matter dysfunction [60]. The somatostatin receptor-effector system in the striatum is disrupted in EAE which is linked to movement control and implicit memory. Even with the findings of animal studies, it is unclear whether deep grey matter dysfunction arises from primary or secondary pathogenic processes in MS [61]. Both mitochondrial dysfunction and axonal transection in WM can lead to hypoxic states which could cause indirect deep grey matter dysfunction through subsequent retrograde axonal degeneration. Conversely, direct neuronal damage can occur in the striatum as glutamate expression in EAE increases because of reduction in the inhibitory neurotransmitter GABA .

Basal ganglia pathology in MS is poorly understood. MRI is the most frequent method for studying dysfunction, especially in humans, yet a consensus on what

regions are affected and how specific pathologic mechanisms relate to MRI measures has not been clearly established. As with WM pathology in MS, GM pathology seems quite heterogeneous and likely arises from several pathological pathways.

1.5 Iron

1.5.1 Iron Physiology

Iron is critical in different processes in the human body including hemoglobin synthesis, neurotransmitter production, DNA synthesis, myelination, and mitochondrial function [62]. Overall body regulation of iron requires an interplay between iron absorption, recycling, and loss. Furthermore, iron in the brain is regulated both by the BBB, and at the cellular level. Normal iron content of the body is approximately 3 to 4 g with the majority (2.5g) incorporated into hemoglobin molecules in red blood cells and developing erythroblasts, 400mg in iron containing proteins, 3-7mg in transferrin bound iron in the plasma, and the remainder stored in ferritin or hemosiderin.

Iron is absorbed through duodenal enterocytes as primarily free iron. It is transported mostly as ferrous iron through DMT1 transporters on the luminal side. On the basolateral cell surface, iron is transported into the circulation by ferroportin, the only known cellular iron export channel. Hepcidin, a protein produced in the liver, interacts with these ferroportin channels to control entry of iron into systemic circulation. Hepcidin is produced when high systemic levels of iron are detected and serves to down regulate ferroportin activity. When iron is released from ferroportin into circulation, ferrous iron is oxidized to ferric iron by ceruloplasmin or hephastin. This free ferric iron is quickly bound by plasma transferrin for transport within the vascular system.

Gastrointestinal iron absorption is pathologically increased in disorders that cause ineffective erythropoiesis such as beta thalassemia, myelodysplastic syndrome, or in conditions that cause improper iron sensory signalling such as hereditary hemochromatosis [63]. However, brain iron is tightly regulated by the BBB and is only increased in the later stages of these diseases.

When RBCs are broken down in the reticular endothelial system, iron from hemoglobin is recycled by macrophages and released into systemic circulation by ferroportin or stored in ferritin according to concentrations of hepcidin[63]. There is no mechanism for regulated iron loss. It is thought that iron is lost through sweat, shed skin, and shed gastrointestinal cells.

Iron is tightly regulated in the CNS, beginning with the entry point, the blood brain barrier [64]. Brain vascular endothelial cells (BVEC) express transferrin receptor 1 (TfR) on their luminal surface. When many of these receptors bind iron

loaded transferrin, endocytosis occurs. This is followed by acidification of the newly formed endosome which releases iron from transferrin. Iron is then exported through DMT1 into the cytoplasm of BVEC then exported on the basolateral cell surface by ferroportin into the CNS. Iron is exported from the CNS by absorption into the venous drainage system through the arachnoid granulations.

Astrocytes seem to regulate the distribution of iron in the CNS. Astrocytes do not express TfR but can uptake iron through DMT1 which is polarized to foot processes near the BBB [65]. These foot processes express ceruloplasmin which oxidizes ferrous iron to ferric iron, enabling the binding of transferrin. As well, astrocytes release ATP and other nucleotides which may be involved in release of iron from BVEC. Furthermore, these foot processes can also form direct connections to neurons to regulate iron distribution.

Iron is required by neurons primarily for ATP generation and neurotransmitter production. Iron uptake occurs through both TfR mediated endocytosis and DMT1 and TRPML1 channels. As well, iron uptake could be facilitated through other means such as iron-citrate or iron-ATP binding complex, voltage-gated calcium channels, or through the uptake of ferritin through the binding of TfR or ferritin (Ft) receptor. Although neurons use large quantities of iron, their storage function of iron is minimal.

Oligodendrocytes are the main storage site of iron in the CNS WM. These cells can bind and uptake ferritin through ferritin receptors for rapid use of large amounts of iron, particularly for highly metabolically active processes such as myelination. For this process, iron is required to generate ATP and fatty acids. In addition to iron storage, oligodendrocytes produce the majority of CNS transferrin for interstitial transport.

Iron homeostasis must be tightly regulated within the CNS because free iron in the ferric form can serves as a reagent in the Haber-Weiss reaction while free ferrous iron can undergo the Fenton reaction, both of which generate free radicals[65]. Furthermore, iron deficiency can adversely affect cellular division in neuronal precursor cells, astrocytes, and oligodendrocytes. At the cellular level, iron storage, release, uptake, and export are regulated by iron responsive proteins (IRP) which interact with iron responsive elements (IRE) on mRNA. These mRNA segments code for proteins that interact with iron including ferritin, ferroportin, TfR and DMT1. With low levels of intracellular iron, IRP binding to IRE regions is increased which results in an increase of DMT1 and TfR expression and a decrease in ferritin and ferroportin expression. Iron to be utilized by a cell can be directed to one of three areas: use in the cytosol labile iron pool, storage in ferritin, or delivery to mitochondria.

Ferritin is a spherical protein that consists of four subunits of the H or L type. H ferritin is commonly found in cells requiring high iron turnover while L type ferritin

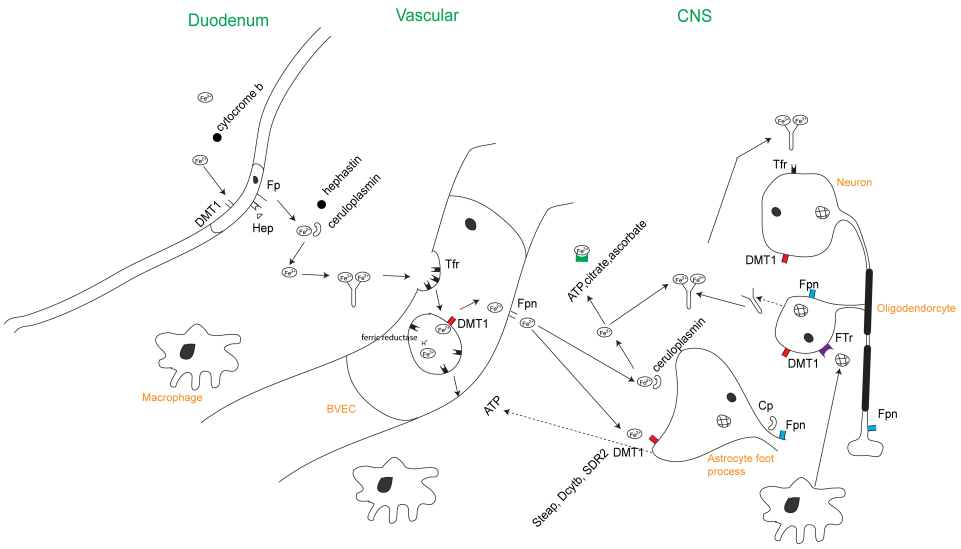

Figure 1.14: Diagram of iron transport in the CNS. Ingested iron is mostly ferric which is converted to ferrous iron before transport across duodenal enterocytes. Hepcidin controls ferroportin activity and absorption into systemic circulation. In the vascular system, ferrous iron is converted to ferric iron by hephastin or ceruloplasmin. Subsequently, transferrin binds 2 molecules of ferric iron for vascular transport. On brain vascular endothelial cells, transferrin binds transferrin receptor and undergoes endocytosis. Vacuoles release ferric iron and ferric reductase converts the iron to ferrous form. Iron is exported into the cytoplasm by DMT1 and exported into the CNS by ferroportin. The ferrous iron is rapidly converted to ferric iron by ceruloplasmin on astrocyte foot processes or transported into astrocytes by DMT1. Interstitially, ferric iron is bound by transferrin which is made by oligodendrocytes or as non-transferin bound iron (NTBI) with molecules such as ATP, citrate, or ascorbate. NTBI ferric iron is released and converted to ferrous iron to enter cells through the channels Steap, Dcytb, or SDR2 on cellular surfaces. Most neuronal iron is uptaken primarily as transferrin bound iron. When large amounts of iron are required, oligodendrocytes can uptake ferritin stored iron through ferritin receptors or TfR.

is associated with iron storage. Ferritin is also an acute phase reactant and can be increased in MS when iron levels are not elevated. Furthermore, ferritin can serve as an iron transport mechanism by moving large volumes of iron along axons to synapses where energy requirements are high. As well, ferritin may transport iron interstitially within the CNS to developing or reactive oligodendrocytes for myelin production.

Mitochondrial iron is needed for synthesis of iron sulphur clusters, fatty acid oxidation, cholesterol synthesis, heme prosthetic groups and ATP generation [66]. Iron is delivered to mitochondria either by chaperone molecules such as phosphate or citrate or delivered directly through fusion of Tf containing endosomes with the mitochondrial membrane. Subsequently, the transporter Mitoferrin delivers iron across

the inner membrane into the matrix. After import, iron is stored in mitochondrial ferritin or used in the generation of iron sulpher clusters or heme. Important iron sulphur clusters include complex I-III in the electron transport chain, ferrochelatase which is involved in heme synthesis, enzymes for pyrimidine/purine metabolism, NTHL1 which is a DNA repair mechanisms, and IRP1 which regulates cellular iron homeostasis. Mitochondrial ferritin does not contain an IRE and the mechanism of regulation is unknown.

1.5.2 Iron in Multiple Sclerosis

Iron is associated with tissue pathology in multiple sclerosis in both the deep grey matter and within lesions [67]. Deep grey matter iron is most commonly evaluated with MRI studies precluding cellular localization [68]. In white matter, postmortem tissue microscopy studies show iron is increased in macrophages and microglia within and surrounding lesions [69, 70, 71, 72]. Animal models often seem unsuitable for studying iron in MS as many models do not closely resemble the classical RRMS disease course as EAE shows a domination of spinal cord symptoms. As well, in vitro analysis does not probe the system as a whole yet can offer insight into specific aspects of iron pathways. New MRI methods could prove useful for better understanding the role of iron in MS with living human patients.

Iron Damage in Multiple Sclerosis

Iron can precipitate tissue damage and pathology in MS primarily through three mechanisms. Excess iron can damage tissue directly, amplify damage by macrophages, and impair mitochondrial function [65, 67].

Excess brain iron causes direct tissue damage through several mechanisms where iron rich regions such as subcortical nuclei are most susceptible to neurodegenerative iron damage [62]. Increased free iron can generate free radicals through the Fenton and Haber-Weiss reactions which can damage DNA, proteins, and lipids. Furthermore, iron can compromise DNA integrity through direct binding and can inhibit DNA repair mechanisms through free radical damage. Excess iron has also been shown to affect apoptosis signalling pathways including AP-1, and MAPKs. Glial cells such as astrocytes and particularly oligodendrocytes are susceptible to mitochondrial dysfunction and oxidative stress in the presence of excess iron. Axonal injury leading to transection is enhanced in the presence of iron which leads to neurodegeneration. The negative consequences of iron can be amplified through a positive feedback loop where oxidative stress from excess iron can trigger the release of more iron from ferritin, heme proteins, and iron sulphur clusters which further escalates dysfunction.

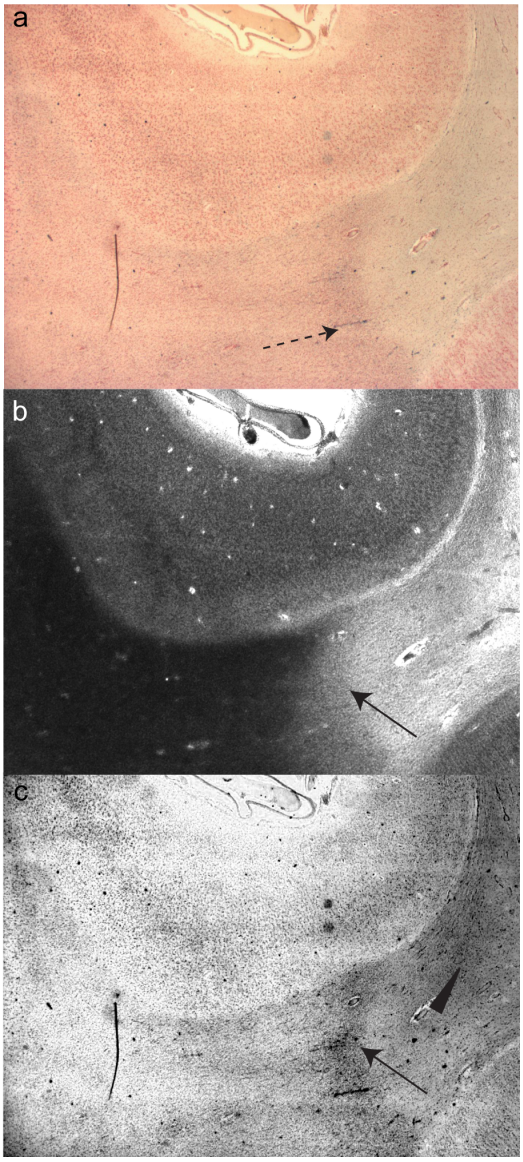

Figure 1.15: Chronic active MS lesion (20x) stained with (a) Perl's iron stain with Nuclear Fast Red counterstain (b) Weil's stain for myelin indicating active demyelination with non distinct lesion border, (c) red colour spectrum of iron stain more clearly depicts regions of increased iron. Iron stains both within the lesions (arrow head) and more intensely at the plaque border where active demyelination is occurring (arrow). There are numerous lines of iron (dotted arrow) which could be within or along axons or blood vessels.

Macrophages are thought to accumulate iron from the phagocytosis of RBCs or myelin. In healthy tissue, the cytoplasm of oligodentrocytes along with inner and outer loops of myelin are enriched with iron which can become liberated in oligodendrocyte dysfunction or damage. Extraverted blood cells have been shown in or near MS plaques and macrophages could phagocytize the resulting hemosiderin de-

posits. Enhanced levels of inflammatory cytokines are produced by macrophages in the presence of elevated iron levels including TNF, IL-1 and MMP-9 which can cause BBB dysfunction. Macrophages also exhibit activation of NF-kB, and increased reactive oxygen species (ROS) production. These factors could contribute to a higher rate of oligodendrocytes or neuronal damage directly from macrophage activity or through stimulation of other inflammatory cells. Resulting oxidative modification of proteins or peptide fragments generation could then undergo antigen presentation and precipitate the lymphocytic aspect of disease. On the surface of microglia, transferrin receptor is upregulated and iron uptake is enhanced in both hypoxic states and with increased levels of inflammatory cytokines. Although excess iron within magcrophages/microglia is associated with MS pathology, it is unclear whether iron is taken up primarily in the CNS or iron rich macrophages are trafficking from the periphery. Likely there are many aspects of iron physiology that are disrupted in MS which are associated with macrophage activity.

Mitrochondrial stress due to excess iron could contribute to neurodegeneration. In order to meet energy demands near MS plaques, dysfunctional mitochondria could undergo biogenesis which results in more dysfunctional mitochondria. This effect could result in overall enhanced neuronal iron uptake resulting in greater free radicle production if iron is not sequestered properly. Mitochondria are likely susceptible to the same iron mediated dysfunction as other cellular elements such as DNA disruption, protein damage, and lipid damage however mitochondria may be affected earlier due to higher local iron demands compared to other cellular components. Since the regulation of the mitochondrial iron storage protein is different than cytosolic regulation, it may be independent of local iron concentration or respond differently to subtle iron concentration changes. In addition, the mitochondrial protein mitochondrial-aconitase, can be a source of Fenton reactants which can exacerbate free radicle production in the presence of increased iron.

Reasons for Increased Iron in Multiple Sclerosis

Iron misregulation can directly cause pathology in several disorders such as PKAN or hereditary aceruloplasminemia however this likely not the case in MS [65] . In animal models of MS, there is a time period of weeks or days after the initial insult until iron accumulation is observed, indicating that iron accumulation is a reactive phenomenon [73, 74]. CSF iron is not increased in subjects with MS which could indicate that iron misregulation or dysfunction is a local phenomenon within certain brain regions. At the subcellular level, iron regulatory proteins seem to be influenced by inflammatory cytokines in MS including INF-gamma. As well, DMT1 has an isoform that is influenced by inflammatory regulation because it contains an

INF-gamma element, a AP-1 binding site and a NF-kB binding site which could further facilitate local iron transport.

Vascular changes in MS are associated with iron accumulation and deposition. Trafficking of immune cells and damage to the BBB could result in extravasation of RBCs into the CNS, leading to iron accumulation in the form of hemoglobin or hemosiderin from RBCs [71]. As well, iron uptake could be enhanced across BVECs because of increased metabolic demand during processes such as myelinogeneisis and acute inflamation. Alternatively, hypoxia in MS can result in decreased blood flow and inadequate oxygenation of tissue. Hypoxia could arise from mitochondrial dysfunction and subsequent compensatory biogenesis could result in increased iron requirements. Decreased oxygenation could also result in expression of hypoxia-inducible factor-1 causing up-regulation of both transferrin receptor and DMT-1 [67].

Iron in Grey Matter

Deep grey matter iron evaluation in MS has only gained substantial interest in the last 10 years with the advent of improved MRI technology. Currently, MRI can show changes in iron concentration in MS relative to control subjects but cannot localize iron to specific cells. In addition, MRI is capable of investigating temporal iron changes in human MS subjects, yet studies of this nature are lacking. Previous cross-sectional studies have correlated MRI iron quantification to various clinical outcomes including disease duration [75], disability measured by EDSS [76], cognitive impairment[77], and brain atrophy[78]. Iron sensitive MRI changes have been observed in most deep grey matter structures including the thalamus, putamen, caudate, globus pallidus, substantia nigra and red nucleus. However, there is variation between studies in MRI iron measurements in different brain regions . This could indicate that various MRI techniques are influenced by tissue components other than iron. In addition, the variation could arise from the individual study populations having different disease stages ranging from CIS to progressive MS, each of which likely show different iron levels. MRI cannot directly investigate the cause of deep grey iron changes, however, by relating MRI iron changes to disease aspects such as atrophy, lesions location, or disease stage, comparisons to several postulated theories developed from human histology, animal models, or in vitro work could identify the most likely relationships. The cause of iron accumulation in the deep grey matter could be from axonal transection leading to retrograde degeneration or a loss of trophic support. As well, a cascading effect of dysfunction could occur since there are many interconnections in the deep grey matter. Neurotransmitter metabolism defects could result in iron accumulation as iron is utilized as a cofactor

Table 1.3: Cross sectional iron evaluation of deep grey matter in MS using MRI

Author	B_o	Patient Type	Acq Method	Finding
Khalil et al [78]	3.0	35 CIS 78 MS 35 HC	$R_2^\star$ mapping	$R_2^\star$ related to atrophy in MS and $R_2^\star$ in CIS equivalent to HC
Hammond et al [75]	7.0T	19 MS 13 HC	phase imaging	caudate phase correlated to DD
Lebel et al [76]	4.7T	22 RRMS 22 HC	$R_2^\star$ mapping R_2 mapping phase imaging	pulvinar thalamus correlated to EDSS with 3 MRI methods
Ge et al [79]	3.0T	17 MS 14 HC	MFCI	MFC correlated with neuropsychological measure
Zhang et al [80]	1.5T & 3.0T	17 RRMS	relative T_2	T_2 correlated to EDSS in GP and Caud at 3.0T only
Ceccarelli et al [81]	1.5T	26 SPMS 35 BMS 25 HC	relative T_2	T_2 in globus pallidus and thalamus moderately correlated to EDSS
Bakshi et al [82]	1.5 T	80 RRMS 34 SPMS 100 HC	Score (0-3) of T_2 hypointensity	Correlation with disease duration and advancing neurological disability
Ceccarelli et al [83]	1.5T	13 HC 47 CIS	relative T_2	In CIS patients deep GM is not spared
Tjoa et al [84]	1.5T	41 RRMS 6 SPMS 15 HC	relative T_2	dentate nucleus T_2 associated with ambulatory dysfunction
Bakshi et al [85]	1.5 T	42 RRMS 18 SPMS	relative T_2	hypointensity associated with disability score in caudate and SPMS disease course
Burgetova et al [86]	1.5 T	970 117 HC	T_2 mapping	Differences in age and increased iron in MS
Ceccarelli et al [87]	1.5T	35 RRMS (paediatric) 10 CIS (paediatric) 14 HC	relative T_2	T_2 hypointensity in caudate between groups and related to lesion volume
Holst et al [88]	1.5T	18 RRMS 5 SPMS 23 HC	T_2'	T_2' decreases between MS and Controls throughout deep grey matter
Habib et al [89]	1.5T & 3.0T	31 RRMS 21 SPMS 122 HC	phase imaging	phase increases in MS patients relative to controls in deep grey matter
Khalil et al [90]	3.0T	RRMS 37 CIS 32	$R_2^\star$ mapping	putamen $R_2^\star$ correlated to disease duration and atrophy

CIS - Clinically Isolated Syndrome HC -Healthy Control

for dopamine synthesis and plays a role in dopamine degradation through regulation of MAO levels [91]. Iron has also been associated with glutamate regulation through NMDA receptors and GABA metabolism. It is also possible that increased deep grey iron results from the inflammatory aspect of the disease and is contained within microglia [69]. Initial MRI investigation of deep grey matter has consistently demonstrated increased iron compared to controls in roughly 15 studies (Table 1.3) but more focused MRI studies and human histological analysis are needed to uncover the causes and temporal changes of deep grey matter iron.

Iron in White Matter

Within WM lesions, iron is present both within macgrophages and oligodendrocytes as ferritin. Iron is also found in transected axons and along vessels in active and chronic lesions and in normal appearing white matter in MS. Patchy iron depositions in the form of hemosiderin within lesions and in NAWM have been identified as microbleeds due to blood vessel permeability changes[71]. Expression of the transferrin receptor is found within WM lesions and in the periplaque region indicating that cells are actively acquiring iron [69]. MRI has been used to study white matter iron deposition within and around lesions using SWI, phase, and $R_2^\star$ imaging and the results indicate that competing pathological processes make iron visualization with these MRI methods difficult. Furthermore, iron-enriched oligodendrocytes likely represent tissue repair while iron-enriched microglia indicate the presence of ongoing tissue destruction yet appear indistinguishable using MRI.

The role of iron in MS is not well understood. It is difficult to understand the pathobiology using MRI, animal models are limited, and iron may actually be protective in some cases. More histological analysis is needed to understand iron changes in WM and currently there are no studies that investigate iron in deep grey matter. MRI is successful in evaluating deep grey matter iron in healthy control subjects yet additional studies are needed to relate iron changes to disease aspects in MS such as atrophy, lesions location, and NMR measurements. Identification of substructure changes in addition to temporal analysis could more clearly identify causes of iron changes.

1.6 MRI to Evaluate Neuropathology

There are several MRI methods that examine tissue pathology in MS in both white matter and grey matter. Furthermore, there are several methods of evaluating brain iron with MRI. This section will examine the findings of other studies and potential issues with the MRI methods with regards to detecting pathological abnormalities, technical problems, or the overall usefulness in evaluating disease burden. These methods and findings will be compared to quantitative relaxation and phase measurements of deep grey matter in the next section.

1.6.1 Other MRI for Multiple Sclerosis

T_1 and T_2 weighed FSE images are primarily used for diagnostic purposes but have also been used to semi-quantitatively and morphologically evaluate lesion load with comparison to clinical measures. Individual T_2 lesion analysis offers limited use-

fulness in staging lesions because inflammation, demyelination, prominent neuronal loss, or gliosis have a similar hyperintense T_2 appearance. As well, overall lesion load has a low correlation to EDSS (r=0.25, p=0.32)[92]. T_1 weighed MRI has been used to correlate black hole lesion intensity with axonal loss and lesion load with EDSS (r=0.52, p=0.004)[93]. As well gadolinium enhancing lesions show BBB dysfunction but do not correlate well with clinical scores. T_1 ring enhancing lesions are generally worse pathologically with more myelin and axonal loss [94]. An issue with T_1 and T_2 weighted FSE is the qualitative image contrast which is dependent on parameters such as TE, TR, flip angle profile, and type of RF pulse, making it particularly difficult to quantitatively and consistently evaluate lesions. Furthermore, lesion analysis may have a poor correlation to disease because of the inability to assess processes such as neuronal plasticity, repair, or extent of damage.

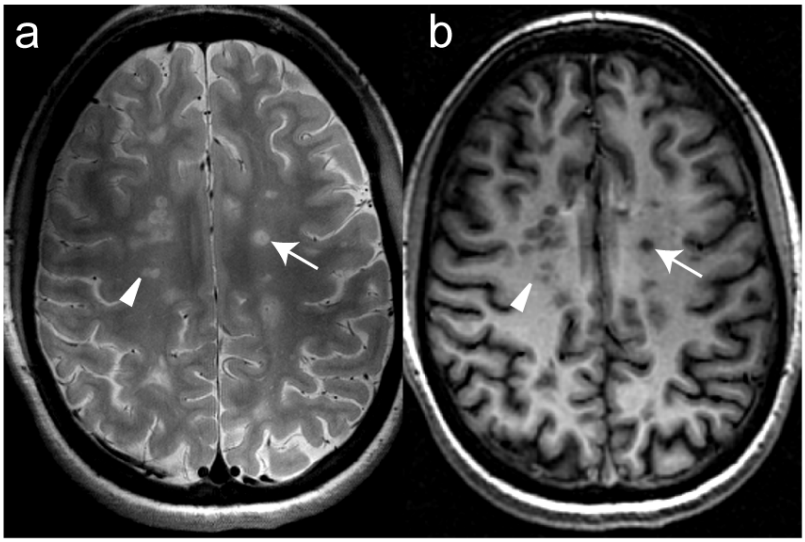

Figure 1.16: MRI lesion contrast in MS with a)T_2 weighted MRI, b)T_1 weighted MRI (MPRAGE) from 4.7T. Arrow head shows hyperintense T_2 lesions with hypointense T_1 lesion. Arrow shows hyperintense T_2 lesion with hypointense "black hole" T_1 lesion.

Atrophy measurements are used extensively for evaluating disease because they correlate well with neurodegeneration and cognitive scores, and automated software is readily available. Volume measurements of the global brain size, selective GM regions, cortex, and spinal cord have been associated with disability [94, 95]. Deep grey matter atrophy has been shown to occur in the caudate and thalamus

in RRMS and to a larger extent in SPMS in both cross sectional and longitudinal studies [96]. Care must be taken with atrophy measurements because the addition of disease modifying therapy or corticosteroids causes a reduction in edema and subsequently brain volume as measured with MRI[97]. Lesions can present problems as segmentation algorithms may inadequately distinguish certain tissue type such as periventricular lesions from ventricles. As well, regional atrophy due to disease can be problematic for segmentation techniques and volume measurements as algorithms are based on healthy brains. Furthermore, it is unclear if atrophy is related to neuronal or glial cell loss and neuroplasticity mechanisms cannot be evaluated. Although atrophy measurements are correlated to disability and show differences from controls in population studies, volume changes over time are subtle and may be undetectable in individual patients over a period of several years.

MTI is used to evaluate changes in brain tissue matrix. MTR decreases with a reduction in macromolecule content and can demonstrate loss of axons and myelin [98]. Normal appearing brain tissue also shows changes in MTI measures compared to controls which are not evident with standard MRI and could represent diffuse inflammation or tissue damage [99]. As well, a weak correlation exists between MTR measurements and disease duration in the deep grey matter [100]. MTR measures can have substantial variation with different imaging parameters and standardization can be an issue. Quantitative MTI is not a specific measure of any particular pathological process and changes may be difficult to interpret.

MWF measurements show a strong correlation to myelin density and are fairly specific to myelin [30]. Using a multicomponent fit, water signal can be separated into 3 components including myelin water (20 to 50ms), intercellular and extracellular water (100ms), and CSF (>1sec). However the distinction in relaxation times are somewhat arbitrary. Remyelinated tissue often has thinner myelin sheaths which would be shown as a reduced amount of myelin yet could still have normal function. Furthermore, this imaging method is time consuming and slice coverage can be limited as many echoes must be acquired for reasonable multicomponent fitting.

Pathologic processes that change the normal motion of water will show different MRI diffusion measurements including ADC and diffusion tensor imaging metrics (FA and MD). Neurodegeneration and demyelination in MS can change the direction of water motion, increase diffusivity, and generally decrease anisotropy. There is a correlation between the increased radial diffusivity and the severity of demyelination [101]. ADC values are shown to increase at NAWM locations where lesions subsequently occur and NAWM DWI measurements correlate with cognitive scores [102]. Diffusion is nonspecific and could represent loss of myelin, other glial cells, or axons.

MRS can provide quantitative measures of two features in MS; active inflam-

mation and neuronal degeneration [103]. N-acetylaspartate is related to neurons and their function, choline is related to cellular turnover, creatine represents energy utilization, lactate is a marker of anaerobic respiration, and myo-inositol is a glial marker. Within acute lesions, choline and lactate peaks are larger while creatine peaks are lower in more aggressive lesions. As lesions resolve, the levels of lactate and creatine decrease followed later by decreases in choline and myo-inositol. In subcortical grey matter, reduced concentrations of N-acetylaspartate and choline, and increased concentrations of myo-inositol are seen. MRS suffers from low signal to noise where many image averages must be obtained. As well, the spatial resolution is often poor which is problematic in MS because affected tissue regions are often punctate.

BOLD fMRI has been used to evaluate functional reorganization of the brain in MS in areas of motor and neuropsychological deficits. It is thought that substantial alterations in neuronal populations occur in the early stages of MS and reorganization is necessary to maintain brain function. Certain areas of the cortex are more activated in RRMS patients [96]. In early disease stages, increased activation of brain areas for a given task is observed, including the primary sensorimotor cortex and the supplementary motor area, which indicate more neuronal involvement is required for the same task as a healthy individual. Later in the disease, there is more widespread recruitment of additional areas indicating reorganization. fMRI is a time consuming process because subtle changes in blood oxygenation due to tissue metabolism can only be detected with multiple image averages. As well, neuroplasticity is poorly understood and changes may be person dependent and may not directly relate to disease.

1.6.2 Other MRI for Iron

There are several other MRI methods that have been suggested to evaluate brain iron, each of which have several notable differences to relaxometry methods and phase imaging.

Magnetic Field Correlation imaging is related to iron-induced microscopic field variations using asymmetric spin echos [104]. However this is a newer method with limited applications to MS. As with $R_2^\star$ mapping, background field sources from air tissue interfaces can cause a change in signal which is particularly troublesome for deep grey matter measurements.

Quantitative susceptibility mapping (QSM) requires several steps beginning with a processed phase image devoid of a background field [68]. This is problematic because unwrapping, and many background field removal methods perform poorly in areas of high noise or near the outer surface of the brain. As well, QSM requires division in k-space by the Fourier transform of a dipole point source which is an ill-posed

problem. Methods of overcoming this include multi-angle acquisition, thresholding the discontinuous k-space regions, or regularization but changes in certain parameters can drastically affect the results. Furthermore, reference values within the brain must be obtained as the absolute susceptibility cannot be determined.

Direct Saturation Imaging uses off-resonant RF saturation pulses that cause a reduction in the longitudinal tissue magnetization [33]. Similar to MTR, this method probably suffers from changes in parameters and could be hard to standardize.

FDRI has a very strong correlation to iron yet this method will probably never see clinical use and is difficult to implement in research studies [31] [105]. This is because at least two field strengths are needed which greatly increases scan time and cost. As well, variation in imaging parameters such as interecho spacing can affect quantitative R_2 measurements.

1.7 MRI Methods for Deep Grey Matter Iron Quantification in Multiple Sclerosis

There are several important reasons for using MRI to investigate deep grey matter iron in MS. Iron accumulation in deep grey matter is probably a slow, steady process while other aspects of the disease such as demyelination (and remeylination), inflammation, edema, and neurodegeneration can rapidly occur and similarly quickly resolve. Other imaging methods of WM have produced lower correlations to clinical disability possibly because they depict nonspecific inflammation which may not reflect overall disease burden. The underlying mechanisms of iron accumulation are not well understood but may represent global CNS dysfunction. Furthermore, studies of deep grey matter iron with MRI have shown a better correlation to EDSS, cognition, or other measures of disability compared to standard imaging methods. The anatomical location of deep grey structures is predictable which makes automatic segmentation methods, or manual tracing relatively fast and reliable. The role of iron in MS is unclear with a possible direct contribution to disease progression or benign accumulation in deep grey matter. Irregardless, it may be a biomarker of disease as measured with MRI. MRI methods must be first evaluated for their ability to measure deep grey matter iron and extensive assessment of their relationship to disease will require many patient studies.

There are several advantages of quantitative relaxation methods and phase imaging for evaluating deep grey matter iron. Phase imaging and $R_2^\star$ mapping are available on clinical systems while minor adaptations to T_2 weighted FSE can generate R_2 maps. Transverse relaxometry has a high correlation to brain iron in deep grey matter in healthy control subjects [106]. Furthermore, quantitative relaxation or phase measures are not subjective and can be reproducible, to an extent, even with

different parameters such as number of echoes, echo time, and resolution. Technical considerations of signal decay fitting with $R_2^\star$ mapping and R_2 mapping are important. A contribution to $R_2^\star$ relaxation results from susceptibility differences at air tissue interfaces which could affect evaluation of endogenous tissue iron. R_2 relaxation can be difficult to measure from signal decay as stimulated echoes can occur over multiple refocusing pulses. Phase imaging is influenced by several factors including the background phase removal method used, object shape, and head angle relative to the main magnetic field. Many of these issues have been addressed in previous works [107, 76] and variants of each method have been extensively used in neurological diseases, leading to a wide base of literature which supports their future development and current utility.

Although these quantitative MRI methods show promise for use in MS there are further issues that preclude their appropriate and reliable use. Phase imaging has problems with background phase removal and non-local field influences of iron containing structures. Therefore the evaluation of several conditions of deep grey matter phase imaging should include appropriate filter strength, location of background phase measurements, and predictable phase artifacts around deep grey matter.

A different approach to background phase removal could improve tissue visualization by removing more phase wraps while preserving contrast within deep grey matter structures. There are several current options for phase removal but many require additional image processing such as segmentation and phase unwrapping, both of which can become unreliable areas of low SNR.

Although quantitative phase and relaxation MRI methods have been evaluated in phantoms, postmortem control subjects, and theoretical modelling, these methods remain unproven for analysis of iron in lesions and deep grey matter in MS. It is important to analyze the reliability of these methods in specific diseases as opposed to healthy controls as other processes could be occurring in the deep grey matter such as edema, demyelination, or neurodegeration, all of which could potentially affect these MRI measurements.

Longitudinal analysis of iron in deep grey matter in MS is lacking and is warranted to determine how iron changes over time. Currently there are only three longitudinal studies of deep grey matter iron in MS, each of which use qualitative FSE for iron determination without a control group [108][109][110]. Longitudinal quantitative measures may relate strongly to disease and may improve understanding of iron accumulation in MS.

It is ultimately desired to have an MRI method that correlates well to clinical scores, and accurately measures a biomarker of disease that represents specific underling tissue pathology. This could aid in diagnosis, prognosis, and could allow

further exploration of the pathobiology of the disease. Because of their sensitivity to a potential biological marker, and possible adaptability to clinical use, phase and relaxation MRI of deep grey matter in MS could fulfill this role. To bring this realization forward, several issues remain paramount: aspects of phase imaging must be investigated in relation to artifacts and measurement techniques in deep grey matter, new background phase removal techniques should be examined, methods must be tested for their correlation to iron in MS, and longitudinal analysis of iron accumulation in deep grey matter could provide a new method for evaluating disease. This thesis addresses these four issues and attempts to further the understanding of iron in MS as well as the use of phase and relaxation MRI for evaluating brain iron.

Bibliography

[1] Haacke EM. Magnetic resonance imaging : physical principles and sequence design. Wiley, New York, 1999.

[2] Bloembergen N, Purcell EM, Pound RV. Relaxation Effects in Nuclear Magnetic Resonance Absorption. Physical Review 1948;73(7):679–712.

[3] Tofts P. Quantitative MRI of the Brain Measuring Changes Caused by Disease Introduction. Quantitative Mri of the Brain: Measuring Changes Caused by Disease 2003;Xv–Xvi.

[4] Yablonskiy DA, Haacke EM. Theory of NMR signal behavior in magnetically inhomogeneous tissues: the static dephasing regime. Magnetic resonance in medicine 1994;32(6):749–63.

[5] Haacke EM, Mittal S, Wu Z, Neelavalli J, Cheng YC. Susceptibility-weighted imaging: technical aspects and clinical applications, part 1. AJNR Am J Neuroradiol 2009;30(1):19–30.

[6] Hagmann P, Jonasson L, Maeder P, Thiran JP, Wedeen VJ, Meuli R. Understanding diffusion MR imaging techniques: From scalar diffusion-weighted imaging to diffusion tensor imaging and beyond. Radiographics 2006;26:S205–U219.

[7] Grossman RI, Gomori JM, Ramer KN, Lexa FJ, Schnall MD. Magnetization-Transfer - Theory and Clinical-Applications in Neuroradiology. Radiographics 1994;14(2):279–290.

[8] Poloni G, Minagar A, Haacke EM, Zivadinov R. Recent Developments in Imaging of Multiple Sclerosis. Neurologist 2011;17(4):185–204.

[9] Gossuin Y, Muller RN, Gillis P. Relaxation induced by ferritin: a better understanding for an improved MRI iron quantification. NMR in biomedicine 2004;17(7):427–32.

[10] Jensen JH, Chandra R. Theory of nonexponential NMR signal decay in liver with iron overload or superparamagnetic iron oxide particles. Magnetic Resonance in Medicine 2002;47(6):1131–1138.

[11] Gillis P, Koenig SH. Transverse relaxation of solvent protons induced by magnetized spheres: application to ferritin, erythrocytes, and magnetite. Magnetic resonance in medicine 1987;5(4):323–45.

[12] Gossuin Y, Roch A, Muller RN, Gillis P, Lo Bue F. Anomalous nuclear magnetic relaxation of aqueous solutions of ferritin: an unprecedented first-order mechanism. Magnetic resonance in medicine 2002;48(6):959–64.

[13] Schenck JF. Magnetic resonance imaging of brain iron. Journal of the neurological sciences 2003;207(1-2):99–102.

[14] Haacke EM, Cheng NY, House MJ, Liu Q, Neelavalli J, Ogg RJ, Khan A, Ayaz M, Kirsch W, Obenaus A. Imaging iron stores in the brain using magnetic resonance imaging. Magnetic Resonance Imaging 2005;23(1):1–25.

[15] MacKay A, Laule C, Vavasour I, Bjarnason T, Kolind S, Madler B. Insights into brain microstructure from the T-2 distribution. Magnetic Resonance Imaging 2006;24(4):515–525.

[16] Vymazal J, Brooks RA, Zak O, Mcrill C, Shen C, Dichiro G. T1 and T2 of Ferritin at Different Field Strengths - Effect on Mri. Magnetic Resonance in Medicine 1992;27(2):368–374.

[17] Haacke EM, Reichenbach JR. Susceptibility weighted imaging in MRI : basic concepts and clinical applications. Wiley-Blackwell, Hoboken, N.J., 2011.

[18] Du YP, Chu R, Hwang D, Brown MS, Kleinschmidt-DeMasters BK, Singel D, Simon JH. Fast multislice mapping of the myelin water fraction using multicompartment analysis of T-2* decay at 3T: A preliminary postmortem study. Magnetic Resonance in Medicine 2007;58(5):865–870.

[19] Lee J, van Gelderen P, Kuo LW, Merkle H, Silva AC, Duyn JH. T-2*-based fiber orientation mapping. Neuroimage 2011;57(1):225–234.

[20] Mittal S, Wu Z, Neelavalli J, Haacke EM. Susceptibility-weighted imaging: technical aspects and clinical applications, part 2. AJNR Am J Neuroradiol 2009;30(2):232–52.

[21] De Zanche N, Maunder A, Charlton T, Wachowcz B KFallone. A Unified Framework for SNR Comparisons of Four Array Image Combination Methods. ISMRM, volume 19. Montreal, Canada, 2011; .

[22] Robinson RJ, Bhuta S. Susceptibility-weighted imaging of the brain: current utility and potential applications. Journal of neuroimaging 2011;21(4):e189–204.

[23] Wild JM, Martin WR, Allen PS. Multiple gradient echo sequence optimized for rapid, single-scan mapping of R(2)(*) at high B0. Magnetic resonance in medicine 2002;48(5):867–76.

[24] Cho ZH, Ro YM. Reduction of susceptibility artifact in gradient-echo imaging. Magnetic resonance in medicine 1992;23(1):193–200.

[25] Fernandez-Seara MA, Wehrli FW. Postprocessing technique to correct for background gradients in image-based R*(2) measurements. Magnetic resonance in medicine 2000;44(3):358–66.

[26] Du YPP, Jin ZY, Hu YZ, Tanabe J. Multi-Echo Acquisition of MR Angiography and Venography of the Brain at 3 Tesla. Journal of Magnetic Resonance Imaging 2009;30(2):449–454.

[27] Schweser F, Deistung A, Lehr BW, Reichenbach JR. Quantitative imaging of intrinsic magnetic tissue properties using MRI signal phase: An approach to in vivo brain iron metabolism? Neuroimage 2011;54(4):2789–2807.

[28] Liu T, Khalidov I, de Rochefort L, Spincemaille P, Liu J, Tsiouris AJ, Wang Y. A novel background field removal method for MRI using projection onto dipole fields (PDF). NMR in biomedicine 2011;24(9):1129–36.

[29] Rauscher A, Sedlacik J, Barth M, Mentzel HJ, Reichenbach JR. Magnetic susceptibility-weighted MR phase imaging of the human brain. AJNR American journal of neuroradiology 2005;26(4):736–42.

[30] Laule C, Vavasour IM, Moore GR, Oger J, Li DK, Paty DW, MacKay AL. Water content and myelin water fraction in multiple sclerosis. A T2 relaxation study. Journal of neurology 2004;251(3):284–93.

[31] Bartzokis G, Aravagiri M, Oldendorf WH, Mintz J, Marder SR. Field dependent transverse relaxation rate increase may be a specific measure of tissue iron stores. Magnetic resonance in medicine 1993;29(4):459–64.

[32] Jensen JH, Chandra R, Ramani A, Lu H, Johnson G, Lee SP, Kaczynski K, Helpern JA. Magnetic field correlation imaging. Magnetic resonance in medicine 2006;55(6):1350–61.

[33] Smith SA, Bulte JW, van Zijl PC. Direct saturation MRI: theory and application to imaging brain iron. Magnetic resonance in medicine 2009;62(2):384–93.

[34] Duyn JH. Study of brain anatomy with high-field MRI: recent progress. Magnetic resonance imaging 2010;28(8):1210–5.

[35] Kangarlu A. High-field magnetic resonance imaging. Neuroimaging clinics of North America 2009;19(1):113–28.

[36] Alonso A, Hernan MA. Temporal trends in the incidence of multiple sclerosis: a systematic review. Neurology 2008;71(2):129–35.

[37] Bach JF. The effect of infections on susceptibility to autoimmune and allergic diseases. The New England journal of medicine 2002;347(12):911–20.

[38] Compston A. McAlpine's multiple sclerosis. Churchill Livingstone Elsevier, 2005. ISBN 044307271X.

[39] Fischer JS, Rudick RA, Cutter GR, Reingold SC. The Multiple Sclerosis Functional Composite Measure (MSFC): an integrated approach to MS clinical outcome assessment. National MS Society Clinical Outcomes Assessment Task Force. Multiple sclerosis 1999;5(4):244–50.

[40] Roxburgh RH, Seaman SR, Masterman T, Hensiek AE, Sawcer SJ, Vukusic S, Achiti I, Confavreux C, Coustans M, le Page E, Edan G, McDonnell GV, Hawkins S, Trojano M, Liguori M, Cocco E, Marrosu MG, Tesser F, Leone MA, Weber A, Zipp F, Miterski B, Epplen JT, Oturai A, Sorensen PS, Celius EG, Lara NT, Montalban X, Villoslada P, Silva AM, Marta M, Leite I, Dubois B, Rubio J, Butzkueven H, Kilpatrick T, Mycko MP, Selmaj KW, Rio ME, Sa M, Salemi G, Savettieri G, Hillert J, Compston DA. Multiple Sclerosis Severity Score: using disability and disease duration to rate disease severity. Neurology 2005;64(7):1144–51.

[41] Polman CH, Reingold SC, Banwell B, Clanet M, Cohen JA, Filippi M, Fujihara K, Havrdova E, Hutchinson M, Kappos L, Lublin FD, Montalban X, O'Connor P, Sandberg-Wollheim M, Thompson AJ, Waubant E, Weinshenker B, Wolinsky JS. Diagnostic criteria for multiple sclerosis: 2010 revisions to the McDonald criteria. Annals of Neurology 2011;69(2):292–302.

[42] Lovblad KO, Anzalone N, Dorfler A, Essig M, Hurwitz B, Kappos L, Lee SK, Filippi M. MR imaging in multiple sclerosis: review and recommendations for current practice. AJNR American journal of neuroradiology 2010;31(6):983–9.

[43] Loma I, Heyman R. Multiple sclerosis: pathogenesis and treatment. Current neuropharmacology 2011;9(3):409–16.

[44] Wu GF, Alvarez E. The immunopathophysiology of multiple sclerosis. Neurologic clinics 2011;29(2):257–78.

[45] Barnett MH, Henderson AP, Prineas JW. The macrophage in MS: just a scavenger after all? Pathology and pathogenesis of the acute MS lesion. Multiple sclerosis 2006;12(2):121–32.

[46] van der Valk P, De Groot CJ. Staging of multiple sclerosis (MS) lesions: pathology of the time frame of MS. Neuropathology and applied neurobiology 2000;26(1):2–10.

[47] Stadelmann C, Wegner C, Bruck W. Inflammation, demyelination, and degeneration - recent insights from MS pathology. Biochimica et biophysica acta 2011;1812(2):275–82.

[48] Afifi AK. The basal ganglia: a neural network with more than motor function. Seminars in pediatric neurology 2003;10(1):3–10.

[49] DeLong M, Wichmann T. Update on models of basal ganglia function and dysfunction. Parkinsonism & related disorders 2009;15 Suppl 3:S237–40.

[50] Nolte J, Sundsten JW. The human brain : an introduction to its functional anatomy. Mosby, St. Louis, Mo., 5th edition, 2002.

[51] Carpenter MB. Core text of neuroanatomy. Williams & Wilkins, Baltimore, 4th edition, 1991.

[52] Hallgren B, Sourander P. The effect of age on the non-haemin iron in the human brain. Journal of neurochemistry 1958;3(1):41–51.

[53] Geurts JJ, Stys PK, Minagar A, Amor S, Zivadinov R. Gray matter pathology in (chronic) MS: modern views on an early observation. Journal of the neurological sciences 2009;282(1-2):12–20.

[54] Vercellino M, Masera S, Lorenzatti M, Condello C, Merola A, Mattioda A, Tribolo A, Capello E, Mancardi GL, Mutani R, Giordana MT, Cavalla P. Demyelination, inflammation, and neurodegeneration in multiple sclerosis deep gray matter. Journal of neuropathology and experimental neurology 2009; 68(5):489–502.

[55] Cifelli A, Arridge M, Jezzard P, Esiri MM, Palace J, Matthews PM. Thalamic neurodegeneration in multiple sclerosis. Annals of Neurology 2002;52(5):650–653.

[56] Derache N, Marie RM, Constans JM, Defer GL. Reduced thalamic and cerebellar rest metabolism in relapsing-remitting multiple sclerosis, a positron emission tomography study: correlations to lesion load. Journal of the neurological sciences 2006;245(1-2):103–9.

[57] Paulesu E, Perani D, Fazio F, Comi G, Pozzilli C, Martinelli V, Filippi M, Bettinardi V, Sirabian G, Passafiume D, Anzini A, Lenzi GL, Canal N, Fieschi C. Functional basis of memory impairment in multiple sclerosis: a[18F]FDG PET study. Neuroimage 1996;4(2):87–96.

[58] Roelcke U, Kappos L, Lechner-Scott J, Brunnschweiler H, Huber S, Ammann W, Plohmann A, Dellas S, Maguire RP, Missimer J, Radu EW, Steck A, Leenders KL. Reduced glucose metabolism in the frontal cortex and basal ganglia of multiple sclerosis patients with fatigue: a 18F-fluorodeoxyglucose positron emission tomography study. Neurology 1997;48(6):1566–71.

[59] Fernandez-Ruiz J, Lastres-Becker I, Cabranes A, Gonzalez S, Ramos JA. Endocannabinoids and basal ganglia functionality. Prostaglandins, leukotrienes, and essential fatty acids 2002;66(2-3):257–67.

[60] Pott F, Gingele S, Clarner T, Dang J, Baumgartner W, Beyer C, Kipp M. Cuprizone effect on myelination, astrogliosis and microglia attraction in the mouse basal ganglia. Brain Research 2009;1305:137–49.

[61] Geurts JJ, Barkhof F. Grey matter pathology in multiple sclerosis. Lancet neurology 2008;7(9):841–51.

[62] Mills E, Dong XP, Wang F, Xu H. Mechanisms of brain iron transport: insight into neurodegeneration and CNS disorders. Future medicinal chemistry 2010; 2(1):51–64.

[63] Marion D. Regulation of iron balance. In: UpToDate, Basow, DS (E). UpToDate, Waltham, MA, 2012;.

[64] Burdo JR, Connor JR. Brain iron uptake and homeostatic mechanisms: an overview. Biometals : an international journal on the role of metal ions in biology, biochemistry, and medicine 2003;16(1):63–75.

[65] Benarroch EE. Brain iron homeostasis and neurodegenerative disease. Neurology 2009;72(16):1436–40.

[66] Horowitz MP, Greenamyre JT. Mitochondrial iron metabolism and its role in neurodegeneration. Journal of Alzheimer's disease : JAD 2010;20 Suppl 2:S551–68.

[67] Williams R, Buchheit CL, Berman NE, LeVine SM. Pathogenic implications of iron accumulation in multiple sclerosis. Journal of neurochemistry 2012; 120(1):7–25.

[68] Ropele S, de Graaf W, Khalil M, Wattjes MP, Langkammer C, Rocca MA, Rovira A, Palace J, Barkhof F, Filippi M, Fazekas F. MRI assessment of iron deposition in multiple sclerosis. Journal of magnetic resonance imaging 2011; 34(1):13–21.

[69] Bagnato F, Hametner S, Yao B, van Gelderen P, Merkle H, Cantor FK, Lassmann H, Duyn JH. Tracking iron in multiple sclerosis: a combined imaging and histopathological study at 7 Tesla. Brain : a journal of neurology 2011; 134(Pt 12):3602–15.

[70] Adams CW. Perivascular iron deposition and other vascular damage in multiple sclerosis. Journal of neurology, neurosurgery, and psychiatry 1988; 51(2):260–5.

[71] Craelius W, Migdal MW, Luessenhop CP, Sugar A, Mihalakis I. Iron deposits surrounding multiple sclerosis plaques. Archives of pathology & laboratory medicine 1982;106(8):397–9.

[72] LeVine SM. Iron deposits in multiple sclerosis and Alzheimer's disease brains. Brain Research 1997;760(1-2):298–303.

[73] Wang J, Pantopoulos K. Regulation of cellular iron metabolism. The Biochemical journal 2011;434(3):365–81.

[74] Ong WY, Ren MQ, Makjanic J, Lim TM, Watt F. A nuclear microscopic study of elemental changes in the rat hippocampus after kainate-induced neuronal injury. Journal of neurochemistry 1999;72(4):1574–9.

[75] Hammond KE, Metcalf M, Carvajal L, Okuda DT, Srinivasan R, Vigneron D, Nelson SJ, Pelletier D. Quantitative In Vivo Magnetic Resonance Imaging of Multiple Sclerosis at 7 Tesla with Sensitivity to Iron. Annals of Neurology 2008;64(6):707–713.

[76] Lebel RM, Eissa A, Seres P, Blevins G, Wilman AH. Quantitative high-field imaging of sub-cortical gray matter in multiple sclerosis. Multiple sclerosis 2012;18(4):433–41.

[77] Brass SD, Benedict RHB, Weinstock-Guttman B, Munschauer F, Bakshi R. Cognitive impairment is associated with subcortical magnetic resonance imaging grey matter T2 hypointensity in multiple sclerosis. Multiple sclerosis 2006; 12(4):437–444.

[78] Khalil M, Langkammer C, Ropele S, Petrovic K, Wallner-Blazek M, Loitfelder M, Jehna M, Bachmaier G, Schmidt R, Enzinger C, Fuchs S, Fazekas F. Determinants of brain iron in multiple sclerosis: a quantitative 3T MRI study. Neurology 2011;77(18):1691–7.

[79] Ge Y, Jensen JH, Lu H, Helpern JA, Miles L, Inglese M, Babb JS, Herbert J, Grossman RI. Quantitative assessment of iron accumulation in the deep gray matter of multiple sclerosis by magnetic field correlation imaging. AJNR American journal of neuroradiology 2007;28(9):1639–44.

[80] Zhang Y, Zabad RK, Wei X, Metz LM, Hill MD, Mitchell JR. Deep grey matter "black T2" on 3 tesla magnetic resonance imaging correlates with disability in multiple sclerosis. Multiple sclerosis 2007;13(7):880–3.

[81] Ceccarelli A, Filippi M, Neema M, Arora A, Valsasina P, Rocca MA, Healy BC, Bakshi R. T2 hypointensity in the deep gray matter of patients with benign multiple sclerosis. Multiple sclerosis 2009;15(6):678–86.

[82] Bakshi R, Dmochowski J, Shaikh ZA, Jacobs L. Gray matter T2 hypointensity is related to plaques and atrophy in the brains of multiple sclerosis patients. Journal of the neurological sciences 2001;185(1):19–26.

[83] Ceccarelli A, Rocca MA, Neema M, Martinelli V, Arora A, Tauhid S, Ghezzi A, Comi G, Bakshi R, Filippi M. Deep gray matter T2 hypointensity is present in patients with clinically isolated syndromes suggestive of multiple sclerosis. Multiple sclerosis 2010;16(1):39–44.

[84] Tjoa CW, Benedict RH, Weinstock-Guttman B, Fabiano AJ, Bakshi R. MRI T2 hypointensity of the dentate nucleus is related to ambulatory impairment in multiple sclerosis. Journal of the neurological sciences 2005;234(1-2):17–24.

[85] Bakshi R, Benedict RH, Bermel RA, Caruthers SD, Puli SR, Tjoa CW, Fabiano AJ, Jacobs L. T2 hypointensity in the deep gray matter of patients with multiple sclerosis: a quantitative magnetic resonance imaging study. Archives of neurology 2002;59(1):62–8.

[86] Burgetova A, Seidl Z, Krasensky J, Horakova D, Vaneckova M. Multiple sclerosis and the accumulation of iron in the Basal Ganglia: quantitative assessment of brain iron using MRI t(2) relaxometry. European neurology 2010; 63(3):136–43.

[87] Ceccarelli A, Rocca MA, Perego E, Moiola L, Ghezzi A, Martinelli V, Comi G, Filippi M. Deep grey matter T2 hypo-intensity in patients with paediatric multiple sclerosis. Multiple sclerosis 2011;17(6):702–7.

[88] Holst B, Siemonsen S, Finsterbusch J, Bester M, Schippling S, Martin R, Fiehler J. T2' imaging indicates decreased tissue metabolism in frontal white matter of MS patients. Multiple sclerosis 2009;15(6):701–7.

[89] Habib CA, Liu M, Bawany N, Garbern J, Krumbein I, Mentzel HJ, Reichenbach J, Magnano C, Zivadinov R, Haacke EM. Assessing Abnormal Iron Content in the Deep Gray Matter of Patients with Multiple Sclerosis versus Healthy Controls. AJNR American journal of neuroradiology 2011;.

[90] Khalil M, Enzinger C, Langkammer C, Tscherner M, Wallner-Blazek M, Jehna M, Ropele S, Fuchs S, Fazekas F. Quantitative assessment of brain iron by R(2)* relaxometry in patients with clinically isolated syndrome and relapsing-remitting multiple sclerosis. Multiple sclerosis 2009;15(9):1048–54.

[91] Drayer B, Burger P, Hurwitz B, Dawson D, Cain J. Reduced signal intensity on MR images of thalamus and putamen in multiple sclerosis: increased iron content? AJR Am J Roentgenol 1987;149(2):357–63.

[92] Miki Y, Grossman RI, Udupa JK, Wei L, Polansky M, Mannon LJ, Kolson DL. Relapsing-remitting multiple sclerosis: longitudinal analysis of MR images–lack of correlation between changes in T2 lesion volume and clinical findings. Radiology 1999;213(2):395–9.

[93] van Waesberghe JH, van Walderveen MA, Castelijns JA, Scheltens P, Lycklama a Nijeholt GJ, Polman CH, Barkhof F. Patterns of lesion development in multiple sclerosis: longitudinal observations with T1-weighted spin-echo and magnetization transfer MR. AJNR American journal of neuroradiology 1998; 19(4):675–83.

[94] Fisher E, Rudick RA, Simon JH, Cutter G, Baier M, Lee JC, Miller D, Weinstock-Guttman B, Mass MK, Dougherty DS, Simonian NA. Eight-year follow-up study of brain atrophy in patients with MS. Neurology 2002; 59(9):1412–20.

[95] Evangelou N, DeLuca GC, Owens T, Esiri MM. Pathological study of spinal cord atrophy in multiple sclerosis suggests limited role of local lesions. Brain : a journal of neurology 2005;128(Pt 1):29–34.

[96] Filippi M, Agosta F. Imaging biomarkers in multiple sclerosis. Journal of magnetic resonance imaging 2010;31(4):770–88.

[97] Zivadinov R, Reder AT, Filippi M, Minagar A, Stuve O, Lassmann H, Racke MK, Dwyer MG, Frohman EM, Khan O. Mechanisms of action of disease-modifying agents and brain volume changes in multiple sclerosis. Neurology 2008;71(2):136–44.

[98] Schmierer K, Scaravilli F, Altmann DR, Barker GJ, Miller DH. Magnetization transfer ratio and myelin in postmortem multiple sclerosis brain. Annals of Neurology 2004;56(3):407–15.

[99] Filippi M, Campi A, Dousset V, Baratti C, Martinelli V, Canal N, Scotti G, Comi G. A magnetization transfer imaging study of normal-appearing white matter in multiple sclerosis. Neurology 1995;45(3 Pt 1):478–82.

[100] Audoin B, Ranjeva JP, Au Duong MV, Ibarrola D, Malikova I, Confort-Gouny S, Soulier E, Viout P, Ali-Cherif A, Pelletier J, Cozzone PJ. Voxel-based analysis of MTR images: a method to locate gray matter abnormalities in patients at the earliest stage of multiple sclerosis. Journal of magnetic resonance imaging 2004;20(5):765–71.

[101] Sun SW, Liang HF, Trinkaus K, Cross AH, Armstrong RC, Song SK. Noninvasive detection of cuprizone induced axonal damage and demyelination in the mouse corpus callosum. Magnetic resonance in medicine 2006;55(2):302–8.

[102] Benedict RH, Bruce J, Dwyer MG, Weinstock-Guttman B, Tjoa C, Tavazzi E, Munschauer FE, Zivadinov R. Diffusion-weighted imaging predicts cognitive impairment in multiple sclerosis. Multiple sclerosis 2007;13(6):722–30.

[103] Tartaglia MC, Arnold DL. The role of MRS and fMRI in multiple sclerosis. Advances in neurology 2006;98:185–202.

[104] Jensen JH, Szulc K, Hu CX, Ramani A, Lu HZ, Xuan L, Falangola MF, Chandra R, Knopp EA, Schenck J, Zimmerman EA, Helpern JA. Magnetic Field Correlation as a Measure of Iron-Generated Magnetic Field Inhomogeneities in the Brain. Magnetic Resonance in Medicine 2009;61(2):481–485.

[105] Pfefferbaum A, Adalsteinsson E, Rohlfing T, Sullivan EV. MRI estimates of brain iron concentration in normal aging: comparison of field-dependent (FDRI) and phase (SWI) methods. Neuroimage 2009;47(2):493–500.

[106] Langkammer C, Krebs N, Goessler W, Scheurer E, Ebner F, Yen K, Fazekas F, Ropele S. Quantitative MR imaging of brain iron: a postmortem validation study. Radiology 2010;257(2):455–62.

[107] Lebel RM, Wilman AH. Transverse relaxometry with stimulated echo compensation. Magnetic Resonance in Medicine 2010;64(4):1005–14.

[108] Neema M, Arora A, Healy BC, Guss ZD, Brass SD, Duan Y, Buckle GJ, Glanz BI, Stazzone L, Khoury SJ, Weiner HL, Guttmann CR, Bakshi R. Deep gray matter involvement on brain MRI scans is associated with clinical progression in multiple sclerosis. Journal of neuroimaging 2009;19(1):3–8.

[109] Zhang Y, Metz LM, Yong VW, Mitchell JR. 3T deep gray matter T2 hypointensity correlates with disability over time in stable relapsing-remitting multiple sclerosis: a 3-year pilot study. Journal of the neurological sciences 2010;297(1-2):76–81.

[110] Bermel RA, Puli SR, Rudick RA, Weinstock-Guttman B, Fisher E, Munschauer r F E, Bakshi R. Prediction of longitudinal brain atrophy in multiple sclerosis by gray matter magnetic resonance imaging T2 hypointensity. Arch Neurol 2005;62(9):1371–6.

Chapter 2

Susceptibility phase imaging with comparison to $R_2^\star$ mapping of iron-rich deep grey matter [1]

2.1 Abstract

Magnetic resonance imaging with susceptibility phase is seeing increasing use, especially at high magnetic fields. Tissue susceptibility can produce unique phase contrast for qualitative or quantitative imaging of iron-rich deep grey matter. However, phase imaging has several established sources of error including inherent susceptibility field effects and artifacts from background phase removal. These artifacts have led to inconsistent findings in past works relating iron to phase in healthy deep grey matter. This study seeks to determine the relative artifactual contributions from inherent susceptibility fields and from high pass phase filtering, currently the most common and accessible background phase removal method. In simulation, phase is compared to a known susceptibility distribution, while $R_2^\star$ maps are used as the in vivo gold standard surrogate for iron in healthy volunteers. The results indicate phase imaging depends highly on filtering, structure size, shape and local environment. Using in vivo phase and $R_2^\star$ profiles, it is shown that different filtering values, commonly seen in the literature, can lead to substantially different phase measures. Correlations between phase and $R_2^\star$ mapping are shown to be highly variable between structures. For example, using a standard filter of 0.125 the slopes and correlation coefficients were 4.28 x 10^{-4} ppm*s and R=0.88 for the putamen, 0.81 x 10^{-4} ppm*s and R=0.08 for the globus pallidus, 5.48 x 10^{-4} ppm*s and R=0.72 for the red nucleus, and 14.64 x 10^{-4} ppm*s and R=0.54 for the substantia

[1] A version of this section has been published. Walsh AJ, Wilman AH. Susceptibility phase imaging with comparison to $R_2^\star$ mapping of iron-rich deep grey matter. Neuroimage 2011,57:452-261.

nigra. To achieve the most effective correlation to $R_2^\star$ we recommend using a filter width of 0.094 for the globus pallidus and putamen and 0.125 for the substantia nigra and red nucleus. The baseline phase measure should be obtained directly adjacent to the substantia nigra, and red nucleus to yield the most accurate phase values as demonstrated in simulation and in vivo. Different regression slopes are seen between subROIs within structures suggesting that regional iron accumulation within a structure is best studied with subROIs between different subject groups, not differences in phase values relative to the overall phase in one structure. Phase imaging with the standard high pass filter method has the potential to differentiate subtle iron changes in pathological processes compared to normal tissues with more reliability if specific filter strengths and measurement areas are appropriately applied on a structure dependent basis.

2.2 Introduction

Phase susceptibility imaging and susceptibility-weighted imaging (SWI) have demonstrated sensitivity to brain iron [1, 2], which has been shown to accumulate in neurodegenerative diseases such as Alzheimer's disease [3], Parkinson's disease [4], and multiple sclerosis (MS) [5]. These imaging methods have been used for quantifying iron changes in deep grey matter [6, 2] and qualitatively for enhancing image contrast, particularly between MS lesions and normal tissue [7, 8, 9]. While transverse relaxation rate (R_2 or $R_2^\star$) mapping is sensitive to iron in normal individuals [10], phase imaging should be both more sensitive to iron because it depends on subtle phase shifts rather than significant dephasing, and more specific since phase is not significantly affected by water content, which could be a confound in cases of neurodegeneration [11].

Putative quantitative iron measures are seeing increasing use with phase imaging [12, 9, 13, 14], however, studies have not shown consistent reliability of phase imaging for iron measurement because phase is also confounded by certain physical factors including: the angle of brain structure to the Bo field [15], neuronal fiber orientation [16], myelin content [17], calcium and phospholipid content [18], neighboring susceptibility sources [19], and the type of background phase removal method [1, 20, 19, 21]. By focusing on the iron-rich basal ganglia, where there are substantial deposits of non-heme iron, factors such as phospholipids, myelin and fiber orientation will contribute a smaller role bringing background phase removal and susceptibility field effects to the forefront.

Background phase removal is necessary to remove the global magnetic field variations created by the geometry of the head and air tissue interfaces, such as the nasal cavity, in order to provide access to the underlying field variations related

to the local tissue environment. While new phase background removal methods are continually evolving, standard phase imaging with simple background phase removal through phase filtering has been used extensively throughout the short history of phase imaging [22, 13, 23] and in recent neurological studies [24, 25, 26, 27, 28]. As well, the phase filtering approach has the advantage of being relatively easy to implement and is widely available on many clinical MRI systems. Although this method produces visually interpretable images, it can alter the true phase values in certain brain structures. The effect of filtering on phase images has implications in quantitative phase measurements because effects of filtering depend upon object shape and size. This requires an in-depth understanding of shape effects.

The effect of phase suppression from varying filter strength has been previously presented qualitatively [12], and quantitatively [22, 29] which has led to one common standard filtering approach of utilizing 12% of the image in a low pass filter, in order to suppress background global fields but attempt to retain local phase differences. The quantitative studies either did not examine deep grey matter or did not compare subsections of the structures between filter strengths. Since deep grey matter structures vary in shape and size, different parts of structures could be affected differently by filtering and this could have implications when examining iron accumulation patterns.

As well as phase filtering, susceptibility field effects also substantially affect phase images [30, 31, 15]. These dipolar field effects result from the susceptibility difference, $\Delta\chi$, between the inner and external environment of a structure and phase effects are produced within and around structures. Considering a very simple spherical susceptibility distribution, the analytical solution for field effect changes is well known depending on $\Delta\chi$ inside of the spherical structure, and outside on $\Delta\chi$ and on the directional component $3cos^2(\theta) - 1$, where θ is the angle to the main magnetic field. More geometrically complex susceptibility distributions require a numerical computation by multiplication of a dipole field in k-space [15], which has demonstrated the directional, and nonlocal, field effects of more anatomically representative distributions.

In the human brain, $R_2^\star$ values have shown very high correlation to post mortem iron concentrations r = 0.9 [32]. However, previous studies have correlated phase or $R_2^\star$ to predicted iron content of the basal ganglia with minimal success [33, 19, 21]. These studies compared phase between different structures in the same individual, while examining the same structure across individuals would enable phase-iron correlation without the confounding effects of structure dependent filtering and field shift due to structure shape.

In this work, phase imaging is compared to quantitative $R_2^\star$ mapping across multiple volunteers to demonstrate the role of susceptibility fields, phase filtering

and ROI placement in each iron-rich, deep grey matter structure. Phase variations are examined in simulation and in vivo experiments using a wide range of filters with clear separation of susceptibility field effects from filter reconstruction effects. Structure-dependent recommendations for filter size and ROI placement are provided. By quantifying the possible confounds of phase imaging in deep grey matter, a means for better interpretation of quantitative phase imaging is provided.

2.3 Materials and Methods

Phase imaging was studied in three ways. First, a computer simulation tested the effects of phase filtering using a simple susceptibility model that accounted for inherent susceptibility fields. Second, in vivo phase susceptibility experiments were performed at 3.0 T on healthy subjects to validate simulation findings. Third, the in vivo phase susceptibility within each deep grey matter structure was measured using different filters and ROI placements, and correlated to corresponding $R_2^\star$ measurements.

2.3.1 Susceptibility Field Modeling

A simplified 3D susceptibility distribution of the basal ganglia was created in Matlab (MathWorks Inc., Massachusetts, USA) using only the putamen (PUT), globus pallidus (GP), substantia nigra (SN), and red nucleus (RN). The model boundaries were traced from a healthy control subject using multiple axial slices (3 mm thick, TE 40 ms, gradient echo). Voxels inside each region received homogeneous susceptibility values (PUT = 0.09 ppm, GP = 0.18 ppm, SN = 0.16 ppm, RN = 0.13 ppm) based on values calculated by Wharton and Bowtell (2010) [19]. Voxels outside these regions were set to zero. These slices were interpolated to create a 3D volume with 0.5mm isotropic pixel dimension. This 3D susceptibility distribution was Fourier transformed into k-space and multiplied by the corresponding dipole field using a field forward calculation as described in Marques and Bowtell (2005) [34] and Salomir et al. (2003) [35]. The resulting k-space volume was then inverse Fourier transformed to produce a field map in image space. Three planes in the z direction were then averaged to produce 1.5 mm thick slices for 2D filtering.

2.3.2 Filter

The phase image resulting from the field effects of the model was subject to 2D spatial high pass filtering with increasing strength of filters. The standard filtering method of Haacke was used[8, 23]. A 2D symmetrical Hanning window was constructed in k-space, size m x m points, and zero padded to the full n x n matrix

size, of the original 2D image. The filter width was defined as the ratio of one dimension of the Hanning window divided by the total filter size in that dimension: m/n, using a square field of view and isotropic resolution. A typical filter reported is 0.125 filter width or greater[29, 23]. Filtering effects were examined using a range of filter widths from 0 to 0.2. The raw k-space data matrix was multiplied by this 2D Hanning window, and the result was Fourier transformed to the spatial domain, resulting in a low pass filtered image. This low pass image was complex divided into the original image to produce a high pass filtered image from which phase angles were calculated.

2.3.3 Phase Behavior in Simulation

The simulated 2D images of the GP-PUT and SN-RN slices were examined with 4 different filter widths (0.063, 0.094, 0.125, and 0.200) and compared to images of the raw phase and the susceptibility distribution. The effects arising from filtering and from field shifts were studied. Next, the field effect created by neighboring susceptibility distributions was examined more closely by assigning a constant susceptibility to the GP (0.16 ppm) with four different susceptibility values assigned to the PUT (0.06, 0.09, 0.12, 0.15 ppm). These four separate simulations were filtered with the standard 0.125 filter width to illustrate the internal phase effects in a brain structure from external susceptibility sources within neighboring tissue, while using a constant filter. Conversely, the internal phase within the SN due to inherent susceptibility was studied by assigning susceptibility values to the SN (0.18, 0.16, 0.14 ppm). The effect of external field shifts caused by the different susceptibility values assigned to the PUT within the GP were studied by comparing the cross sectional profiles though both structures. The phase within the SN due to different susceptibility values from within the structure was studied by comparing the measured phase to the assigned susceptibility from ROIs which encompass the entire 2D structure in one axial image. To quantify the phase effect due to structure shape and filter strength, measures from a cross sectional profile of the deep grey matter structures were obtained in simulation. To compare simulation to in vivo measures, fractional measures were used to remove the effects of varying structure susceptibility across subjects. Phase changes were evaluated by comparing the edge phase to middle phase values between filters, and the change in edge phase between filters. To evaluate the phase changes across a structure with different filter widths, the measures between phase at the edge minus the middle divided by the edge minus the baseline produced a fractional phase change from the edge to middle of the structure. The baseline was measured adjacent to the outside edge of the structure. For normalization, the divisor (const) was based on the measured phase from the smallest filter width profile and the edge to middle phase was compared between

four filter widths (0.200, 0.125, 0.094 0.063).

$$\text{Phase change middle}_i = \frac{\text{edge}_\text{i} - \text{middle}_\text{i}}{\text{edge}_\text{const} - \text{base}_\text{const}} \tag{2.1}$$

Also of interest are the changes in edge phase with the four different filter widths between the simulated structures. The phase measured at the edge subtracted from the baseline phase of a structure with one of the four filter widths was subtracted from the edge phase subtracted from the baseline phase using the smallest filter width. The result was divided by the phase measured at the edge subtracted by the phase measured at the base immediately outside of the structure with the smallest filter width.

$$\text{Phase change edge}_i = \frac{(\text{edge}_\text{i} - \text{base}_\text{i}) - (\text{edge}_\text{const} - \text{base}_\text{const})}{\text{edge}_\text{const} - \text{base}_\text{const}} \tag{2.2}$$

In Eqs. 2.1 and 2.2, the constant, or smallest filter width, for edge and base is 0.094 for the RN and SN and 0.063 for the GP and PUT. The 0.063 filter width was not used to evaluate the SN and RN because of visible phase wrapping within these structures in vivo when this small filter width was applied.

2.3.4 Volunteer MRI Acquisition

Images were obtained from seven healthy volunteers (age 36 ± 16 years) to quantify the effects of filter width on the phase measured within deep grey matter structures and to correlate $R_2^\star$ to phase. Using a 3.0 T MRI system, a 2D gradient echo sequence (flip angle 60°, TR 500 ms, 512 frequency x 256 phase, 3 mm thickness, 7 slices, no slice separation, FOV 25 cm) was used to image the basal ganglia. The images were zero padded in k-space to 512 x 512 resolution before phase filtering. Four separate echo times were used TE 9/16/26/40 ms [36] with 40 ms being the maximum because images acquired with a greater TE incurred artifact from field inhomogeneities due to the nasal cavity and paranasal sinuses. $R_2^\star$ maps of the brain were obtained by fitting the four echoes with a single exponential decay. $R_2^\star$ values from structures in the basal ganglia were compared to the phase values computed from the TE = 16 ms and 26 ms images since typically phase images are acquired at TE of 16 - 26 ms at 3.0 T [37, 38]. Four filter widths were applied to each image: 0.200, 0.125, 0.094, and 0.063, corresponding to a central filter width of 102 x 102, 64 x 64, 48 x 48, and 32 x 32. These phase values were converted to ppm by dividing by $\gamma \cdot B_0 \cdot TE \cdot 10^{-6}$ [39] .

2.3.5 Volunteer Phase Profile Comparison

In each subject, cross sectional profiles were taken through each basal ganglia structure. The percentage decrease in phase from edge-to-middle and edge-to-base was computed and averaged across all subjects, yielding 14 measurements from each structure using Eqs. 2.1 and 2.2. This was repeated for each of the four filters. To evaluate if the $R_2^\star$ profile of each structure was indeed flat, the $R_2^\star$ values were measured at the edge and middle of a structure and compared with a paired t-test.

2.3.6 Volunteer Phase vs $R_2^\star$ Mapping

Regressions between phase and $R_2^\star$ in different structures were examined with different filter widths and different ROIs. The differences in regression slope between different filter widths are used to examine the effect of filtering on measured phase. For a specific structure, a changing regression slope indicates that structures with higher raw phase are affected more severely by filtering. Correlations between phase and $R_2^\star$ are used to determine the accuracy of phase measures with different filters, ROIs within structures, and baseline ROI measures. Phase and $R_2^\star$ were calculated in basal ganglia structures by averaging voxels within ROIs. ROIs were constructed, based on the $R_2^\star$ map, around whole structures and around selective parts of structures. The same registered ROI was used for $R_2^\star$ and phase measurement. To avoid partial volume effects in the superiorinferior direction, the ROIs were obtained from an $R_2^\star$ image slice where the structure was visible in slices both above and below. The selective ROIs were around the lateral PUT, the medial GP, posterior PUT, posterior lateral PUT, posterior GP, posterior lateral GP and the posterior RN. Selective ROIs were not measured from the SN because of its small shape. The structural phase measures are compared to two baseline phase measures, one from an area of subcortical white matter (WM) and another from an area directly adjacent to the structure of interest.

2.4 Results

2.4.1 Phase Behavior in Simulation

Figs. 2.1 and 2.2 depict the effects on the susceptibility distribution using the 3D field forward model with various phase filter widths. In both figures, the central phase values within a structure decrease as the filter width increases, with only the extreme edges retaining close to unfiltered values. The susceptibility distribution in Figs. 2.1a and 2.2a differs substantially from the unfiltered phase image in Figs. 2.1b and 2.2b, which is calculated from the field forward model. In particular, the phase image illustrates field effects from structures outside of the slice due to nonlocal

effects of the field distribution. For example, in Fig. 2.1b phase effects from the RN are evident even though the RN is not within the slice. This out-of-plane field shift can offset the baseline phase of the basal ganglia structures, as demonstrated in the profiles shown in Fig. 2.3. Because the overall baseline in this region is offset negatively, a decrease in filter size does not necessarily increase the measured phase within a structure (Fig. 2.3b and d). However, the phase within a structure compared to a baseline immediately outside of the structure is increased.

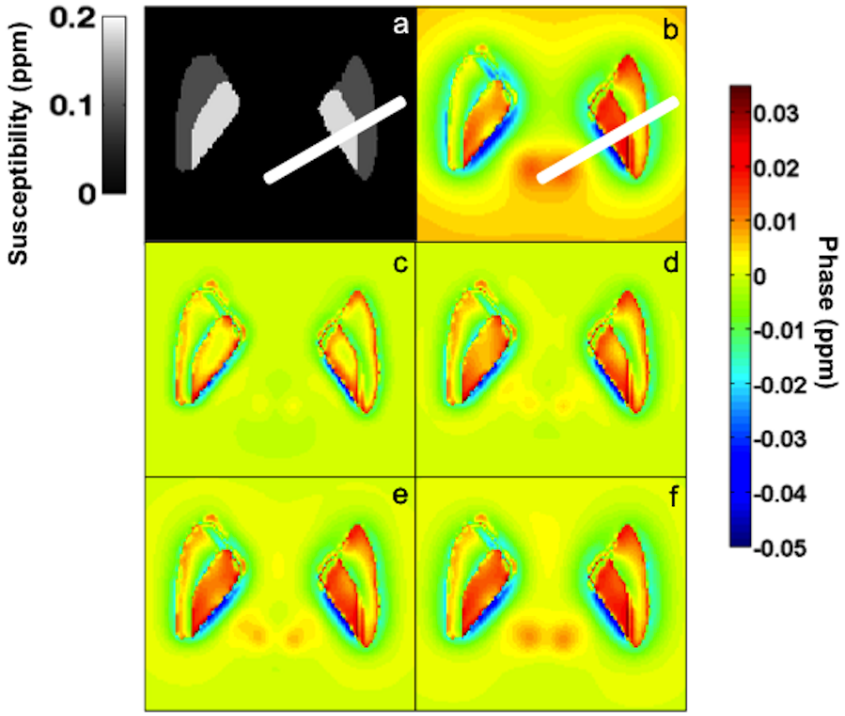

Figure 2.1: 3D field forward model of the PUT and GP with (a) susceptibility distribution before k-space dipole multiplication, (b) unfiltered 3D field forward model, and (c-f) 3D field forward phase model with 4 different filter widths: (c) 0.200, (d) 0.125, (e) 0.094, and (f) 0.063. Units are ppm for phase and ppm for susceptibility. Also cross sectional profiles for Fig. 2.3 are shown through the GP and PUT in (a) and (b).

The unfiltered profiles show that the baseline phase is different from zero because of the nonlocal susceptibility effect of other structures (Fig. 2.3b and d). This nonzero baseline was manually adjusted by moving the profile along the phase axis until the edges of the raw phase matched the outer edges of the least filtered phase. This allows visual comparison of the difference between the raw profile and the filtered profiles. From Fig. 2.3b, it appears that phase is most affected by filtering in the middle of the GP because of its large in plane dimension, which leads to a narrower k-space representation that is more strongly affected by the low pass filter. The profile through the PUT seems relatively unaffected by filtering, especially on

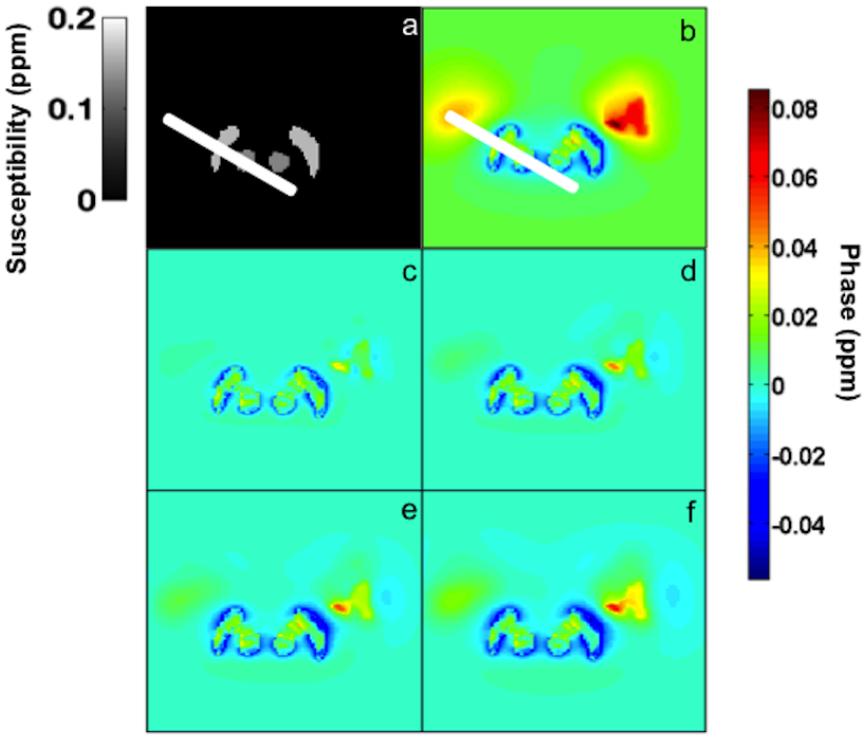

Figure 2.2: 3D field forward model of the SN and RN with (a) susceptibility distribution before k-space dipole multiplication, (b) unfiltered 3D field forward model of the SN and RN, and (c-f) field forward phase model with 4 different filter widths: (c) 0.200, (d) 0.125, (e) 0.094, and (f) 0.063. Units are ppm for field shift and ppm for susceptibility. Also cross sectional profiles for Fig. 2.3 are shown through the SN and RN in (a) and (b).

the lateral border. The profile through the SN and RN shows that the phase within the structure does not vary appreciably with filtering however the phase between the two structures seems to be elevated compared to the susceptibility distribution.

The external field shift effect generated by susceptibility distributions is modeled in Fig. 2.4, where profiles are shown through the PUT and GP with a susceptibility profile, raw phase profile and filtered phase profile using a 0.125 filter width. Different susceptibility values within the PUT have field shift effects external to its structure and consequently affect the phase profile of the adjacent GP, even though the susceptibility value of the GP remains the same. It appears that the PUT and GP have field effects external to their structure boundaries resulting in phase effects in the neighboring part of the other structure.

The internal field shift effect due to different assigned susceptibilities in the SN shows that the phase values decrease as the susceptibility increases. The assigned

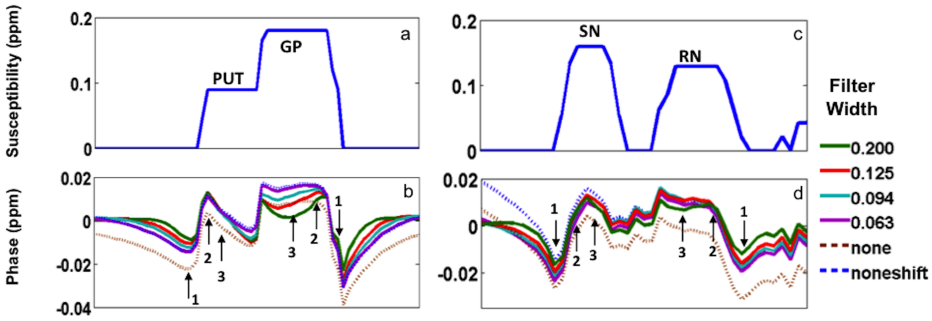

Figure 2.3: Susceptibility and phase profiles of the GP, PUT, SN, and RN from the cross sections shown in Figs. 2.1 and 2.2. Cross sectional susceptibility profile (in ppm) of (a) GP and PUT and (c) SN and RN. Phase profile of (b) GP and PUT and (d) SN and RN. Phase profiles used 4 different filter widths in solid lines (0.200, 0.125, 0.094, and 0.063), and show the raw phase profile and the phase axis shifted phase profile (dotted lines). The raw phase is aligned along the phase axis so the structure borders have the same phase value. Arrows in (b) and (d) show the measurement locations for Eqs. (1) and (2), with arrow 1: base, arrow 2: edge, and arrow 3: middle.

susceptibility values of 0.18, 0.16, and 0.14 ppm produced the measured phase values of 0.0107, 0.0133, and 0.0159 ppm (phase) respectively using ROIs around the entire structure. As susceptibility increases in the SN, the phase evolution decreases. This is opposite to what was observed with the increasing susceptibilities in the PUT (Fig. 2.4). Furthermore, there is an apparent shift in structural borders between the phase and susceptibility profile that is perhaps most pronounced in the SN cross section (Fig. 2.3c and d) due to the field shift.

2.4.2 Volunteer Phase Profile Comparison

In Fig. 2.5, in vivo phase and $R_2^\star$ profiles are shown through the GP-PUT and SN-RN for one volunteer. Fortuitously, the raw phase profile shown for the GP-PUT is

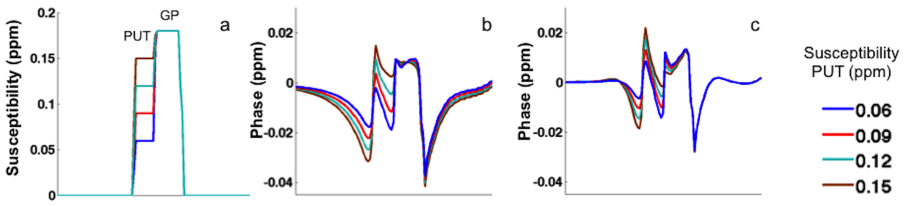

Figure 2.4: Cross sectional field shift values of the GP and PUT with different susceptibility values assigned to the PUT. (a) Susceptibility distribution (b) raw field map (c) filtered field map. Filter width 0.125.

in line with the global susceptibility change created by the nasal cavity and sinuses, enabling visualization of the unfiltered phase without significant contamination. The profile of the PUT $R_2^\star$ map has a relatively flat shape while the phase does not, because of susceptibility effects from the GP. The raw phase of the PUT is not flat in the profile of the GP and PUT in Fig. 2.5b, and worsens with increasing filtering, similar to the raw phase of the simulation in Fig. 2.3b. Tables 2.1 and 2.2 compare phase values from in vivo measurements and the simulation using a range of filtering widths. Two measurement locations are used: the difference between edge and central phase value within a structure between filters (Table 2.1, Eq. 2.1), and the difference between the edge and base between filters (Table 2.2, Eq. 2.2). In Table 2.1, the edge-to-middle phase values show that with increasing filter strength, the phase in the middle of a structure decreases in all structures. The predicted decrease in phase from the edge of a structure to the middle has a similar trend in simulation and experiment for the GP and PUT, but not for the SN and RN. Interestingly, the phase in the PUT is less affected by filtering until the filter width is decreased to 0.063 because the inclined raw phase profile of the PUT has higher spatially varying frequencies than a flat shape. In Table 2.2, the predicted decrease in phase at the edge of a structure follows the same trend as seen in vivo for all the structures. As the filter width decreases, the phase at the edge of the structure compared to outside of the structure increases.

Table 2.1: Fractional phase difference of deep grey structures from edge to middle compared to adjacent baseline - in vivo and simulation.

Structure	Filter width	In vivo phase edge to middle (ppm ± stdev)	Simulated phase edge to middle (ppm)
PUT	0.2	0.22 ± 0.06	0.30
	0.125	0.19 ± 0.09	0.32
	0.094	0.19 ± 0.10	0.28
	0.063	0.13 ± 0.10	0.24
GP	0.2	0.20 ± 0.08	0.23
	0.125	0.10 ± 0.08	0.11
	0.094	-0.01 ± 0.12	0.04
	0.063	-0.08 ± 0.16	-0.03
SN	0.2	-0.05 ± 0.14	-0.06
	0.125	-0.17 ± 0.18	-0.11
	0.094	-0.25 ± 0.20	-0.14
RN	0.2	0.18 ± 0.14	-0.01
	0.125	0.06 ± 0.14	-0.05
	0.094	0.06 ± 0.14	-0.08

In contrast to phase, $R_2^\star$ values across each structure showed much less variability. The paired t-test for $R_2^\star$ values corresponding to the spatial location of phase

Table 2.2: Fractional phase difference of deep grey structure edges - in vivo and simulation

Structure	Filter width	In vivo phase edge difference compared to smallest filter (ppm ± stdev)	Simulated phase edge differences (ppm)
PUT	0.2	-0.35 ± 0.06	-0.29
	0.125	-0.15 ± 0.04	-0.13
	0.094	-0.07 ± 0.03	-0.10
	0.063	0.00 ± 0.00	0.00
GP	0.2	-0.44 ± 0.13	-0.30
	0.125	-0.19 ± 0.09	-0.13
	0.094	-0.05 ± 0.08	-0.06
	0.063	0.00 ± 0.00	0.00
SN	0.2	-0.42 ± 0.10	-0.15
	0.125	-0.15 ± 0.04	-0.04
	0.094	0.00 ± 0.00	0.00
RN	0.2	-0.31 ± 0.12	-0.24
	0.125	-0.08 ± 0.05	-0.04
	0.094	0.00 ± 0.00	0.00

measures indicated that the $R_2^\star$ values are the same at the edge and middle of structures in the PUT, SN, and RN, while the $R_2^\star$ is significantly higher ($p<0.05$) in the middle of the GP compared to the edge.

2.4.3 Volunteer Phase vs $R_2^\star$ mapping

The location of the phase and $R_2^\star$ measures obtained for regression analysis with PUT, GP, SN, and RN, are shown in Fig. 2.6 while the scatter plots of $R_2^\star$ vs phase measures are presented in Figs. 2.7 and 2.8. The equations for the linear regression lines, correlation coefficients, and p values of the slope are found in Tables 2.3, 2.4, 2.5. The phase values are highly variable depending upon filter and structure, as discussed below.

In the PUT, the correlation between phase and $R_2^\star$ is generally high and is improved with ROI placement and filter width adjustment. The ROI structural measurements reveal that whole structure measurements show a weaker correlation ($R = 0.71$) compared to measuring the posterior part of the structure ($R=0.90$) with the smallest filter width of 0.063. Also of note, the slope of the regression line is less variable when the phase is measured at the lateral border (4.20 - 4.55 x 10^{-4} ppm*s) of the structure compared to around its entirety (3.12 - 5.10 x 10^{-4} ppm*s) (Fig. 2.7a-d and Table 2.3). As well, the correlation between phase and $R_2^\star$ is similar when baseline phase measures are obtained from a nearby section of

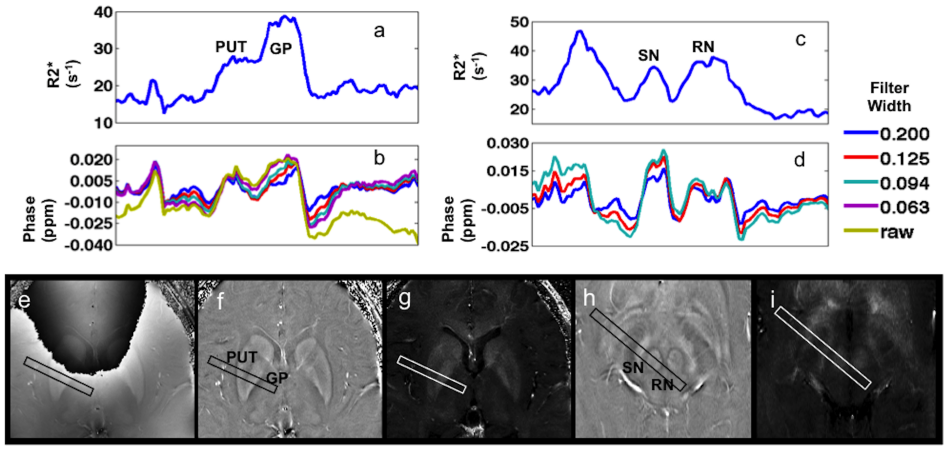

Figure 2.5: In vivo cross sectional profiles of (a) $R_2^\star$ and (b) phase with different size filter widths across the PUT and GP. The raw phase in (b) is adjusted along the phase axis to align the phase of the outside of both structures since the raw phase is arbitrary. Cross sectional profiles of (c) $R_2^\star$ and (d) phase with different filter widths across the SN and RN. Axial images of (e) raw phase and (f) filtered phase, with a filter width of 0.125 for the GP and PUT, TE = 16 ms. (g) Axial $R_2^\star$ map of the GP and PUT. (h) Filtered phase with a filter width of 0.125 showing the SN and RN, TE = 16 ms. (i) $R_2^\star$ map of the SN and RN. The rectangular section has a width of 12 pixels in e-g and 8 pixels in h-i. The pixels along the width of the rectangular section are averaged to produce the graphs in a-d to mitigate the effects of noisy pixels and create a smoother profile for more accurate phase measurements.

subcortical WM or when taken immediately outside of the structure.

In the GP, although the size, shape, and orientation is similar to that of the PUT, the regression analysis between phase and $R_2^\star$ are markedly different. The regression between phase and $R_2^\star$ in the GP across subjects is only significant when measured at the edge of the structure and even then only has a moderate correlation of R = 0.52 using a filter width of 0.094 (Fig. 2.7e,f and Table 2.4). As opposed to the PUT measurements, the correlation coefficient is not significant when the baseline phase is measured immediately outside of the GP.

The SN regression between phase and $R_2^\star$ is negative (Fig. 2.8a,b and Table 2.5), which agrees with the simulated results. The correlation between phase and $R_2^\star$ appears higher when phase is compared to a baseline adjacent to the SN (R = 0.67) versus the subcortical WM baseline (R=0.54) using a filter width of 0.125. In the SN, there was visible artifact when the filter width was set to 0.063.

In the RN, as seen with the regression analysis of the SN, there appears to be a higher correlation between phase and $R_2^\star$ in the RN with the baseline phase measure obtained adjacent to the structure (R = 0.81) compared to subcortical WM (R = 0.72) using a filter width of 0.125 (Figs. 2.8c-f and Table 2.5). There is less variation

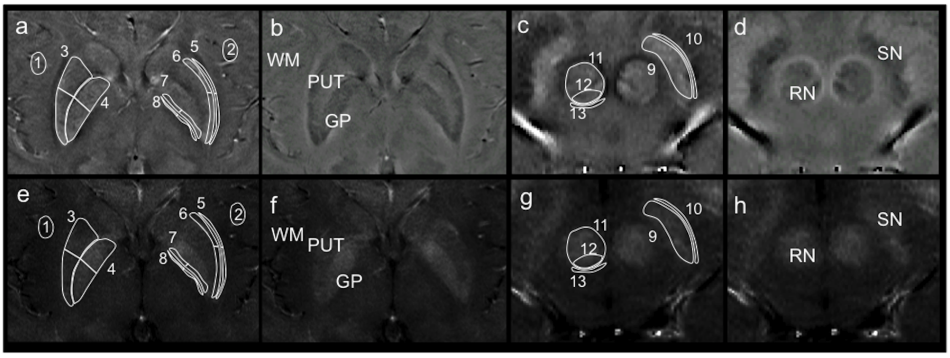

Figure 2.6: Phase images (top row) and $R_2^\star$ images (bottom row) illustrating ROI placement. The top row illustrates inverted phase images (a and c) as used for comparison to $R_2^\star$ values, and traditional phase images of the same slice (b and d), with stronger susceptibility sources having a more negative value. The bottom row of $R_2^\star$ images show larger $R_2^\star$ values as being brighter. The ROIs are identified by numbers on the two slice locations (a, b, d, f) GP, PUT and (c, d, g, h) RN, SN. (1) and (2) are sections of subcortical WM. (3) the entire PUT and posterior PUT, (4) the entire GP and posterior GP, (5) the lateral and lateral posterior baseline adjacent to the PUT, (6) the lateral and lateral posterior aspect of PUT, (7) the medial and medial posterior aspect of GP, (8) the medial and medial posterior baseline adjacent to the GP, (9) the entire SN, (10) the adjacent baseline of SN, (11) the entire RN, (12) the posterior aspect of RN, and (13) the adjacent baseline of the RN. Sections of subcortical white matter are not shown for the RN SN but are in similar position to (1) and (2) but in the axial slice of the RN SN.

in the slope of the regression when the structural ROI is taken at the posterior aspect of the structure (4.19 - 6.85 x 10^{-4} ppm*s) compared to an ROI around the whole structure (3.22 - 6.59 x 10^{-4} ppm*s), not including the 0.063 filter width because wrapping artifact was apparent within the structure.

2.5 Discussion

The main factors examined in this study that contribute to phase values produced by a susceptibility distribution are structural geometry, filtering, and external field shift effects from other susceptibility sources. Our work has shown that more accurate phase measurements can be obtained with careful attention to where the baseline phase comparison is obtained, what subsections of the structure are measured, and appropriate choice of filter width for the size and location of a structure. While new background phase removal methods and susceptibility mapping techniques are evolving, the simplicity and availability of standard phase imaging explain the current widespread use and support the future consideration of the method in iron accumulation studies.

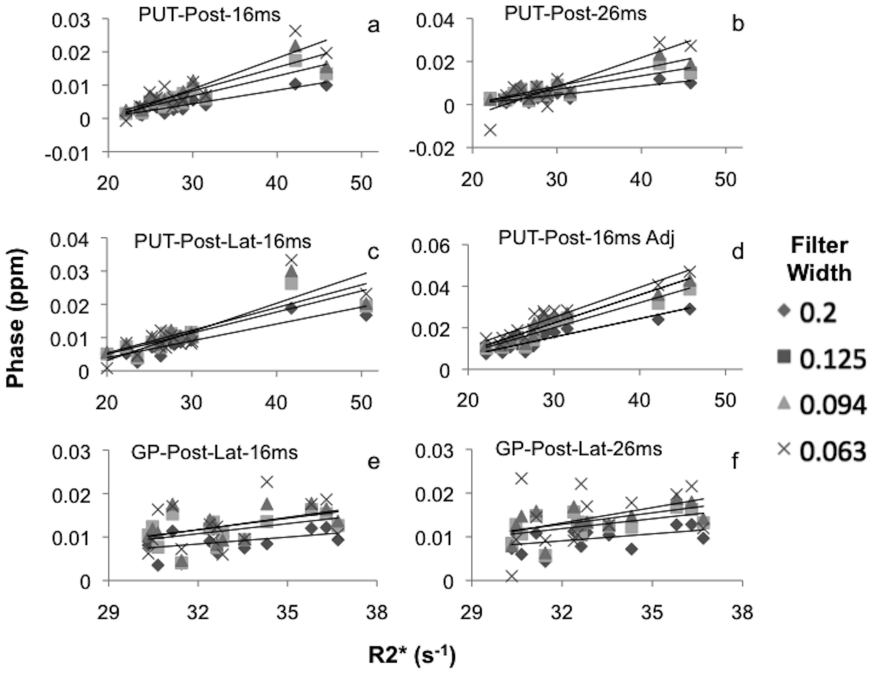

Figure 2.7: Phase vs $R_2^\star$ linear regression of the GP and PUT from 7 healthy volunteers, with each scatter plot showing 4 different filters: 0.200, 0.125, 0.094, and 0.063. (a, b) Posterior half of the PUT (a) 16 ms TE (b) 26 ms TE, (c) posterior lateral aspect of the PUT 16 ms TE. Field shift measures in a-c are compared to a section of subcortical WM (Fig. 6). (d) Posterior aspect of the PUT compared to measure adjacent to PUT 16 ms TE. (e, f) Posterior lateral aspect of the GP compared to a section of subcortical WM with (e) 16 ms TE, and (f) 26 ms TE.

The susceptibility distribution of a deep grey matter structure can cause field effect changes within and around that structure, potentially having an adverse effect on measured phase. This is demonstrated both in simulation and in vivo phase images. The in vivo cross sectional profile through the GP and PUT shows that the phase profile in the PUT is slanted towards the GP while the $R_2^\star$ profile is flat. As shown in the simulation profiles, the lateral aspect of the PUT, the medial aspect of the GP and the posterior aspect of the RN are less affected by surrounding susceptibility distributions in both unfiltered and filtered phase images. Therefore, phase should not be measured from areas that are highly influenced by external field effects such as the medial PUT or the lateral GP.

While a susceptibility distribution can cause external field shift effects, the internal phase depends not only on the susceptibility, but also on the shape of the structure. The in vivo profile (Fig. 2.3) and axial phase image (Figs. 2.1 and 2.2) demonstrate that the phase within a structure depends on the shape, which is perhaps most pronounced in the SN. In the simulation and in vivo profile, the

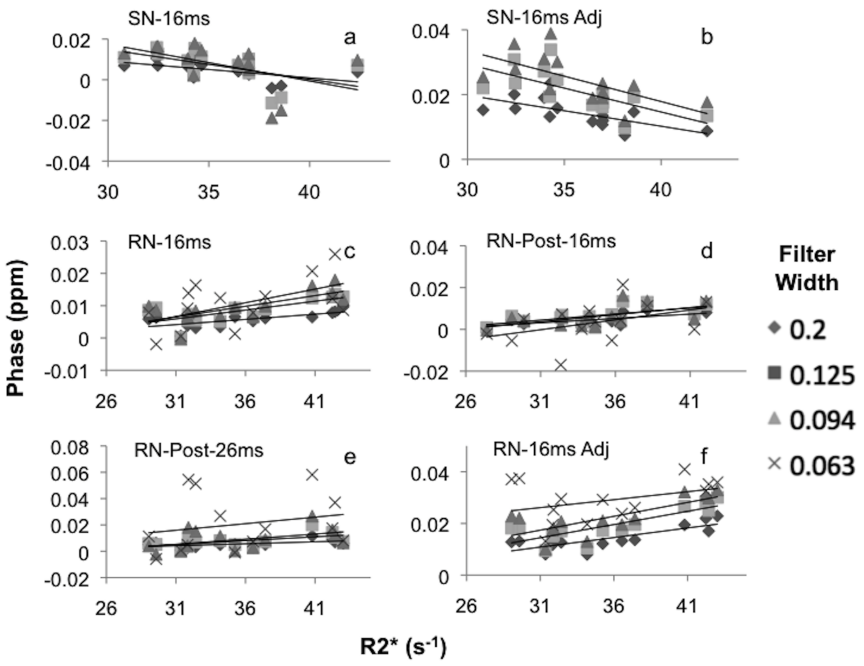

Figure 2.8: Phase vs $R_2^\star$ regression of the SN and RN. (a, b) Whole SN 16 ms TE with phase compared to section of subcortical WM in (a) and adjacent to SN in (b). (c) Whole RN 16 ms TE (d) posterior aspect of RN 16 ms TE, (e) whole RN 26 ms TE. Measured phase in c-e is compared to a section of subcortical WM (Fig. 6). (f) Whole RN 16 ms TE compared to phase directly posterior to structure. Each scatter plot shows 4 different filters: 0.200, 0.125, 0.094, and 0.063.

lateral borders of the SN show less phase evolution making it difficult to discern the structure's true edge. This effect makes it appear as though the edge is shifted in the phase image compared to the $R_2^\star$ map, which has been described for other structures in phase imaging [40]. Since the edge shift appears in both in vivo and simulated, non-filtered phase images, it seems that the apparent edge shift is due to structural geometry combined with the dipole field effect [31]. Therefore ROIs should be drawn around the magnitude image (or $R_2^\star$ image) and not the phase image, if phase within the true structure is to be measured.

When comparing phase measures within structures to known brain iron concentrations, phase may not be reliable between different structures, as seen by the wide variability in regression slopes between phase and $R_2^\star$ between structures, but could be used to evaluate the relative iron changes in the same structure across subjects. Several studies have compared phase across different structures to estimated iron content [13, 19], however a more appropriate measure would be phase within one structure across subjects [9, 29]. The variability in the regression between phase and $R_2^\star$ between structures is exemplified by the negative regression in the SN which

Table 2.3: Phase - $R_2^\star$ regression for PUT with TE-phase =16 ms.

Phase measure (baseline)	Filter width	Slope (ppm*s) x 10^{-4}	R	p-Value
Whole (baseline subcortical)	0.2	3.12	0.87	0.00
	0.125	4.28	0.88	0.00
	0.094	4.67	0.84	0.00
	0.063	5.10	0.71	0.00
Whole (baseline adjacent)	0.2	7.63	0.82	0.00
	0.125	10.07	0.83	0.00
	0.094	11.17	0.84	0.00
	0.063	11.13	0.86	0.00
Lateral (baseline subcortical)	0.2	4.20	0.86	0.00
	0.125	4.55	0.77	0.00
	0.094	4.25	0.68	0.01
	0.063	4.21	0.60	0.02
Posterior (baseline subcortical)	0.2	4.07	0.93	0.00
	0.125	6.01	0.92	0.00
	0.094	7.09	0.90	0.00
	0.063	9.26	0.90	0.00
Posterior lateral (baseline subcortical)	0.2	5.08	0.90	0.00
	0.125	6.35	0.87	0.00
	0.094	6.83	0.84	0.00
	0.063	8.59	0.84	0.00
Posterior (baseline adjacent)	0.2	8.87	0.93	0.00
	0.125	12.05	0.95	0.00
	0.094	13.54	0.95	0.00
	0.063	14.38	0.95	0.00

is attributed to the complicated three-dimensional geometry of the structure, unlike the more cylindrical RN. This could be an important feature when studying the SN because it has been reported that the phase evolves with Parkinson's disease progression and iron accumulation [27], or in normal individuals with ageing [41, 14]. However our study shows phase evolution in the opposite direction with increasing iron content, although all results are significant. Due to the nonlocal dipolar effects as seen in Figs. 2.1 and 2.2, the most intense phase may be outside of the structure in the superior-inferior plane. With ROI placement based on phase imaging only, the measured phase could be outside of the actual structure, in the superior imaging slice. As well, the in-plane edges of the structure may be difficult to discern due to phase geometry effects as seen in Fig. 2.3. The ROIs in our study were drawn on $R_2^\star$ images to eliminate the out-of-plane phase effects and the ambiguity at the edges of structures on the phase images. While the out-of-plane measure on phase images could prove useful, it is important to accurately describe the spatial location

Table 2.4: Phase - $R_2^\star$ regression for GP with TE-phase =16 ms.

Phase measure (baseline)	Filter width	Slope (ppm*s) x 10^{-4}	R	p-Value
Whole (baseline subcortical)	0.2	1.10	0.16	0.56
	0.125	0.81	0.08	0.79
	0.094	0.12	0.01	0.98
	0.063	2.84	0.12	0.98
Lateral (baseline subcortical)	0.2	4.16	0.40	0.15
	0.125	6.06	0.50	0.07
	0.094	7.72	0.52	0.05
	0.063	10.99	0.44	0.12
Posterior (baseline subcortical)	0.2	-0.59	0.06	0.83
	0.125	-1.14	0.09	0.77
	0.094	-0.99	0.06	0.83
	0.063	2.56	0.11	0.70
Posterior lateral (baseline subcortical)	0.2	-5.35	0.41	0.15
	0.125	7.73	0.48	0.08
	0.094	8.74	0.47	0.09
	0.063	9.52	0.40	0.16
Posterior lateral (baseline adjacent)	0.2	9.66	0.32	0.27
	0.125	12.54	0.34	0.23
	0.094	14.63	0.39	0.17
	0.063	16.09	0.41	0.15

of ROIs in both phase and magnitude images for reproducibility and comparison with other studies.

The baseline phase in an image is somewhat arbitrary and depends on factors such as shimming and global susceptibility effects therefore phase measured in structures is typically compared to another region in the brain. As well, neighboring susceptibility sources outside of the slice of interest must also be considered in order to obtain an accurate phase measure, as demonstrated in the simulation of the SN and RN. When using axial plane slices, it is somewhat fortuitous that the inferior SN and RN are not directly in line with the more superior GP and PUT, which means these iron-rich structures do not have a direct effect on each other, but do have an effect on the neighboring background. To overcome this, the baseline phase measurement should be obtained directly adjacent to the structure of interest to mitigate the effects of other susceptibility sources such as air tissue interfaces or endogenous structures. The in vivo data shows higher correlations between phase and $R_2^\star$ when baseline measures of phase are obtained adjacent to structures compared to a distant area of subcortical WM in the SN and RN. The GP correlation was not stronger with the adjacent baseline measure possibly because of the close proximity of the SN causing a strong susceptibility effect. The correlations between phase and

Table 2.5: Phase-$R_2^\star$ regression for RN and SN with TE-phase =16 ms.

Phase measure (baseline)	Filter width	Slope (ppm*s) x 10^{-4}	R	p-Value
RN Whole (baseline subcortical)	0.2	3.22	0.69	0.01
	0.125	5.48	0.72	0.00
	0.094	6.59	0.71	0.00
	0.063	8.47	0.55	0.04
RN Whole (baseline adjacent)	0.2	7.41	0.80	0.01
	0.125	10.24	0.81	0.00
	0.094	10.73	0.76	0.00
	0.063	6.17	0.37	0.19
RN Posterior (baseline subcortical)	0.2	4.19	0.64	0.01
	0.125	5.83	0.62	0.02
	0.094	6.85	0.58	0.03
	0.063	9.47	0.43	0.13
SN whole (baseline subcortical)	0.2	-8.19	0.58	0.03
	0.125	-14.64	0.54	0.04
	0.094	-18.14	0.49	0.08
	0.063	-18.59	0.33	0.25
SN whole (baseline adjacent)	0.2	-9.58	0.65	0.01
	0.125	-14.74	0.67	0.01
	0.094	-15.66	0.64	0.01
	0.063	-13.96	0.51	0.06

$R_2^\star$ were similar for the PUT with both baseline measures, possibly because both measures are close in proximity.

Measuring the edge phase rather than the whole structure gives less change in slope of the regression line for PUT, GP, and RN. As well, when the whole structure was measured, the slope of the regression decreased as the filter strength increased. This supports the idea that filtering affects the measured phase more in structures with a higher iron content within axially viewed structures compared to the same structures with lower iron content. As well, the filtering effect is stronger in the center of structures. This filtering effect is most clearly demonstrated in the GP as the correlation between phase and $R_2^\star$ is weak and is only significant when the ROI is measured around the medial border. The large in-plane dimensions of the GP and its high iron content leads to lower phase values post filtering in the middle of the structure. Haacke et al. (2007) [22] found that measuring phase from different ROIs in the PUT produced drastically different phase results and attributed this to different iron accumulation patterns. As well, Zivadinov et al. (2010) [42] and Haacke et al. (2010) [41] described iron accumulation patterns in the GP and PUT and Grabner et al. (2010) [43] describe iron accumulation in the posterior aspect of the PUT in Parkinson's disease. These patterns are similar to the results of

filtering and dipole effects demonstrated in Figs. 2.1 and 2.2. This suggests that the observed iron accumulation pattern in these studies with the standard phase filtering method might be attributed to filtering and susceptibility dipole effects. With the standard phase filtering method, an increase in iron may not show a large increase in phase within a highly filtered area. To overcome this, ROIs should be placed around specific parts of structures and these sub-ROIs analyzed across subjects to better reveal the pattern of iron changes. Therefore, iron accumulation patterns within specific structures could be studied with the standard phase filtering method if many subROIs are examined.

Filter width should be chosen based on structure shape, size, and regional susceptibility influences. The simulation would suggest that the lowest filter width is the most desirable to remove the slow varying phase effects, as the phase values in a structure are least affected both in the middle and at the edges of the structures. However, the in vivo data suggest susceptibility artifact from the sinuses and other baseline phase influences, while not visually apparent, can alter the inherent phase measures due to local susceptibility, therefore the smallest filter width is not always appropriate. This is apparent with the relatively lower correlation between phase and $R_2^\star$ in the RN and SN with the smallest filter width compared to phase measures with higher filter widths in these structures. As well, measuring phase in the PUT benefits with a higher $R_2^\star$ vs phase correlation when ROIs are taken in the posterior aspect of the structure, compared to the whole structure. This effect in the SN, RN, and anterior PUT at small filter widths is due to the background susceptibility effect from the air tissue interface of the paranasal sinuses and nasal cavity. The slope of the regression between phase and $R_2^\star$ in a structure increases as filter width decreases which is desired in neurological studies to separate high from low iron containing structures. However, as the filter width decreases, the correlation between phase and $R_2^\star$ decreases, which reduces the power of statistical analysis in discerning normal from high iron accumulation states. This correlation is increased by measuring the baseline ROI directly adjacent to the structure of interest to mitigate the effects of background susceptibility.

Because the SN and RN are smaller structures with broader k-space representations, it is expected that there would not be as much phase variation measured in simulation with Eq. 2.1 across different filter widths. However the in vivo results show that there is considerable variation with filter width. A drawback of the simulation is the assumption of homogenous susceptibility throughout each structure and no susceptibility effect from other brain tissue. While the paired t-test for $R_2^\star$ measures from edge to middle of a structure show homogeneity of $R_2^\star$ measures for the PUT, SN and RN, this is for only one axial slice and for one cross section. A zero susceptibility value was assigned to surrounding tissue to clarify iron rich structure

effects and because the distant baseline phase is not used in any simulation measurements. The influence of other external tissues is not accounted for in the model and this could produce additional susceptibility effects giving rise to the differences found in vivo. Nevertheless, the simplistic model served to clarify and accurately predict effects in the GP and PUT.

Some studies have investigated susceptibility mapping techniques [30, 44, 45], an image processing step after phase imaging, which removes dipolar artifacts from phase images to find susceptibility distributions. While these techniques look promising to uncover accurate brain susceptibility values, they are currently complicated to implement with issues such as highly involved image processing, multiple patient orientations, or image artifact.

To optimize the precision of phase imaging for estimating tissue susceptibility, ROIs should be placed and interpreted with knowledge of external phase effects and filtering effects, and baseline phase measures should be obtained immediately adjacent to the SN and RN and close to the PUT for the PUT and GP measures. Many sub-ROIs should be obtained across subjects, in order to discern the relative quantity and location of iron accumulation within a structure. Although phase is influenced by filtering and external susceptibility sources, good correlations are observed between phase measures and $R_2^\star$. Smaller filter widths will elucidate the differences between high iron and low iron states while adjacent baseline phase measures will improve the accuracy of the measured phase. Of the filter widths used in this study, the best choices are 0.125 for the SN and RN and 0.094 for the GP and PUT or 0.063 for the posterior GP and PUT to remove the global susceptibility effect and preserve the phase due to endogenous brain structures.

2.6 Conclusions

Phase imaging with the high pass filtering method uses standard MRI sequences and processing software that are widely available, and reveals susceptibility information that was previously confounded by other tissue parameters. The accuracy of measured phase to tissue susceptibility was optimized using simulated phase images, to predict both field effects and filtering effects, and was verified in vivo by comparing phase to $R_2^\star$. The simulated field effects, as demonstrated in sectional profiles, showed the most profound effects in the PUT from the external field effects caused by the neighboring GP and substantial changes in baseline phase around the SN and RN. The in vivo phase comparison to $R_2^\star$ showed that phase is most accurately measured on a structure by structure basis, with appropriate filter width for the size of structure, and with the background phase obtained directly adjacent to the SN and RN. Using a standard filter of 0.125 the slopes and correlation coefficients were

4.28 x 10^{-4} ppm*s and R = 0.88 for the PUT, 0.81 x 10^{-4} ppm*s and R = 0.08 for the GP, 5.48 x 10^{-4} ppm*s and R=0.72 for the RN and 14.64 x 10^{-4} ppm*s and R=0.54 for the SN. To achieve the most effective correlation to $R_2^\star$ we recommend using a filter width of 0.094 for the GP and PUT and 0.125 for the SN and RN. The baseline phase measure should be obtained directly adjacent to the SN, and RN as opposed to an area of distant subcortical WM. The correlation improved using the adjacent measures compared to the subcortical measure in the SN from R = 0.54 to 0.67 and in the RN from R = 0.72 to 0.81, using a filter width of 0.125. Different regression slopes are seen between subROIs within structures suggesting that regional iron accumulation within a structure is best studied with subROIs between different subject groups, not differences in phase values relative to the overall phase in one structure. Phase imaging has the potential for more sensitive comparisons of brain iron accumulation in deep grey matter if specific filtering parameters and susceptibility effects are carefully considered.

2.7 Acknowledgments

Operating grants from the Canadian Institutes of Health Research (CIHR) and the Natural Sciences and Engineering Research Council of Canada (NSERC) are acknowledged. AJW was supported by a Vanier Canada Graduate Scholarship, and an Alberta Innovates Health Solutions MD/PhD studentship.

Bibliography

[1] Haacke EM, Xu Y, Cheng YC, Reichenbach JR. Susceptibility weighted imaging (SWI). Magnetic Resonance in Medicine 2004;52(3):612–8.

[2] Ogg RJ, Langston JW, Haacke EM, Steen RG, Taylor JS. The correlation between phase shifts in gradient-echo MR images and regional brain iron concentration. Magn Reson Imaging 1999;17(8):1141–8.

[3] Bartzokis G, Tishler TA. MRI evaluation of basal ganglia ferritin iron and neurotoxicity in Alzheimer's and Huntingon's disease. Cellular and Molecular Biology 2000;46(4):821–833.

[4] Baudrexel S, Nurnberger L, Rub U, Seifried C, Klein JC, Deller T, Steinmetz H, Deichmann R, Hilker R. Quantitative mapping of T1 and T2* discloses nigral and brainstem pathology in early Parkinson's disease. Neuroimage 2010; 51(2):512–20.

[5] Pinero DJ, Connor JR. Iron in the brain: An important contributor in normal and diseased states. Neuroscientist 2000;6(6):435–453.

[6] Haacke EM, Makki M, Ge YL, Maheshwari M, Sehgal V, Hu JN, Selvan M, Wu Z, Latif Z, Xuan Y, Khan O, Garbern J, Grossman RI. Characterizing Iron Deposition in Multiple Sclerosis Lesions Using Susceptibility Weighted Imaging. Journal of Magnetic Resonance Imaging 2009;29(3):537–544.

[7] Eissa A, Lebel RM, Korzan JR, Zavodni AE, Warren KG, Catz I, Emery DJ, Wilman AH. Detecting lesions in multiple sclerosis at 4.7 tesla using phase susceptibility-weighting and T2-weighting. J Magn Reson Imaging 2009; 30(4):737–42.

[8] Haacke EM, Mittal S, Wu Z, Neelavalli J, Cheng YC. Susceptibility-weighted imaging: technical aspects and clinical applications, part 1. AJNR Am J Neuroradiol 2009;30(1):19–30.

[9] Hammond KE, Metcalf M, Carvajal L, Okuda DT, Srinivasan R, Vigneron D, Nelson SJ, Pelletier D. Quantitative In Vivo Magnetic Resonance Imaging of Multiple Sclerosis at 7 Tesla with Sensitivity to Iron. Annals of Neurology 2008; 64(6):707–713.

[10] Bermel RA, Puli SR, Rudick RA, Weinstock-Guttman B, Fisher E, Munschauer r F E, Bakshi R. Prediction of longitudinal brain atrophy in multiple sclerosis by gray matter magnetic resonance imaging T2 hypointensity. Arch Neurol 2005;62(9):1371–6.

[11] Mitsumori F, Watanabe H, Takaya N. Estimation of Brain Iron Concentration In Vivo Using a Linear Relationship Between Regional Iron and Apparent Transverse Relaxation Rate of the Tissue Water at 4.7T. Magnetic Resonance in Medicine 2009;62(5):1326–1330.

[12] Hammond KE, Lupo JM, Xu D, Metcalf M, Kelley DA, Pelletier D, Chang SM, Mukherjee P, Vigneron DB, Nelson SJ. Development of a robust method for generating 7.0 T multichannel phase images of the brain with application to normal volunteers and patients with neurological diseases. Neuroimage 2008; 39(4):1682–92.

[13] Hopp K, Popescu BF, McCrea RP, Harder SL, Robinson CA, Haacke ME, Rajput AH, Rajput A, Nichol H. Brain iron detected by SWI high pass filtered phase calibrated with synchrotron X-ray fluorescence. Journal of Magnetic Resonance Imaging 2010;31(6):1346–54.

[14] Xu X, Wang Q, Zhang M. Age, gender, and hemispheric differences in iron deposition in the human brain: an in vivo MRI study. Neuroimage 2008; 40(1):35–42.

[15] Schafer A, Wharton S, Gowland P, Bowtell R. Using magnetic field simulation to study susceptibility-related phase contrast in gradient echo MRI. Neuroimage 2009;48(1):126–137.

[16] Lee J, Shmueli K, Fukunaga M, van Gelderen P, Merkle H, Silva AC, Duyn JH. Sensitivity of MRI resonance frequency to the orientation of brain tissue microstructure (vol 107, pg 5130, 2010). Proceedings of the National Academy of Sciences of the United States of America 2010;107(18):8498–8498.

[17] Duyn JH, van Gelderen P, Li TQ, de Zwart JA, Koretsky AP, Fukunaga M. High-field MRI of brain cortical substructure based on signal phase. Proc Natl Acad Sci U S A 2007;104(28):11796–801.

[18] He X, Yablonskiy DA. Biophysical mechanisms of phase contrast in gradient echo MRI. Proc Natl Acad Sci U S A 2009;106(32):13558–63.

[19] Wharton S, Bowtell R. Whole-brain susceptibility mapping at high field: a comparison of multiple- and single-orientation methods. Neuroimage 2010; 53(2):515–25.

[20] Neelavalli J, Cheng YCN, Jiang J, Haacke EM. Removing Background Phase Variations in Susceptibility-Weighted Imaging Using a Fast, Forward-Field Calculation. Journal of Magnetic Resonance Imaging 2009;29(4):937–948.

[21] Yao B, Li TQ, Gelderen P, Shmueli K, de Zwart JA, Duyn JH. Susceptibility contrast in high field MRI of human brain as a function of tissue iron content. Neuroimage 2009;44(4):1259–66.

[22] Haacke EM, Ayaz M, Khan A, Manova ES, Krishnamurthy B, Gollapalli L, Ciulla C, Kim I, Petersen F, Kirsch W. Establishing a baseline phase behavior in magnetic resonance imaging to determine normal vs. abnormal iron content in the brain. Journal of Magnetic Resonance Imaging 2007;26(2):256–264.

[23] Wang Y, Yu Y, Li D, Bae KT, Brown JJ, Lin W, Haacke EM. Artery and vein separation using susceptibility-dependent phase in contrast-enhanced MRA. Journal of Magnetic Resonance Imaging 2000;12(5):661–670.

[24] Gupta D, Saini J, Kesavadas C, Sarma PS, Kishore A. Utility of susceptibility-weighted MRI in differentiating Parkinson's disease and atypical parkinsonism. Neuroradiology 2010;52(12):1087–94.

[25] Rossi M, Ruottinen H, Elovaara I, Ryymin P, Soimakallio S, Eskola H, Dastidar P. Brain Iron Deposition and Sequence Characteristics in Parkinsonism: Comparison of SWI, T2* Maps, T2-Weighted-, and FLAIR-SPACE. Invest Radiol 2010;.

[26] Szumowski J, Bas E, Gaarder K, Schwarz E, Erdogmus D, Hayflick S. Measurement of brain iron distribution in Hallevorden-Spatz syndrome. J Magn Reson Imaging 2010;31(2):482–9.

[27] Zhang JQ, Zhang YL, Wang J, Cai P, Luo CX, Qian ZM, Dai YM, Feng H. Characterizing iron deposition in Parkinson's disease using susceptibility-weighted imaging: An in vivo MR study. Brain Research 2010;1330:124–130.

[28] Zhu WZ, Zhong WD, Wang W, Zhan CJ, Wang CY, Qi JP, Wang JZ, Lei T. Quantitative MR phase-corrected imaging to investigate increased brain iron deposition of patients with Alzheimer disease. Radiology 2009;253(2):497–504.

[29] Pfefferbaum A, Adalsteinsson E, Rohlfing T, Sullivan EV. MRI estimates of brain iron concentration in normal aging: comparison of field-dependent (FDRI) and phase (SWI) methods. Neuroimage 2009;47(2):493–500.

[30] de Rochefort L, Liu T, Kressler B, Liu J, Spincemaille P, Lebon V, Wu JL, Wang Y. Quantitative Susceptibility Map Reconstruction from MR Phase Data Using Bayesian Regularization: Validation and Application to Brain Imaging. Magnetic Resonance in Medicine 2010;63(1):194–206.

[31] Deistung A, Rauscher A, Sedlacik J, Stadler J, Witoszynskyj S, Reichenbach JR. Susceptibility Weighted Imaging at Ultra High Magnetic Field Strengths: Theoretical Considerations and Experimental Results. Magnetic Resonance in Medicine 2008;60(5):1155–1168.

[32] Langkammer C, Krebs N, Goessler W, Scheurer E, Ebner F, Yen K, Fazekas F, Ropele S. Quantitative MR imaging of brain iron: a postmortem validation study. Radiology 2010;257(2):455–62.

[33] Haacke EM, Miao Y, Liu M, Habib CA, Katkuri Y, Liu T, Yang Z, Lang Z, Hu J, Wu J. Correlation of putative iron content as represented by changes in R2* and phase with age in deep gray matter of healthy adults. J Magn Reson Imaging 2010;32(3):561–76.

[34] Marques JP, Bowtell R. Application of a fourier-based method for rapid calculation of field inhomogeneity due to spatial variation of magnetic susceptibility. Concepts in Magnetic Resonance Part B-Magnetic Resonance Engineering 2005;25B(1):65–78.

[35] Salomir R, De Senneville BD, Moonen CTW. A fast calculation method for magnetic field inhomogeneity due to an arbitrary distribution of bulk susceptibility. Concepts in Magnetic Resonance Part B-Magnetic Resonance Engineering 2003;19B(1):26–34.

[36] Du YPP, Jin ZY, Hu YZ, Tanabe J. Multi-Echo Acquisition of MR Angiography and Venography of the Brain at 3 Tesla. Journal of Magnetic Resonance Imaging 2009;30(2):449–454.

[37] Denk C, Rauscher A. Susceptibility weighted imaging with multiple echoes. J Magn Reson Imaging 2010;31(1):185–91.

[38] Lee J, Hirano Y, Fukunaga M, Silva AC, Duyn JH. On the contribution of deoxy-hemoglobin to MRI gray-white matter phase contrast at high field. Neuroimage 2010;49(1):193–8.

[39] Petridou N, Wharton SJ, Lotfipour A, Gowland P, Bowtell R. Investigating the effect of blood susceptibility on phase contrast in the human brain. Neuroimage 2010;50(2):491–8.

[40] O'Gorman RL, Shmueli K, Ashkan K, Samuel M, Lythgoe DJ, Shahidiani A, Wastling SJ, Footman M, Selway RP, Jarosz J. Optimal MRI methods for direct stereotactic targeting of the subthalamic nucleus and globus pallidus. Eur Radiol 2010;.

[41] Haacke EM, Ayaz M, Boikov AS, Kido DK, Kirsch WM. Imaging Cerebral Microbleeds Using Susceptibility Weighted Imaging: One Step Toward Detecting Vascular Dementia. Journal of Magnetic Resonance Imaging 2010;31(1):142–148.

[42] Zivadinov R, Schirda C, Dwyer MG, Haacke ME, Weinstock-Guttman B, Menegatti E, Heininen-Brown M, Magnano C, Malagoni AM, Wack DS, Hojnacki D, Kennedy C, Carl E, Bergsland N, Hussein S, Poloni G, Bartolomei I, Salvi F, Zamboni P. Chronic cerebrospinal venous insufficiency and iron deposition on susceptibility-weighted imaging in patients with multiple sclerosis: a pilot case-control study. Int Angiol 2010;29(2):158–75.

[43] Grabner G, Haubenberger D, Rath J, Beisteiner R, Auff E, Trattnig S, Barth M. A population-specific symmetric phase model to automatically analyze susceptibility-weighted imaging (SWI) phase shifts and phase symmetry in the human brain. J Magn Reson Imaging 2010;31(1):215–20.

[44] Shmueli K, de Zwart JA, van Gelderen P, Li TQ, Dodd SJ, Duyn JH. Magnetic Susceptibility Mapping of Brain Tissue In Vivo Using MRI Phase Data. Magnetic Resonance in Medicine 2009;62(6):1510–1522.

[45] Wharton S, Schafer A, Bowtell R. Susceptibility mapping in the human brain using threshold-based k-space division. Magnetic Resonance in Medicine 2010; 63(5):1292–304.

Chapter 3

Susceptibility Phase Imaging With Improved Image Contrast Using Moving Window Phase Gradient Fitting and Minimal Filtering [1]

3.1 Abstract

Purpose: To enhance image contrast in susceptibility phase imaging using a new method of background phase removal.

Materials and Methods: A background phase removal method is proposed that uses the spatial gradient of the raw phase image to perform a moving window third-order local polynomial estimation and correction of the raw phase image followed by minimal high pass filtering. The method is demonstrated in simulation, 10 healthy volunteers, and 5 multiple sclerosis patients in comparison to a standard phase filtering approach.

Results: Compared to standard phase filtering, the new method increased phase contrast with local background tissue in subcortical grey matter, cortical grey matter, and multiple sclerosis lesions by 67% ± 33%, 13% ± 7%, and 48% ± 19%, respectively (95% confidence interval). In addition, the new method removed more phase wraps in areas of rapidly changing background phase.

Conclusion: Local phase gradient fitting combined with minimal high pass fil-

[1] A version of this section has been published. Walsh AJ, Wilman AH, Eissa A, Blevins G. Susceptibility Phase Imaging With Improved Image Contrast Using Moving Window Phase Gradient Fitting and Minimal Filtering. Journal of Magnetic Resonance Imaging 2012, 14601469.

tering provides better tissue depiction and more accurate phase quantification than standard filtering.

3.2 Introduction

The primary sources of susceptibility affecting phase contrast in brain tissue are iron, myelin, calcium, and air [1, 2]. Visualization or quantification of these susceptibility sources can be achieved with phase imaging [3], susceptibility-weighted imaging (SWI) [4], or susceptibility mapping [5]. However, all of these methods first require background phase removal. Background phase arises from sources of magnetic field variation external to the region of interest (ROI). This includes boundaries between regions of significantly different magnetic susceptibility, most notably at the airtissue interfaces in the sinuses and at the surface of the head [6].

The most widely reported phase removal method uses a threshold k-space, high pass filter approach to remove slowly varying background phase due to susceptibility sources external to the brain tissue [4, 7, 8, 9]. Limitations of the standard filtering method include suppression of phase values in larger structures and lack of background removal in areas of the brain with rapidly varying background phase, such as near the paranasal sinuses [10]. In addition, phase quantification in deep grey matter is altered by strong filter values while weaker filters might not properly remove background phase [11]. Variable filters have been proposed for improved visualization [12, 13, 14], but may have potentially confounding diagnostic value due to nonuniform processing. As well, assumptions are made about edge locations in the brain which could be problematic when visualizing certain localized pathologies near the brain surface such as cortical multiple sclerosis (MS) lesions or cortical vein thrombosis [15]. Using the weakest possible filter while still removing all of the global background phase is desirable for maximum contrast; however, these goals are contradictory.

Recent alternatives to filtering include sophisticated harmonic artifact reduction for phase data (SHARP) [16] and projection onto dipole fields (PDF) [17]. As well, polynomial fitting to the whole brain [18] or within a moving window [19] have also been implemented. However, these methods experience problems near the outer brain surface with removal of pixels using SHARP or violation of assumptions using PDF. Moreover, the polynomial fitting methods can also suffer from phase suppression in larger structures if the polynomial matches the structure contour, rather than the background phase, because of a high-order polynomial or small fitting territory. All of these alternative methods require phase unwrapping prior to background phase removal. There is a wide variety of unwrapping algorithms that are generally effective, but many algorithms can be less robust in areas of

extremely large phase variation or areas with a low signal-to-noise ratio (SNR) as described by Bagher-Ebadian et al [20], Rauscher et al [21], Langley and Zhao [22], and Witoszynkyj et al [23]. For phase unwrapping, the 2π surfaces are trivial to detect provided they are distinct from regions where adjacent pixels differ by less than π, and there is adequate SNR. In cases of excessive noise, rapidly varying phase or phase discontinuities, phase unwrapping becomes very difficult, although complex algorithms may overcome this [21, 22].

In this work, we apply a background phase removal method that determines local polynomial coefficients to the raw phase image without requiring unwrapping or image masking. The method relies on a moving window analytical estimation of the raw phase based on a least-squares calculation of the spatial gradient of the raw phase image to locally smooth the background phase followed by the application of a weak filter. The new method is tested against standard phase filtering in simulation, healthy volunteers, and MS patients.

3.3 Materials and Methods

3.3.1 Phase Removal Method Overview

The new phase removal method makes use of a moving window approach to perform local, analytical determination of polynomial coefficients of the raw phase using the phase gradient. There are five main steps: 1) computation of spatial gradient maps in the x and y direction from the raw phase; 2) analytical determination of local polynomial coefficients to the raw phase from the phase gradient maps within a square fitting window; 3) phase correction of the original complex image based on the determined polynomial coefficients producing a locally smoothed phase profile within the fitting window; 4) minimal high pass filtering using a k-space approach; then 5) extraction from each corrected image of a square portion, called the extraction window, that is centered within the square fitting window. Steps 2 to 5 are repeated, using the information from step 1, moving both the fitting and extraction window by half the dimension of the extraction window in the x and y direction until the full image is covered. The individual extraction windows are subsequently combined into a final image. The entire procedure is outlined in Fig. 3.1. Unwrapping is not required as the spatial gradient is used to locally estimate polynomial coefficients to the raw phase data using a least-squares approach to the gradient information where phase wraps, determined by extreme gradient values, are excluded from the fitting. If a polynomial were fit to the raw phase directly, rather than using the phase gradient, an unwrapping algorithm would be required.

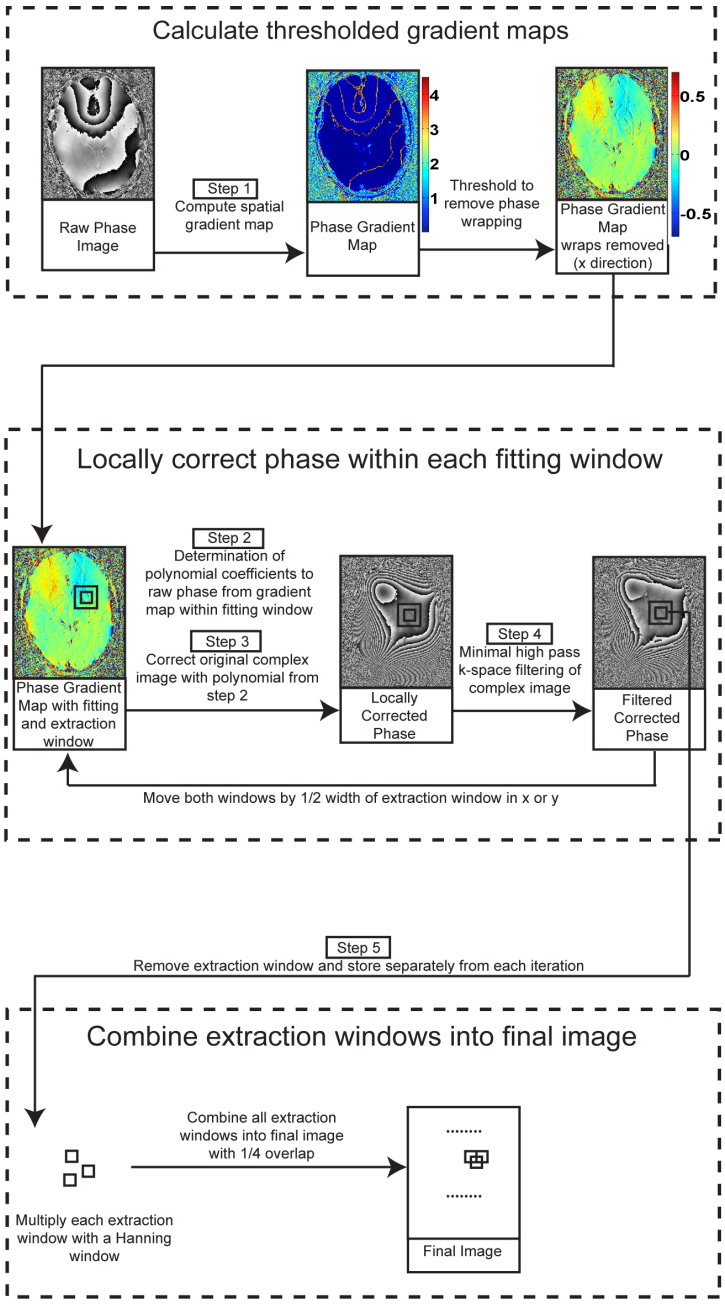

Figure 3.1: Flowchart illustrating the phase removal algorithm beginning with the raw phase image. Two square boxes show the square fitting (larger) and extraction (smaller) windows in steps 2-5. One iteration is shown; however, the moving fitting and extraction windows cover the full image for complete implementation. Color bars for the gradient maps are in units of radians/pixel. The phase gradient map directly after step 1 is calculated with sqrt($g_x^2 + g_y^2$) where g_x and g_y are the gradient maps in the x and y direction. The gradient maps following this show the x direction only; however, both x and y gradient maps are used in the algorithm.

3.3.2 Phase Removal Method Details

In step 1, the spatial gradient of a 2D raw phase image is obtained in the x and y dimensions over the whole image, creating two separate gradient maps. Both gradient maps, generated using the MatLab (MathWorks, Natick, MA) 2011a gradient function, are thresholded at $\sqrt{g_x^2 + g_y^2} > 2.5$ rads/pixel, where g_x and g_y are the values of the gradient data in the x direction and y direction. The thresholded regions are excluded in the least-squares fit. The phase gradient at locations of phase wraps has a much higher gradient value than unaffected regions, which have gradient values of less than 1 rad/pixel in this work.

In step 2, the phase gradient data are used to locally estimate a third-order polynomial fit to the original phase data within each fitting window using a new gradient least-squares approach. The coefficients for a 2D polynomial estimate to the raw background phase are calculated by minimizing the residual of the partial derivatives of this polynomial to the gradient data. The analytical process is illustrated using a second-order polynomial fit, which can be extended to higher orders. Equations 3.1 to 3.6 show the sums of squares fit to the gradient data, where $p(x, y)$ is the estimated polynomial fit to the original raw phase image, p_x is the estimated value of the gradient data in the x direction, and p_y is the estimated value of the gradient data in the y direction. The computed gradients of the original phase image are g_x and g_y in the x and y direction, respectively. A second-order polynomial fit with coefficients a_{0-5} is shown in Eq. 3.1, with Eqs. 3.1, 3.2 illustrating the partial derivatives to $p(x, y)$ in the x and y directions, respectively, Eq. 3.4 the minimization function, and Eqs. 3.5a - 3.6 the sum of squares fit.

$$p(x, y) = a_0 + a_1 x + a_2 x + a_3 xy + a_4 x^2 + a_5 y^2 \tag{3.1}$$

$$p_x = \frac{\partial p}{\partial x} = a_1 x + a_3 y + a_4 2x \tag{3.2}$$

$$p_y = \frac{\partial p}{\partial y} = a_2 x + a_3 x + a_5 2y \tag{3.3}$$

$$S_r = \sum (g_x - a_1 - a_3 y - a_4 2x)^2 + \sum (g_y - a_2 - a_3 x - a_5 2y)^2 \tag{3.4}$$

The index sum is over the pixels within the fitting window. Taking partial derivatives with respect to the constant terms gives:

$$\frac{\partial S_r}{\partial a_1} = -2 \sum (g_x - a_1 - a_3 y - a_4 2x) = 0 \tag{3.5a}$$

$$\frac{\partial S_r}{\partial a_2} = -2\sum(g_y - a_2 - a_3x - a_5 2y) = 0 \tag{3.5b}$$

$$\frac{\partial S_r}{\partial a_3} = -2\sum(g_x - a_1 - a_3y - a_4 2x)y - 2\sum(g_y - a_2 - a_3x - a_5 2y)x = 0 \tag{3.5c}$$

$$\frac{\partial S_r}{\partial a_4} = -2\sum(g_x - a_1 - a_3y - a_4 2x)2x = 0 \tag{3.5d}$$

$$\frac{\partial S_r}{\partial a_5} = -2\sum(g_y - a_2 - a_3x - a_5 2y)2y = 0 \tag{3.5e}$$

This can be rearranged to:

$$\begin{bmatrix} n & 0 & \sum y & 2\sum x & 0 \\ 0 & n & \sum x & 0 & 2\sum y \\ \sum y & \sum x & \sum x^2 + \sum y^2 & 2\sum xy & 2\sum xy \\ \sum x & 0 & \sum xy & 2\sum x^2 & 0 \\ 0 & \sum y & \sum xy & 0 & 2\sum y^2 \end{bmatrix} \cdot \begin{bmatrix} a_1 \\ a_2 \\ a_3 \\ a_4 \\ a_5 \end{bmatrix} = \begin{bmatrix} \sum g_x \\ \sum g_y \\ \sum g_x + \sum g_y \\ \sum g_x x \\ \sum g_y y \end{bmatrix} \tag{3.6}$$

where n is the number of data points used within the local fitting window and the index sum is over the pixels in this window. In step 3 the whole original 2D complex image img_{orig} is multiplied, element by element, with a complex exponential to locally correct the phase within a fitting window. This exponential corrects the phase of the complex data with a local third order polynomial estimation of the background phase from coefficients determined in step 2. The whole original complex image is multiplied by this exponential function which yields the corrected image img_{corr}.

$$img_{corr}(x, y) = img_{orig}(x, y) \cdot e^{i(-p(x,y))} \tag{3.7}$$

where $p(x, y)$ is from Eq. 3.1 and the constant a_0 term is not included. This creates a smoothed phase profile within the fitting window and consequently the rest of the image may have a variable phase profile after this step.

In step 4, traditional k-space filtering is applied independently to each locally corrected image generated in step 3 with a less intense filter than standardly used. For traditional filtering, a 2D symmetrical Hanning window is constructed in the central portion of the image k-space and zero padded to the size of the full 2D image [24]. The filter width is defined as the ratio of one dimension of the Hanning window divided by the total image size in that dimension. This central k-space

window is Fourier transformed back to image space. The original 2D complex image is complex divided by the result, creating a high pass effect in phase. A typical filter reported is 0.125 filter width or greater when using a 512 x 512 image matrix [25, 26, 27] for a similar echo time-to-field strength ratio used in this work. This corresponds to a central k-space representation of ±785 rad/m for a 25.6 cm field of view (FOV). In the new method, a 0.0625 filter is also used which corresponds to ±393 rad/m central k-space representation. Weak filtering is applied because higher terms in the polynomial fit are determined with the new fitting method, but not the constant term a_0. The weak filter moves the baseline of each region to zero, which reduces discontinuities between image segments. Other methods could normalize the baseline of individual extraction windows but filtering has the benefit of further removing slow varying background phase.

Finally, in step 5, after filtering each locally corrected image, the central region of the fitting window, the extraction window, is removed from each image according to the location of the local fitting in step 2. This small window is multiplied by a spatial Hanning window of the same in-plane dimensions to further remove slight discontinuities at the window edges. All extraction windows are then combined into a final image where each individual extraction window has a one-quarter overlap with adjacent extraction windows. This overlap results in a final image with a flat profile, if each extraction window has the same offset and is initially flat.

3.3.3 Simulation

A simulated 3D phase model was created in MatLab with dimensions 512 x 512 x 512. Beginning with a large sphere of susceptibility -7 ppm, a smaller sphere was removed from the edge. Several shapes were constructed inside this distribution including a cylinder with susceptibility of -4.82 ppm, and ellipsoids and fine structures each with susceptibility of -4.70 ppm. The Fourier transform of a dipole point source was multiplied to the Fourier transform of the entire susceptibility distribution and the result was inverse Fourier transformed to obtain the field projection from the susceptibility sources. Random phase noise from -π to +π was added outside of the distribution to simulate air. A similar model was created without the large spherical susceptibility distribution to obtain the ideal field representation of the internal structures for postfiltering comparison.

The simulation was tested with the standard filtering method and the new method, both with filter widths of 0.125 and 0.0625. Different square fitting (f) window sizes were tested with a constant square extraction (e) window of 16 pixels width and length. The side lengths of the fitting windows were 32, 48, and 64 pixels (32f x 16e, 48f x 16e, 64f x 16e). The images were visually compared for background field removal in areas with rapidly varying background phase and a profile

was obtained from an internal structure to quantitatively evaluate the extent of phase alteration between methods and between different parameters using the new method.

3.3.4 MRI Acquisition

Following institutional ethical approval and informed consent, images were obtained from 10 healthy volunteers and 5 patients with clinically definite relapsing- remitting MS using axial 2D gradient echo sequences with 512 x 256 encoding matrix. Five volunteers were imaged at 3.0 T with a MR Research Systems console to examine the deep grey matter using seven 3-mm thick contiguous slices and 25 cm square FOV, TE/ TR = 26/500 msec, and 70° flip angle. A 16-element cylindrical birdcage coil was used for transmission and reception. Five patients with relapsing remitting MS and five healthy volunteer were imaged using a 4.7 T Varian Unity Inova system with whole brain imaging using 50 2-mm thick contiguous slices, 25.6 x 19.25 cm FOV, TE/TR = 15/1540 msec, and 62° flip angle. A 16-element cylindrical birdcage coil was used for transmission with a four-element circumscribing receiver array. The raw k-space data were zero-filled to 512 x 512 pixels prior to phase removal processing using standard filtering and the new method with a range of fitting windows, extraction windows, and filter strengths. The 4.7 T acquisitions used an asymmetric FOV, thus giving different k-space step sizes in the two dimensions. For the 4.7T images, the same absolute k-space cutoff was used for the filter in both dimensions, with the filter width definition based on the larger FOV in the frequency encoding dimension. With multiple element receiver arrays from the 4.7T MRI system, the full background phase removal algorithm was performed on each coil independently, then subsequently combined by weighting each phase channel by the magnitude image squared.

3.3.5 Image Analysis

Phase and SWI images using the new method and standard phase filtering were evaluated using both ROI measurements and examination of background phase removal. Quantitative ROI analysis was used to optimize parameters for deep grey matter contrast at 3.0 T. Phase measurements of the globus pallidus (GP), putamen (PUT), head of the caudate (CAUD), and cortical grey matter (GM) were referenced to nearby white matter (WM) that was <5 mm from each structure and compared between filtering methods using a paired t-test. As well, profiles were obtained through the right globus pallidus and putamen, registered, and averaged across the five subjects, then compared between phase removal methods. The profiles were manually selected based on visual correspondence of location and angle in each subject. Registration was implemented using a custom MatLab function to

align structures borders and correct any baseline discrepancies of the 1D profiles. At 4.7 T, 25 significant WM lesions in patients with MS were identified based on phase hypointensity and T_2 hyperintensity. These lesions were compared to background phase measures in nearby tissue <5 mm away. The contrast between lesions using the new method and standard phase filtering was compared with a paired t-test. Qualitative analysis examined images from five healthy subjects at 4.7 T for phase wrap removal superior to the paranasal sinuses and auditory canals. Edge depiction and phase wrap removal were compared to the standard filtering method. In addition, a direct polynomial fit that used phase unwrapping was also compared for phase wrap removal. This method used the same moving window algorithm, but with step 1 replaced with unwrapping using PRELUDE in 2D mode [28] or PhiUn [23] and with step 2, the gradient fitting, replaced with a direct third-order polynomial fit to the unwrapped phase.

3.4 Results

3.4.1 Simulation

Regions near strong background field variation are better visualized with the new method compared to standard filtering (Fig. 3.2). The ellipsoid, near the top of the images (arrow), is not affected by phase wrapping with the new method because it provides better elimination of background field shifts (Fig. 3.2a,b) compared to standard filtering (Fig. 3.2e,f). Since the gradient of the raw phase is rapidly changing near this edge of the large spherical susceptibility distribution, smaller fitting windows and higher filter strengths better eliminate background contributions in Fig. 3.2a compared to a half strength filter and larger fitting window in Fig. 3.2d. However, all of the different parameters tested with the new method eliminate more phase wrapping compared to the standard method (Fig. 3.2).

The fitting window size affects measured phase within large structures as illustrated in Fig. 3.2 and the profiles in Fig. 3.3. The fitting window must be at least as large as the structure of interest to avoid suppression of phase values in the center of the structure which is apparent for a fitting window of size 32 (Fig. 3.2b, 3.3). Finer structures have equivalent contrast using either the standard or new phase removal method, yet slight hyperintensities are present in the simulation with a small fitting window of size 32. Using a standard filter with a low strength of 0.0625 does not remove the background phase properly, while the new method, with the same filter strength, matches the ideal field shift more accurately (Fig. 3.3).

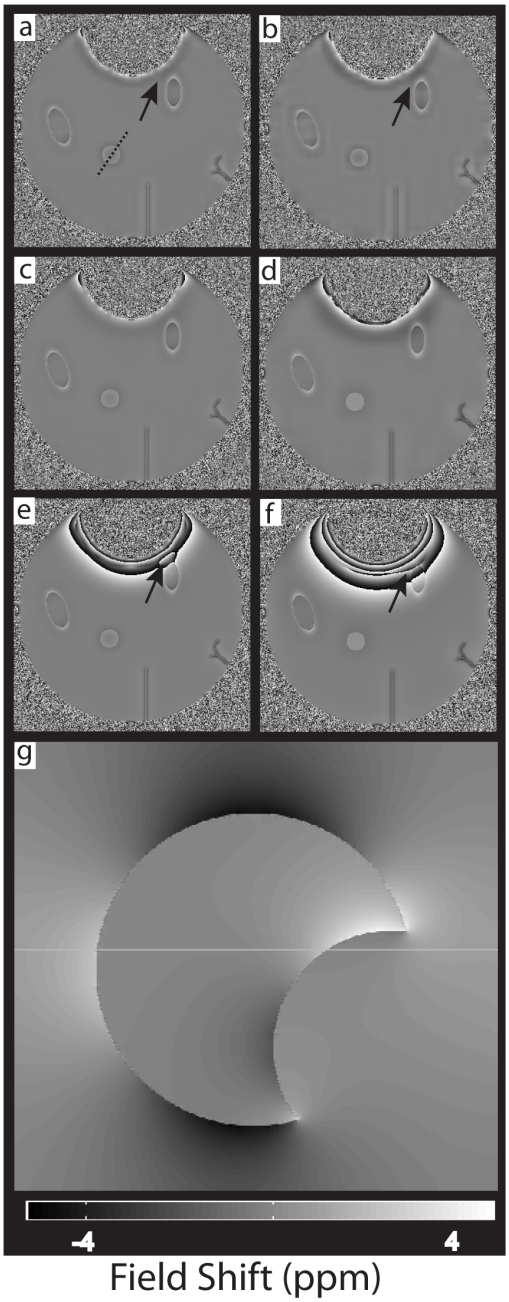

Figure 3.2: Phase susceptibility simulation of a spherical susceptibility distribution with regions removed to create internal background field effects. Internal shapes include a cylinder with the axis along the inferior superior direction, two ellipsoids, and two finer structures. The new phase removal method is shown in axial images using two filtering widths 0.125 (a,c) and 0.0625 (b,d). In (a,b) the square fitting and extraction window is 32f x 16e, while (c,d) use a larger fitting window with same extraction window 64f x 16e. Comparison with the standard filtering method is made in (e,f) using the same filter strengths (e) 0.125 and (f) 0.0625 filter strength. g: Sagittal view of field shift from global susceptibility distribution with location of axial imaging plane of a-f shown. The simulated images use an inverted grey scale for profile comparison. Arrows show difference in background phase removal between methods.

3.4.2 In Vivo

From the phase measures at 3.0 T, the optimum fitting window size is 64 for a 512 x 512 image matrix at TE = 26 msec while different extraction window sizes produce equivalent results (Fig. 3.4). Quantitative phase measures at 3.0 T with the new method using optimized parameters reveal markedly different results from the standard method (Table 3.1). The contrast is increased in the putamen by 31 ± 42%, globus pallidus by 26 ± 13%, caudate by 329 ± 147%, and cortical grey/white matter by 13 ± 7% (95% confidence interval [CI]). The increase in contrast between

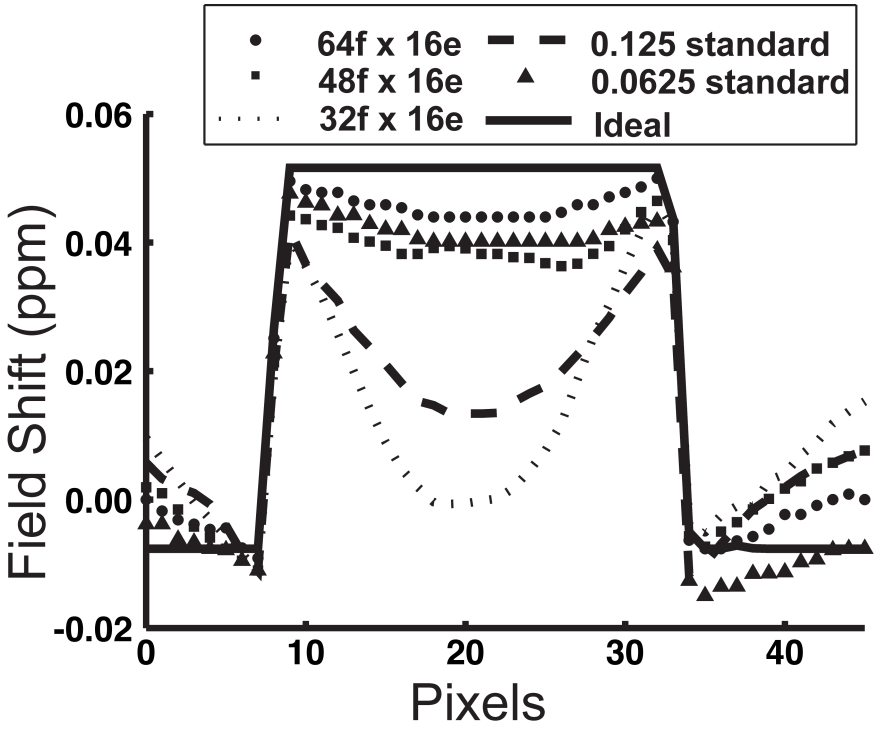

Figure 3.3: Profile through the large cylinder in Fig. 3.2 (dotted line) with the new filtering method using 0.0625 filter strength and three different square fitting (f) and extraction (e) windows. The ideal field shift from the cylinder is shown with no background phase removal and the absence of susceptibility effect from the large sphere. The standard methods are also compared using 0.125 and 0.0625 filter strength.

methods is significant ($P < 0.05$) for all measured structures except the putamen.

Figure 3.5 shows 3.0 T images from a healthy volunteer where, in larger brain structures, the phase is less affected by filtering using the new method (Fig. 3.5a,b). Standard filtering with a weak filter of 0.0625 (Fig. 3.5c) does not properly remove the background phase and wraps are visible in structures of interest. Figure 3.5e shows the average phase contrast from five individuals through a profile of the putamen and globus pallidus. With the new method, the phase is much less suppressed in the globus pallidus (Fig. 3.5e), while the phase in the putamen is similar. Using larger fitting windows slightly decreases the phase contrast in the middle of large structures with flat profiles, such as the globus pallidus. Similar to simulated images, phase suppression in large structures is also seen in vivo when the fitting window size is less than 32.

Lesions in MS patients have greater contrast compared to adjacent tissue using the new phase removal method compared to the standard method. The contrast using the new method and standard filtering are -7.8 $\pm$ 2.7 ppb and -5.2 $\pm$ 2.2 ppb ($P < 0.00001$), respectively, yielding a 48% $\pm$ 19% (95% CI) higher contrast with

Table 3.1: Phase Contrast Relative to Local White Matter Between New and Standard Phase Removal Methods Using Five Subjects at 3.0 T[a]

Structure	New method filter strength 0.0625 fitting=64 extraction=32 avg ± SD	Standard method filter strength 0.125 avg ± SD	p-value[b]
PUT	0.116 ± 0.044	0.088 ± 0.039	0.13
GP	0.243 ± 0.049	0.192 ± 0.054	0.001
CAUD	0.221 ± 0.166	0.067 ± 0.088	0.006
GM/WM	0.203 ± 0.071	0.180 ± 0.067	0.002

[a]Images from 3.0 T use an inverted grey scale.
[b]Analyzed with a repeated measures t-test.

the new filtering method. Figure 3.6 illustrates lesion contrast between methods. Even in brain regions superior to the lateral ventricles, where background field contributions should be less than in more inferior brain regions, standard filtering with 0.0625 filter strength (Fig. 3.6c) does not remove the background phase and lesions are poorly visualized.

Compared to standard phase filtering, in all five healthy subjects at 4.7 T at TE = 15 msec, there are fewer phase wraps visualized using the new method with a filter strength of 0.0625 and square fitting and extraction windows of size 64 and 32, respectively. This is especially evident in areas near large susceptibility differences such as near the paranasal sinuses (Fig. 3.7). In one healthy subject shown in Fig. 3.7 the standard filtering method does not properly depict the substantia nigra and anterior vasculature. Even with low signal on the magnitude image near the auditory canals and paranasal sinuses, the phase image from the new method can reveal underlying tissues, while the standard method cannot because of phase wrapping. The background phase is more completely removed using a smaller fitting window with either filter strength of 0.125 of 0.0625 or a larger fitting window with higher filter strength of 0.125.

Direct polynomial fitting using unwrapped phase images are compared to the gradient fit method using the same five subjects at 4.7 T. In all five subjects, greater phase wrap removal is apparent using the gradient fitting compared to PRELUDE unwrapping. PRELUDE fails in some regions of low SNR and rapidly varying background phase, most notably directly superior to the auditory canals and paranasal sinuses. The new method with gradient fitting removes slightly more phase wraps than an advanced unwrapping algorithm, PhiUn, but the results are similar. The

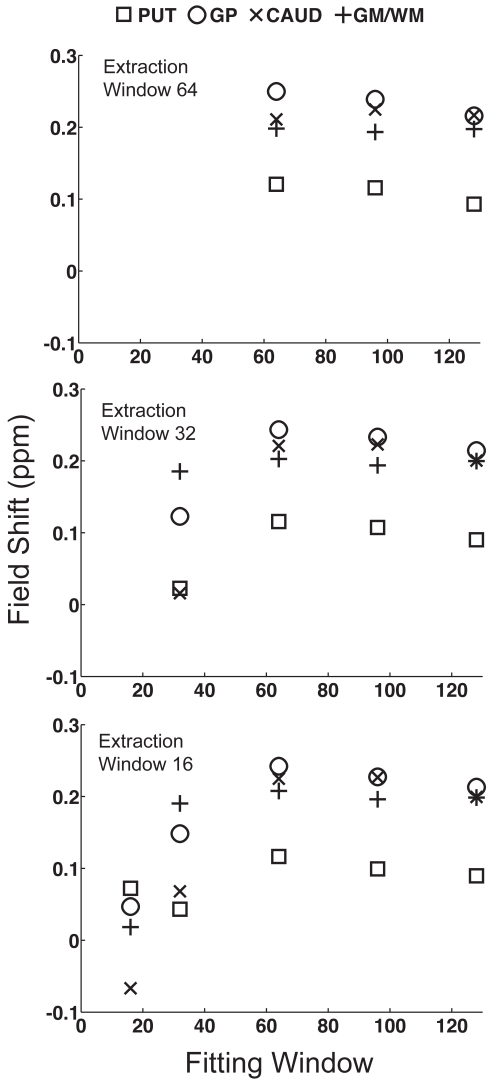

Figure 3.4: Contrast between deep grey matter structures or cortical grey matter and area of adjacent white matter at 3.0 T using different fitting window sizes and extraction window sizes. The filter strength is 0.0625. 3.0 T images use an inverted grey scale.

new background phase removal algorithm with gradient fitting or phase unwrapping with PRELUDE and PhiUn is shown in one of the healthy five subjects imaged at 4.7 T (Fig. 3.8).

3.5 Discussion

The two main advantages of the new background phase removal method over traditional phase filtering are improved visualization in areas affected by rapidly changing background fields and less phase suppression in deep grey matter structures for more

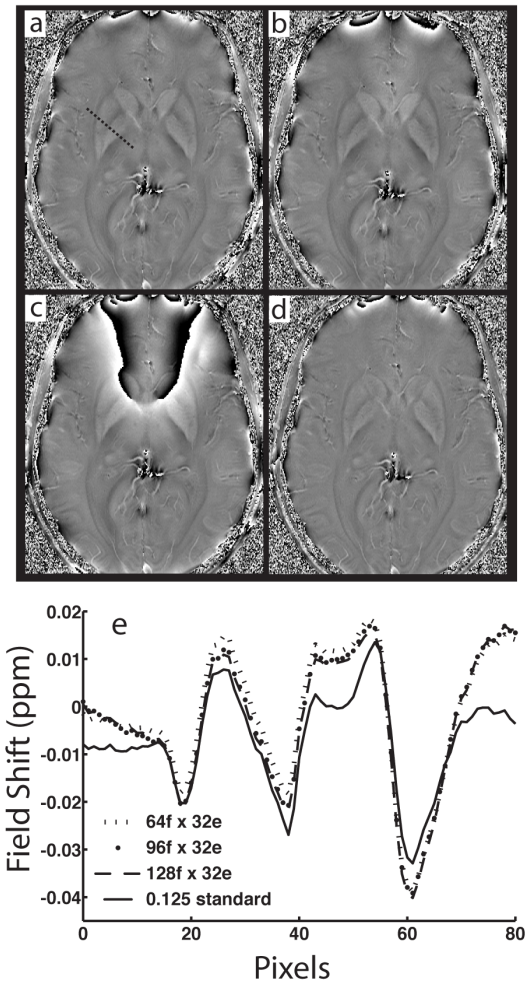

Figure 3.5: Axial image of deep grey matter structures at 3.0 T using the new gradient filtering method with 0.0625 filter strength and (a) 64f x 32e and (b) 128f x 32e square fitting and extraction window, respectively. Standard filtering with (c) 0.0625 filter strength and (d) 0.125 filter strength. e: Average profile through the center of the PUT and GP (dotted line in a) of five subjects using standard filter with 0.125 and new filtering methods with 64f x 32e 96f x 32e and 128f x 32e square fitting and extraction windows, respectively. The profile through the PUT and GP with standard filtering using 0.0625 filter strength is not shown in (e) because of visible phase wrapping. The images from 3.0 T use an inverted grey scale for profile comparison.

accurate quantitative phase analysis and higher contrast.

The new method has few assumptions in its implementation. Phase unwrapping is not required prior to background removal, which eliminates potential difficulties in unwrapping territories near high susceptibility regions for certain algorithms described by Witoszynskyj et al [23] and Zhou et al [29]. The moving window background phase estimation could be implemented with an advanced unwrapping algorithm such as PhiUn; however, areas of rapid phase change or noise could be

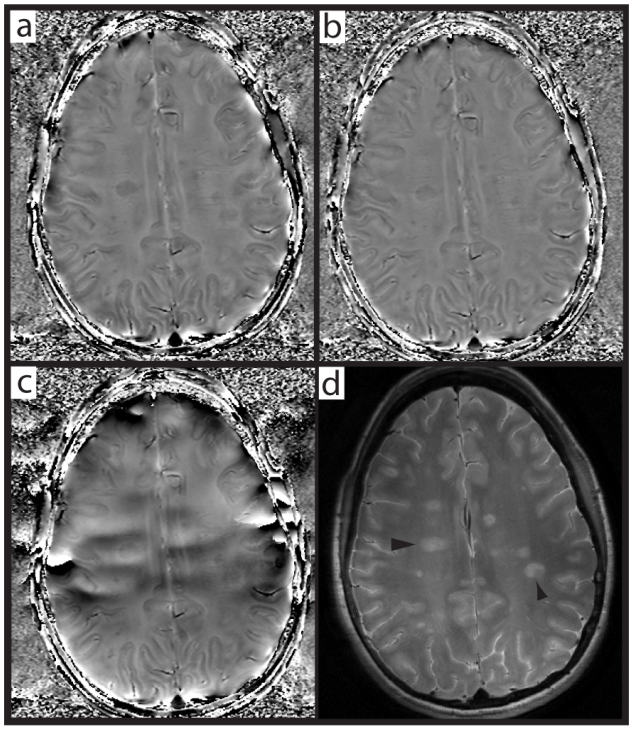

Figure 3.6: Axial images from a 29-year-old RRMS patient acquired at 4.7 T with (a) the new method using 64f x 32e square fitting and extraction window with 0.0625 filter strength, (b) standard method using 0.125 filter strength, (c) standard method using 0.0625 filter strength, and (d) T2-weighted FSE image identifying inflammatory lesion in MS. Arrowheads in (d) show example lesions used for phase contrast measures.

adversely affected. The gradient fitting method circumvents phase unwrapping by using the spatial gradient of the phase data to determine polynomial coefficients to the raw phase. This local smoothing allows implementation of a weaker standard high pass filter, which dramatically improves tissue contrast and visualization compared to standard filtering. A 0.0625 strength filter was used as the weakest filter in this study because areas with rapidly varying background phase were studied; however, smaller filter strengths could be implemented for even less phase suppression in areas with less significant background fields. As well, the 0.0625 filter closely approximated the ideal phase in simulation and there may be minimal benefit in applying a weaker filter than this. In addition, there is no need for tissue segmentation or masking as with other methods where an accurate brain volume must be delineated [6]. The gradient fitting moving window algorithm does not use masking, yet generally performs well at brain edges because the algorithm is designed so the fitting window should contain an adequate number of voxels for polynomial estimation. The final image consists of overlapping extraction windows, originating from a smaller central region within their respective fitting windows. If the fitting window

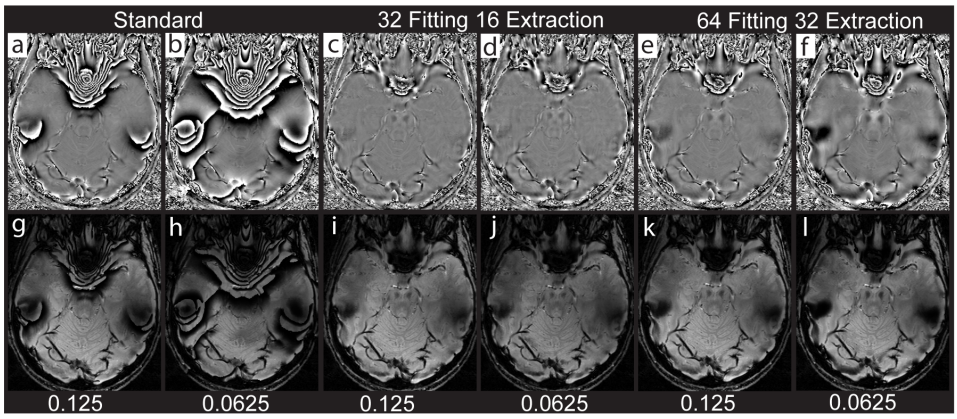

Figure 3.7: 4.7 T images from a 28-year-old volunteer, phase images (top) and SWI images (bottom) showing the midbrain with substantia nigra, left middle cerebral artery, and cerebellum. Standard filtering using (a,g) 0.125 filter strength and (b,h) 0.0625 filter strength. New background phase removal using 32f x 16e fitting and extraction window with (c,i) 0.125 filter strength and (d,j) 0.0625 filter strength. New background phase removal using 64f x 32e fitting and extraction window with (e,k) 0.125 filter strength and (f,l) 0.0625 filter strength.

is at the edge of brain tissue with some voxels containing brain and most containing air/skull, there must be a minimum of voxels which extend from the fitting window edge into the extraction window. If brain tissue only represents a few voxels near the edge of the fitting window alone, this will not be included in the extraction window and subsequently the final image. In addition, the edges of the extraction window are weighted less strongly with multiplication of a 2D Hanning window to negate effects of potentially poor background phase removal at brain edges. The method does not require a 3D volume but future implementations could utilize a 3D approach. Every iteration must estimate the local phase followed by Hanning filtering, causing total processing time to depend on the extraction window size and the time of these two operations. For one slice of a 512 x 512 matrix using an extraction window of 32, the algorithm took 33.5 seconds but an extraction window of 64 took 6.8 seconds on a computer with a 2.66 GHz corei7 processor.

Quantitative phase analysis with the new method compared to standard phase filtering show higher accuracy in simulation and provides more contrast in vivo using a low filter strength and a fitting window at least as large as the structure of interest. The standard filtering method has drawbacks with either strong or weak filter strengths. If the filter is strong enough to suppress background fields, the phase in the center of structures is suppressed, leading to less contrast and altered phase values [11]. Conversely, if the filter strength is weak, the background field may not be removed, confounding visualization of tissue. The new method addresses these conflicting issues apparent in standard filtering and closely approximates the phase

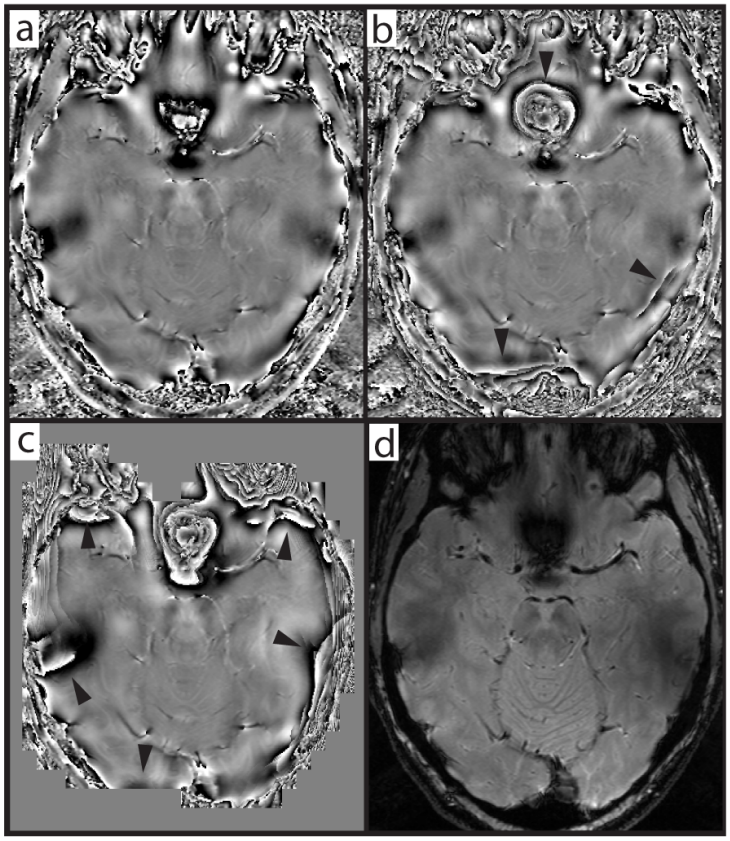

Figure 3.8: 4.7 T images from a 25-year-old volunteer. In each phase image (a-c), the background phase is locally estimated using a moving window third-order polynomial fit. The coefficients for this polynomial are determined using (a) a least-squares fit from the phase gradient data, (b) a direct polynomial fit using an unwrapped phase image with PhiUn, and (c) a direct polynomial fit using an unwrapped phase image with PRELUDE. The magnitude image is shown in (d). Arrowheads in (b,c) identify areas that were not properly unwrapped by PhiUn or PRELUDE but were correctly depicted with the gradient method. The filter width was 0.0625 and the fitting and extraction windows were 64f x 32e for ac.

profile of large structures while still removing the background phase in simulation provided an adequately sized fitting window. Although a range of fitting parameters were examined, different fitting window sizes produce similar results in vivo as most brain structures are relatively small compared to the whole image. Furthermore, the extraction window should be smaller than the fitting window for the best results to avoid spurious edge effects using a low-order polynomial fit. The caudate has much more contrast because traditional filtering often does not fully remove phase wraps within this structure which depresses phase values. The putamen has increased contrast with the new method, but it is not significantly different between methods because it contains high spatial frequencies with a strong slope in the phase profile (Fig. 3.5e).

Improved visualization of brain edges, structures, and lesions was demonstrated in simulation and in vivo. However, artifact is observed when the fitting window was smaller than the structure of interest because the polynomial is being fit to the structures, not primarily the background. This can be avoided with attention to the size of the fitting window assuring that it is larger than 32 for a 512 x 512 image matrix. The lesions examined represent a subset of lesions in MS, as some lesions appear either only in phase or T2-weighted images [26, 30]. With the new method, enhanced contrast and improved background removal in all brain areas could further delineate phase lesions. Other potential applications include investigating tissue or pathology near the brain edge such as subarachnoid hemorrhage [31], arteriovenous malformations [31], and cortical MS lesions [32]. The gradient fit method for determining a polynomial background approximation may have performed better than a direct fit using PRELUDE and PhiUn in areas containing substantial noise because the average phase gradient values over a whole fitting window still accurately estimates the background. If unwrapping fails to remove phase wraps, the background phase cannot be accurately fit using the described methods.

In conclusion, a new background phase removal method has been developed that uses the spatial gradient of the raw phase image to determine the coefficients for a low-order local polynomial fit without prior unwrapping. This allows the use of weaker filter strengths to optimize structure and lesion contrast and enables improved removal of background phase compared to the standard filtering method.

3.6 Acknowledgements

Contract grant sponsor: Natural Sciences and Engineering Research Council of Canada (NSERC); Contract grant sponsor: Canadian Institutes of Health Research (CIHR); Contract grant sponsor: Multiple Sclerosis Society of Canada; Contract grant sponsor: Vanier Canada Graduate Scholarship and an Alberta Innovates Health Solutions MD/PhD studentship (to A.J.W.).

Bibliography

[1] Duyn JH, van Gelderen P, Li TQ, de Zwart JA, Koretsky AP, Fukunaga M. High-field MRI of brain cortical substructure based on signal phase. Proc Natl Acad Sci U S A 2007;104(28):11796–801.

[2] He X, Yablonskiy DA. Biophysical mechanisms of phase contrast in gradient echo MRI. Proc Natl Acad Sci U S A 2009;106(32):13558–63.

[3] Ogg RJ, Langston JW, Haacke EM, Steen RG, Taylor JS. The correlation

between phase shifts in gradient-echo MR images and regional brain iron concentration. Magn Reson Imaging 1999;17(8):1141–8.

[4] Haacke EM, Xu Y, Cheng YC, Reichenbach JR. Susceptibility weighted imaging (SWI). Magnetic Resonance in Medicine 2004;52(3):612–8.

[5] Wharton S, Schafer A, Bowtell R. Susceptibility mapping in the human brain using threshold-based k-space division. Magnetic Resonance in Medicine 2010; 63(5):1292–304.

[6] Neelavalli J, Cheng YCN, Jiang J, Haacke EM. Removing Background Phase Variations in Susceptibility-Weighted Imaging Using a Fast, Forward-Field Calculation. Journal of Magnetic Resonance Imaging 2009;29(4):937–948.

[7] Hammond KE, Metcalf M, Carvajal L, Okuda DT, Srinivasan R, Vigneron D, Nelson SJ, Pelletier D. Quantitative In Vivo Magnetic Resonance Imaging of Multiple Sclerosis at 7 Tesla with Sensitivity to Iron. Annals of Neurology 2008; 64(6):707–713.

[8] Hopp K, Popescu BF, McCrea RP, Harder SL, Robinson CA, Haacke ME, Rajput AH, Rajput A, Nichol H. Brain iron detected by SWI high pass filtered phase calibrated with synchrotron X-ray fluorescence. Journal of Magnetic Resonance Imaging 2010;31(6):1346–54.

[9] Haacke EM, Ayaz M, Boikov AS, Kido DK, Kirsch WM. Imaging Cerebral Microbleeds Using Susceptibility Weighted Imaging: One Step Toward Detecting Vascular Dementia. Journal of Magnetic Resonance Imaging 2010;31(1):142–148.

[10] Wharton S, Bowtell R. Whole-brain susceptibility mapping at high field: a comparison of multiple- and single-orientation methods. Neuroimage 2010; 53(2):515–25.

[11] Walsh AJ, Wilman AH. Susceptibility phase imaging with comparison to R2 mapping of iron-rich deep grey matter. Neuroimage 2011;57(2):452–61.

[12] Denk C, Rauscher A. Susceptibility weighted imaging with multiple echoes. J Magn Reson Imaging 2010;31(1):185–91.

[13] McPhee KC, Denk C, Al Rekabi Z, Rauscher A. Bilateral filtering of magnetic resonance phase images. Magnetic resonance imaging 2011;.

[14] Ng A, Johnston L, Chen Z, Cho ZH, Zhang J, Egan G. Spatially dependent filtering for removing phase distortions at the cortical surface. Magnetic resonance in medicine 2011;66(3):spcone.

[15] Tong KA, Ashwal S, Obenaus A, Nickerson JP, Kido D, Haacke EM. Susceptibility-weighted MR imaging: a review of clinical applications in children. AJNR American journal of neuroradiology 2008;29(1):9–17.

[16] Schweser F, Deistung A, Lehr BW, Reichenbach JR. Quantitative imaging of intrinsic magnetic tissue properties using MRI signal phase: An approach to in vivo brain iron metabolism? Neuroimage 2011;54(4):2789–2807.

[17] Liu T, Khalidov I, de Rochefort L, Spincemaille P, Liu J, Tsiouris AJ, Wang Y. A novel background field removal method for MRI using projection onto dipole fields (PDF). NMR in biomedicine 2011;24(9):1129–36.

[18] Yao B, Li TQ, Gelderen P, Shmueli K, de Zwart JA, Duyn JH. Susceptibility contrast in high field MRI of human brain as a function of tissue iron content. Neuroimage 2009;44(4):1259–66.

[19] Meyers S, Eissa A, Wilman AH. Advantages of a Local Polynomial Filter with Moving Window for Phase Reconstruction in Susceptibility-Weighted Imaging. International Society of Magnetic resonance in medicine18th Annual meeting. Stockholm, Sweden, 2010; (abstract 4991).

[20] Bagher-Ebadian H, Jiang Q, Ewing JR. A modified Fourier-based phase unwrapping algorithm with an application to MRI venography. Journal of magnetic resonance imaging 2008;27(3):649–52.

[21] Rauscher A, Barth M, Reichenbach JR, Stollberger R, Moser E. Automated unwrapping of MR phase images applied to BOLD MR-venography at 3 Tesla. Journal of Magnetic Resonance Imaging 2003;18(2):175–80.

[22] Langley J, Zhao Q. Unwrapping magnetic resonance phase maps with Chebyshev polynomials. Magnetic resonance imaging 2009;27(9):1293–301.

[23] Witoszynskyj S, Rauscher A, Reichenbach JR, Barth M. Phase unwrapping of MR images using Phi UN–a fast and robust region growing algorithm. Medical image analysis 2009;13(2):257–68.

[24] Wang Y, Yu Y, Li D, Bae KT, Brown JJ, Lin W, Haacke EM. Artery and vein separation using susceptibility-dependent phase in contrast-enhanced MRA. Journal of Magnetic Resonance Imaging 2000;12(5):661–670.

[25] Haacke EM, Ayaz M, Khan A, Manova ES, Krishnamurthy B, Gollapalli L, Ciulla C, Kim I, Petersen F, Kirsch W. Establishing a baseline phase behavior in magnetic resonance imaging to determine normal vs. abnormal iron content in the brain. Journal of Magnetic Resonance Imaging 2007;26(2):256–264.

[26] Haacke EM, Makki M, Ge YL, Maheshwari M, Sehgal V, Hu JN, Selvan M, Wu Z, Latif Z, Xuan Y, Khan O, Garbern J, Grossman RI. Characterizing Iron Deposition in Multiple Sclerosis Lesions Using Susceptibility Weighted Imaging. Journal of Magnetic Resonance Imaging 2009;29(3):537–544.

[27] Sedlacik J, Kutschbach C, Rauscher A, Deistung A, Reichenbach JR. Investigation of the influence of carbon dioxide concentrations on cerebral physiology by susceptibility-weighted magnetic resonance imaging (SWI). Neuroimage 2008; 43(1):36–43.

[28] Jenkinson M. Fast, automated, N-dimensional phase-unwrapping algorithm. Magnetic resonance in medicine 2003;49(1):193–7.

[29] Zhou K, Zaitsev M, Bao S. Reliable two-dimensional phase unwrapping method using region growing and local linear estimation. Magnetic resonance in medicine 2009;62(4):1085–90.

[30] Eissa A, Lebel RM, Korzan JR, Zavodni AE, Warren KG, Catz I, Emery DJ, Wilman AH. Detecting lesions in multiple sclerosis at 4.7 tesla using phase susceptibility-weighting and T2-weighting. J Magn Reson Imaging 2009; 30(4):737–42.

[31] Kudo K, Fujima N, Terae S, Hida K, Ishizaka K, Zaitsu Y, Asano T, Yoshida D, Tha KK, Haacke EM, Sasaki M, Shirato H. Spinal Arteriovenous Malformation: Evaluation of Change in Venous Oxygenation with Susceptibility-weighted MR Imaging after Treatment. Radiology 2010;254(3):891–899.

[32] Calabrese M, Filippi M, Rovaris M, Mattisi I, Bernardi V, Atzori M, Favaretto A, Barachino L, Rinaldi L, Romualdi C, Perini P, Gallo P. Morphology and evolution of cortical lesions in multiple sclerosis. A longitudinal MRI study. Neuroimage 2008;42(4):1324–8.

Chapter 4

Multiple Sclerosis: Validation of MR Imaging for Quantification and Detection of Iron [1]

4.1 Abstract

Purpose: To investigate the relationship between iron staining and magnetic resonance (MR) imaging measurements in postmortem subjects with multiple sclerosis (MS).

Materials and Methods: Institutional ethical approval was obtained, and informed consent was obtained from the subjects and/or their families. Four MR imaging methods based on transverse relaxation (T_2 weighting, R_2 mapping, and $R_2^\star$ mapping) and phase imaging were performed by using a 4.7-T system in three in situ postmortem patients with MS less than 28 hours after death and in one in vivo patient 1 year before death. Iron staining with the Perls iron reaction was performed after brain extraction. Region-of-interest measurements from six subcortical grey matter structures were obtained from MR imaging and then correlated with corresponding locations on photographs of iron-stained pathologic slices by using a separate linear least-squares regression in each subject. Iron status of white matter lesions, as determined by staining, was compared with appearance on MR images.

Results: $R_2^\star$ mapping had the highest intrasubject correlations with iron in subcortical grey matter ($R^2 = 0.857$, 0.628, and 0.685; all $P < .001$), while R_2 mapping ($R^2 = 0.807$, 0.615, 0.628, and 0.489; $P < .001$ and $P = .001$, .034, and .001, re-

[1] A version of this section has been published. Andrew J. Walsh, BSc, R. Marc Lebel, PhD, Amir Eissa, PhD, Gregg Blevins, MD, Ingrid Catz, MSc, Jian-Qiang Lu, MD, Lothar Resch, MD, Edward S. Johnson, MD, Derek J. Emery, MD, Kenneth G. Warren, MD and Alan H. Wilman, PhD. Multiple Sclerosis: Validation of MR Imaging for Quantification and Detection of Iron. Radiology (Published online before print January 7, 2013, doi:10.1148/radiol.12120863)

spectively), phase imaging (R^2 = 0.672, 0.441, 0.596, 0.548; all P $\leq$ .001), and T_2-weighted imaging (R^2 = 0.463, 0.582, 0.650, and 0.551; all P < .001) had lower but still strong correlations. Within lesions, hypointense areas on phase images did not always represent iron. A hyperintense rim surrounding lesions on $R_2^\star$ maps was only present with iron staining, yet not all iron-staining lesions had $R_2^\star$ rim hyperintensity.

Conclusion: All four MR imaging methods had significant linear correlations with iron and could potentially be used to determine iron status of subcortical grey matter structures in MS, with $R_2^\star$ mapping being preferred. A reliable method of determining iron status within MS lesions was not established.

4.2 Introduction

Iron has an important physiologic role in the brain, including involvement in myelin synthesis, neurotransmitter production, and oxygen transport [1]. In multiple sclerosis (MS), iron is reportedly increased in subcortical grey matter and present in some lesions at histologic analysis [2, 3, 4]. Magnetic resonance (MR) imaging offers a number of methods that are sensitive to brain iron, including T_2-weighted fast spin-echo (SE) imaging [5], T_2^*-weighted gradient-echo imaging [6], mapping of the SE and gradient-echo transverse relaxation rates (R_2 and R_2^*, respectively) [7], phase imaging [8], and susceptibility mapping [9]. These methods provide enhanced iron sensitivity at higher magnetic field strengths [7, 10]. Several MR imaging methods have shown a relationship between subcortical grey matter measures and functional scores in patients with MS [11, 12, 13]; however, the contribution from iron to the quantitative MR imaging measures is unclear, and image contrast could be derived from other sources, such as macromolecules [14] and protein and lipid orientation [15]. Researchers in many studies [14, 16, 17, 18] have examined the relationship between quantitative MR imaging measurements and predicted brain iron content determined from referenced healthy brain iron values, typically by using the 1958 work of Hallgren and Sourander [19]; however, no reference exists for brains with pathologic changes. Postmortem studies are required to determine the relationship between MR imaging measures and actual iron levels in patients with MS.

Few postmortem studies have evaluated the accuracy of quantitative MR imaging methods for measuring brain iron in healthy individuals or in patients with other non-MS diseases. The results of these studies demonstrate that phase [20] and R_2 and R_2^* [21] have a high correlation to iron in these subjects. However, these results cannot be directly translated into evaluating iron in patients with MS because each MR imaging method is variably influenced by different pathologic processes, such as demyelination, cellular infiltration, and edema. Furthermore, most postmortem

MR imaging studies that have investigated the relationship between MR imaging and iron have used formalin-fixed tissue [20, 22, 23, 24]. Formalin fixation can alter relaxation properties and, to a lesser extent, the iron content of tissue [25, 26, 27, 28, 29]. Early in situ postmortem imaging closely resembles in vivo imaging because the brain is surrounded by cerebrospinal fluid, and air-tissue interfaces are intact to cause susceptibility effects that are an important feature in R_2^* mapping and phase imaging.

In our study, four iron-sensitive methods were evaluated for brain iron detection in patients with MS. In vivo and in situ postmortem MR imaging was followed by Perls iron staining, which enables correlation analysis between MR imaging and iron staining measures in subcortical grey matter and MR imaging detection of iron presence within lesions. Since the imaging parameters are suitable for in vivo acquisition, postmortem results are directly translatable to in vivo human applications. Therefore, the purpose of our work was to investigate the postmortem relationship between iron staining and MR imaging measurements in subjects with MS.

4.3 Materials and Methods

4.3.1 Subjects

Four deceased subjects with MS were included in our prospective study between April 1, 2009, and September 13, 2011. Institutional ethical approval was obtained, as was informed consent from the subjects and/or their families. Three subjects with secondary progressive MS underwent postmortem in situ MR imaging shortly after death. Subject 1 was a 63-year-old man who had longstanding type 2 diabetes with neuropathologic evidence of hyalinized vessels, which is consistent with this disease. This subject died of cardiorespiratory failure due to a combination of aspiration pneumonia and septicemia from pyelonephritis and was imaged 28 hours after death. Subject 2 was a 55-year-old woman who had a history of chronic obstructive pulmonary disease and generalized anxiety disorder. This subject died of aspiration pneumonia and was imaged 6 hours after death. Subject 3 was a 60-year-old man who had longstanding chronic obstructive pulmonary disease, longstanding congestive heart failure, and metastatic prostate cancer. This subject died of Staphylococcus aureus septicemia due to pneumonia secondary to prostate cancer lung metastasis and was imaged 7 hours after death. Subject 4 had relapsing-remitting MS with no other longstanding medical conditions. This subject underwent in vivo imaging 1 year before death at the age of 45 years and died of medullary compression due to a B-cell lymphoma tumor in the cerebellum. In all subjects, the clinical diagnosis of MS was made by neurologists who specialize in MS (K.G.W. and G.B., with 38 and 6 years experience, respectively) and was pathologically confirmed by three

neuropathologists (E.S.J., J.Q.L., and L.R., with 34, 5, and 30 years experience, respectively).

4.3.2 MR Image Acquisition

MR imaging data were acquired by using a 4.7-T whole-body imaging system (Varian Unity Inova, Palo Alto, Calif). The imaging protocol consisted of four axial MR imaging methods that took a total time of 39 minutes: standard T_2-weighted fast SE (6.8 minutes) [30], $R_2^\star$ mapping (8.9 minutes), R_2 mapping (15.6 minutes) [31], and phase imaging (6.6 minutes). Subject 2 did not undergo imaging with the $R_2^\star$ mapping sequence.

Axial two-dimensional T_2-weighted fast SE MR imaging was acquired with 80-mm superior-inferior coverage centered on the thalamus with slightly different parameters between subjects. Typical parameters were: repetition time msec/echo time msec, 7000-14 000/30-50; echo train length, four to eight; 40-80 contiguous sections; section thickness, 1-2 mm; field of view, 256 x 192.5 mm; matrix, 1024 x 385 with 75% partial Fourier; voxel size, 0.25 x 0.25 x 1-2 mm. This echo time provided substantial T_2-weighting for iron-containing deep grey matter at 4.7 T [12].

Axial three-dimensional $R_2^\star$ mapping was acquired with full brain coverage (160 mm) by using the following parameters: repetition time, 44 msec; 10 echoes with 4.0-4.2 msec echo spacing; first echo, 2.9-3.2 msec; flip angle, 11; field of view, 256 x 128-160 x 160 mm; matrix, 512 x 160 x 80; voxel size, 1 x 0.8-1 x 2 mm.

Axial two-dimensional R_2 mapping with a multiecho SE was acquired by using the following parameters: repetition time, 3500 msec; 18 - 24 echoes with 10-msec echo spacing; first echo, 10 msec; two sections, section thickness, 4-5 mm; section gap, 8 -10 mm, field of view, 256 x 181 mm; matrix, 512 x 145 -171; voxel size, 0.8-1 x 1 x 4-5 mm. The section thickness of the 180° refocusing pulses was 1.75 times wider than that of the excitation pulse. In vivo specific absorption rate standards allowed only two sections of R_2 mapping to be collected over a 5.2-minute acquisition owing to the high magnetic field and the large number of 180° pulses. The sequence was implemented multiple times to acquire data between interleaved sections. Three acquisitions were performed in subjects 1 and 4, two were performed in subject 2, and one was performed in subject 3.

Axial phase imaging used a two-dimensional single gradient echo with first-order flow compensation acquired with the following parameters: repetition time/echo time msec, 1540/7-15; 50 contiguous sections; section thickness, 2 mm; flip angle, 70°; field of view, 214-256 x 163-192 mm; matrix, 512 x 256-392; voxel size, 0.42-0.5 x 0.42-0.5 x 2 mm.

Images were acquired with a standard birdcage head coil for transmission and a tight-fitting four-element array coil for signal reception. In subject 1, the head coil

was also used for reception owing to large head size.

4.3.3 Pathology Examination

The brains were fixed in 18% formalin, sectioned into 8-mm slices, and photographed before iron staining. Coronal cuts were used based on neuropathology preference, except in subject 1, in whom slices were cut axially. Slices containing subcortical grey matter and/or lesions were stained by using the Perls iron reaction[32]. The slices were placed in a plastic container with 1 L of 2% hydrochloric acid combined with 1 L of 2% potassium ferrocyanide for 30 minutes. After washing for 2 minutes with water, the slices were photographed again.

The photographs were converted to greyscale by using software (ImageJ [33]) and manually rotated, resized, and translated to align the photographs of stained and unstained brain slices. The window and level were normalized on the basis of the intensity of the static background outside of the brain and the intensity of white matter with little staining within the brain slice. Regions of interest (ROIs) were drawn around iron-rich subcortical grey matter structures, and the differences between structures on stained versus unstained photographs were calculated. The results were divided by the difference between the background and the healthy-appearing white matter, generating a relative optical density where a higher optical density corresponds relatively to more iron staining within one subject. This method is similar to that used in a previous quantitative iron validation study [34] with MR imaging using optical density measures. Lesions were visually examined for iron staining and confirmed as MS lesions with microscopic examination by pathologists (E.S.J. and J.Q.L.) with 100% interobserver reliability.

4.3.4 MR Image Processing

All MR images were interpolated to isotropic 0.25-mm resolution and manually registered, on the basis of gyri contours and subcortical grey matter structures, to the pathologic photographs by using affine transformations. With software (ImageJ), ROIs were drawn around the borders of corresponding subcortical grey matter structures after registration with the pathologic photographs to obtain proper anatomic correspondence. This enabled an accurate spatial comparison of the reformatted axial MR images to the coronal gross pathologic slices for subjects 2, 3, and 4. ROIs were based on the T_2-weighted fast SE MR images and the $R_2^\star$ maps and then transferred to the other images. The structures evaluated included the caudate nucleus, putamen, globus pallidus, substantia nigra, red nucleus, thalamus, and subthalamic nucleus.

Large spatial signal intensity variations on the T_2-weighted fast SE MR images, arising from high-field-strength radiofrequency transmittance interference effects [35]

and receiver coil variation, were corrected by using a three-dimensional Gaussian blur with a radius of 64 mm. Measured values were divided by the intensity of cerebrospinal fluid averaged between the right and left lateral ventricles.

$R_2^\star$ maps were produced by using a weighted least-squares monoexponential fit of the 10 echoes [36]. Prior to fitting, a linear field-gradient correction algorithm was applied to recover signal losses from air-tissue interfaces that were in close proximity to relevant subcortical grey matter structures [37]. Weighting factors for the least-squares fitting were given by the intensity scaling factors needed to compensate for signal loss and accounted for amplified noise during the fitting procedure.

R_2 maps were produced by using a least-squares fit with stimulated echo compensation [31], which accounted for the exact signal decay that arose from radiofrequency transmittance variation across the section profile and in-plane variation from high-field-strength radiofrequency interference effects.

Phase images were processed with the standard Hanning filter method [38] by using a filter width of 0.125. The filter width is the ratio of the Hanning filter divided by the total matrix size along one dimension [39, 40]. The phase images were separately processed with a moving window gradient fitting method [40] with a filter width of 0.0625. To mitigate effects of nonlocal external field effects from iron-rich structures, reference phase measures were obtained in nearby healthy-appearing white matter greater than 10 mm from each structure and separately obtained directly adjacent to each structure [40].

4.3.5 MR Imaging Lesion Evaluation

MR imaging lesion contrast was compared between iron-staining and noniron-staining lesions by a neuroradiologist (D.J.E., with 15 years experience) and a neuropathologist (E.S.J.). Intensity was examined both within lesions and around the periphery (rim) by using phase images, $R_2^\star$ maps, and T_2-weighted fast SE MR images. R_2 mapping was not used owing to limited coverage. Lesions in subject 4 were not evaluated because of potential variability in lesion activity over 1 year.

4.3.6 Statistical Analysis

Statistical analysis was performed by using software (SPSS, version 18.0 for Macintosh; IBM, Armonk, NY). Correlations between iron-staining optical densities and individual MR imaging measures were tested by using a separate linear regression model in each subject. More than one measurement from a single structure was sometimes obtained owing to the number of slices through that structure at pathologic sectioning. P values less than .05 were considered to indicate a significant difference.

4.4 Results

4.4.1 Subcortical Grey Matter Measurements

All MR imaging measures showed a significant correlation to iron detected with Perls iron staining (Table 4.1; Figs 4.1, 4.2). $R_2^\star$ measurements had the strongest correlations to optical density in each subject ($R^2 = 0.857$, 0.628, and 0.685; all $P < .001$). R_2 mapping ($R^2 = 0.807$, 0.615, 0.628, and 0.489; $P < .001$ and $P = .001$, .034, and .001, respectively), phase imaging ($R^2 = 0.672$, 0.441, 0.596, and 0.548; all $P \leq .001$), and T_2-weighted fast SE MR imaging ($R^2 = 0.463$, 0.582, 0.650, and 0.511; all $P < .001$) had comparable correlations to optical density. A somewhat weaker correlation was evident between the T_2-weighted fast SE MR measures and iron in subject 4 (Table 4.1, Fig 4.2) while the other MR imaging measures had substantially higher correlations to postmortem staining. Although most subcortical grey matter structures were imaged with the R_2 mapping sequence, this regression contained fewer ROIs because the exact anatomic correspondence to pathologic slices was not achieved in all regions owing to section gaps in some subjects.

Table 4.1: Correlations between Quantitative MR Imaging Measures and Optical Densities

	$R_2^\star$ map		R_2 map		T_2-weighted Fast SE MR Imaging		Phase MR Imaging		No. of ROIs	
Subject	R^2	P Value	R^2	P Value	R^2	P Value	R^2	P Value	$R_2^\star$, T_2 - weighted Fast SE, and Phase	R_2
1	0.685	<.001	0.489	0.001	0.511	<.001	0.548	<.001	22	18
2	ND	ND	0.628	0.034	0.650	<.001	0.596	<.001	15	7
3	0.628	<.001	0.615	0.001	0.582	<.001	0.441	<.001	27	15
4[a]	0.857	<.001	0.807	0.001	0.463	<.001	0.672	<.001	32	27

Note. - ND = no data.
[a]Analyzed with a repeated measures t-test.

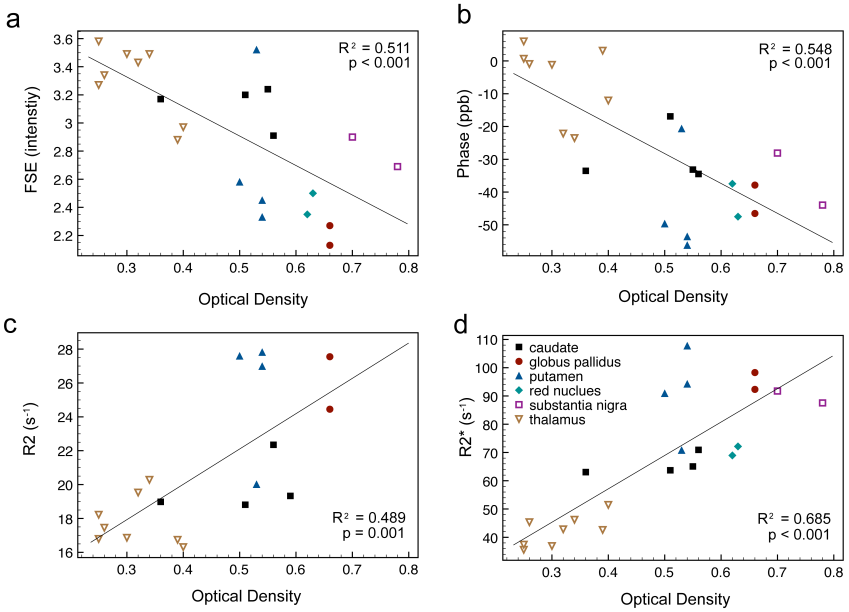

Figure 4.1: Scatterplots show correlations between optical density from iron staining and in situ postmortem (a) fast SE (FSE), (b) phase, (c) R_2, and (d) $R_2^\star$ MR imaging in subject 1. Key for all plots appears on d. Caudate = caudate nucleus, ppb = parts per billion, s = seconds.

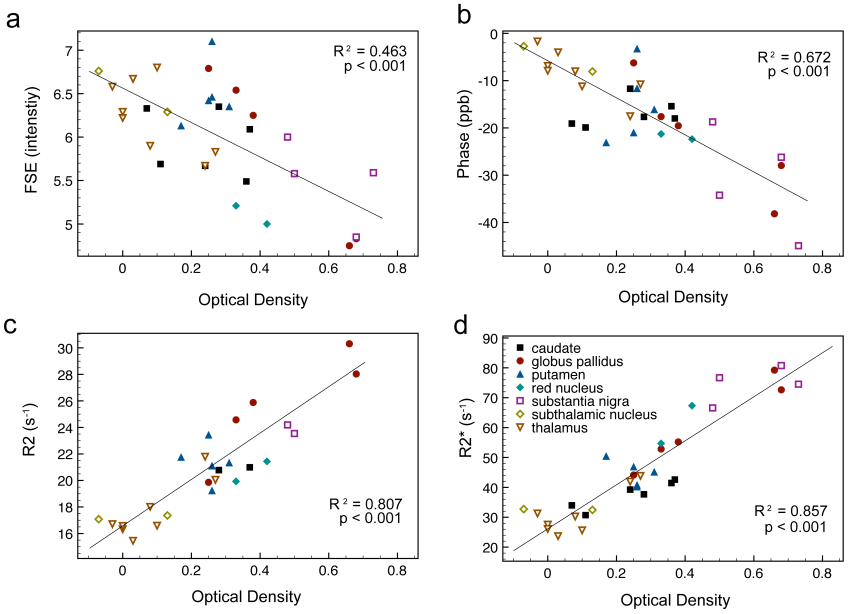

Figure 4.2: Scatterplots show correlation between optical density from iron staining and in vivo (a) fast SE (FSE), (b) phase, (c) R_2, and (d) $R_2^\star$ MR imaging in subject 4. Iron staining was performed 1 year after MR imaging, immediately following death. Key for all plots appears on d. Caudate = caudate nucleus, ppb = parts per billion, s = seconds.

Table 4.2: Correlations between phase MRI and optical densities

	Hanning Standard Filtering				Gradient Fitting					
	White Matter Reference		Adjacent Reference		White Matter Reference		Adjacent Reference		No. of ROIs	
Subject	R^2	P Value	R^2	P Value	R^2	P Value	R^2	P Value	Standard Filtering	Gradient Fitting
1	0.217	0.069	0.0507	0.002	0.012	0.626	0.548	<.001	16	22
2	0.287	0.040	0.255	0.114	0.142	0.167	0.596	.001	15	15
3	0.059	0.233	< 0.001	0.973	0.011	0.609	0.441	<.001	27	27
4[a]	0.212	0.008	0.118	0.056	0.004	0.738	0.672	<.001	32	32

Note.White matter reference = healthy-appearing white matter at least 10 mm from the structure border, lateral to all structures. Adjacent reference = white matter directly adjacent to the structural border, medial to the globus pallidus and lateral to all other structures.
[a]Analyzed with a repeated measures t-test.

The phase analysis methods demonstrated different correlations to iron staining (Table 4.2) and depended strongly on the location of the reference phase measurements. The gradient fitting background removal method with an adjacent reference phase demonstrated the highest correlation to optical density and was the only phase method which demonstrated significant results for all subjects.

4.4.2 Visual Analysis of Subcortical grey Matter

Hyperintense regions on the $R_2^\star$ and R_2 maps and hypointense regions on T_2-weighted fast SE MR images corresponded well to staining of subcortical grey matter with Perls iron stain on photographs (Fig 4.3a, 4.3b). Postmortem MR imaging depicted similar contrast to in vivo results (Fig 4.4.)

The gradient phase removal method produced more contrast in large subcortical grey matter structures, such as the head of the caudate nucleus, putamen, and globus pallidus, compared with the Hanning processing method (Fig 4.3c). The Hanning method does not completely remove phase wraps from structures of interest, eliminating quantitative measures in these regions. Within structures, there is some disparity compared with staining and other MR imaging methods with both Hanning and gradient phase methods (Fig 4.3).

4.4.3 Visual Analysis of MS Lesions

When using T_2-weighted fast SE MR images, phase images, and $R_2^\star$ maps, general trends appear when classifying lesions on the basis of iron staining (Table 4.3). However, convincing evidence for the ability of individual MR imaging methods to be used to determine the iron status of lesions was not established.

Sixteen lesions, both staining and nonstaining, were seen on pathologic samples from subject 1 (Fig 4.5). Three lesions could not be analyzed because of partial volume effects on MR images from the lateral ventricles. On $R_2^\star$ maps, hyperintense rims were only present in iron-staining lesions, while on phase images, hypointense rims were generally, but not exclusively, present in iron-staining lesions. Generally, lesions that stained for iron were centrally isointense or not as hypointense on $R_2^\star$ maps as compared with lesions that did not stain. Also, iron-staining lesions often appeared more hypointense centrally on phase images compared with nonstaining lesions; however, some hypointense lesions did not contain iron. All lesions in this subject were hyperintense on T_2-weighted fast SE MR images.

Subject 2 had 11 regions that contained large chronic plaques, which demonstrated variable staining for iron. Primarily, staining was observed around the periphery (rim) of the plaques, with diffuse patchy staining throughout the lesions. On T_2-weighted fast SE MR images, all lesions appeared hyperintense. On phase images, the centers of large lesions appeared primarily isointense or hypointense,

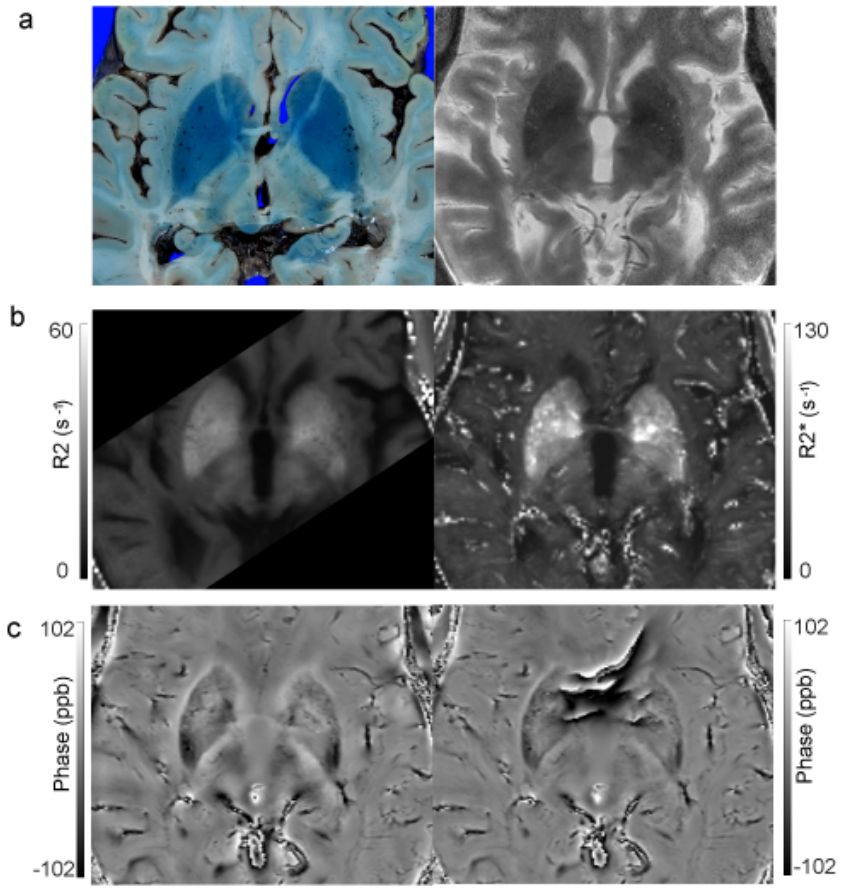

Figure 4.3: In situ postmortem MR images and photographs of pathology samples from subject 1. (a) Corresponding pathology sample (left) stained with Perls iron stain and T_2-weighted fast SE MR image (right). (b) Corresponding R_2 map with six two-dimensional sections (left), which have less coverage than other MR imaging acquisitions, and $R_2^\star$ map (right). (c) Corresponding phase images processed with gradient fitting (left) and Hanning (right) methods. Phase wraps were not removed, and contrast within structures was reduced owing to a higher filter width. ppb = parts per billion, s = seconds.

while the rims appeared variably hypointense. This did not correspond absolutely to the staining.

Subject 3 had six lesions that demonstrated microscopic evidence of remyelination and were considered to be shadow plaques (Fig 4.6). Only one lesion was readily identified at macroscopic visual inspection, and all lesions failed to stain for iron. All lesions were hypointense on $R_2^\star$ maps, hyperintense on T_2-weighted fast SE MR images, and isointense on phase images.

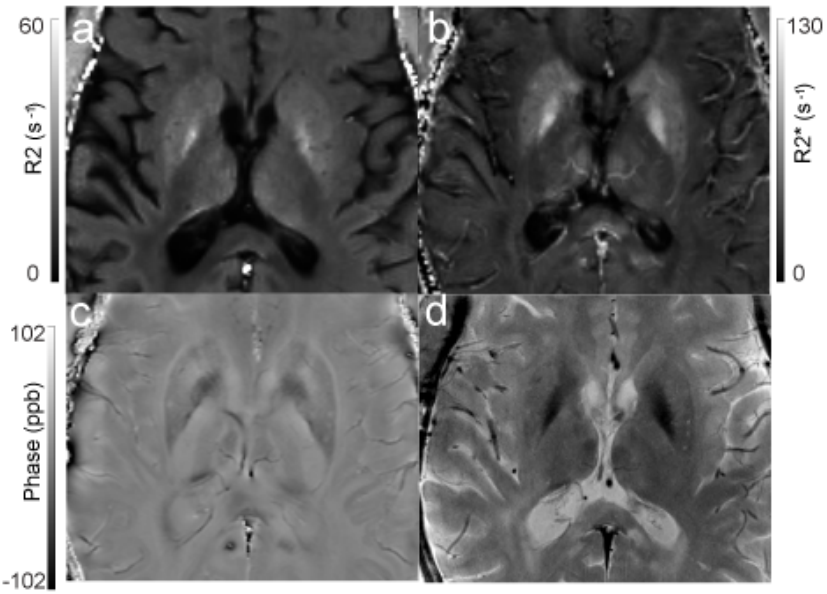

Figure 4.4: In vivo (a) R_2, (b) $R_2^\star$, (c) phase with gradient background removal, and (d) T_2-weighted fast SE MR images from subject 4. Note that vessels are less pronounced on b and c, acquired in vivo versus postmortem (Fig 4.3). ppb = parts per billion, s = seconds.

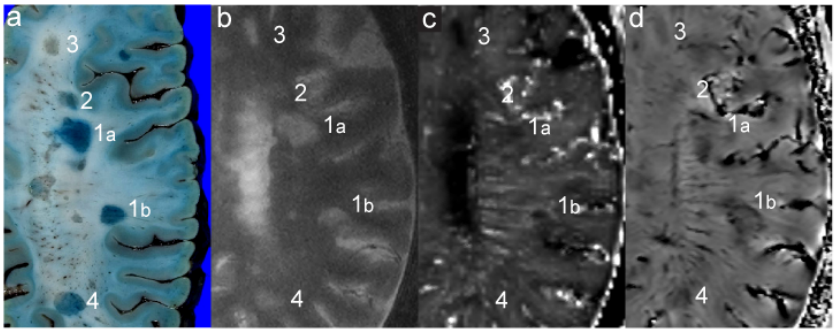

Figure 4.5: (a) Pathology specimen and (b-d) in situ postmortem MR images from subject 1. (a) Perls iron-stained 8-mm-thick axial cerebral slice superior to the left lateral ventricle with staining (1a, 1b, 2, 4) and nonstaining (3) lesions. (b) T_2-weighted fast SE MR image with focal hyperintensities corresponding to both staining and nonstaining lesions. (c) $R_2^\star$ map shows two centrally hypointense lesions with hyperintense rims (1a, 1b), an isointense lesion (2), and a hypointense lesion (4), which all correspond to staining lesions. Hypointense lesion (3) corresponds to nonstaining lesion. (d) Phase image processed with gradient method shows hypointensity in both staining and nonstaining lesions. Partial volume effects are visible from the superior aspect of the left lateral ventricle on b-d.

Table 4.3: Perls Iron Staining of Lesions Compared with MR Imaging Intensity

		Phase		$R_2^\star$	
Lesion	Iron Staining	Center	Rim	Center	Rim
		Subject 1			
1	Complete	Heterogeneous	Hypointense	Heterogeneous	Hyperintense
2	Complete	Hypointense	Isointense	Isointense	Hyperintense
3	Complete	Heterogeneous	Isointense	Hypointense	Hyperintense
4	Complete	Hypointense	Isointense	Isointense	Isointense
5	Complete	Hypointense	Isointense	Hypointense	Isointense
6	None	Hypointense	Isointense	Hypointense	Isointense
7	None	Hypointense	Isointense	Hypointense	Isointense
8	Complete	Hypointense	Isointense	Hypointense	Hyperintense
9	None	Hypointense	Isointense	Hypointense	Isointense
10	None	Hypointense	Hypointense	Hypointense	Isointense
11	Complete	Hypointense	Isointense	Heterogeneous	Isointense
12	None	Hypointense	Hypointense	Hypointense	Isointense
13	None	Hypointense	Isointense	Hypointense	Isointense
		Subject 2			
1	Rim	Isointense	Hypointense	No data	No data
2	Complete	Hypointense	Isointense	No data	No data
3	Rim	Isointense	Isointense	No data	No data
4	Rim	Isointense	Hypointense	No data	No data
5	Rim	Isointense	Hypointense	No data	No data
6	Rim	Isointense	Hypointense	No data	No data
7	Rim	Isointense	Heterogeneous	No data	No data
8	Rim	Isointense	Hypointense	No data	No data
9	Rim	Isointense	Hypointense	No data	No data
10	Rim	Isointense	Hypointense	No data	No data
11	Rim	Isointense	Hypointense	No data	No data
		Subject 3			
1	None	Isointense	Isointense	Hypointense	Isointense
2	None	Isointense	Isointense	Hypointense	Isointense
3	None	Isointense	Isointense	Hypointense	Isointense
4	None	Isointense	Isointense	Hypointense	Isointense
5	None	Isointense	Isointense	Hypointense	Isointense
6	None	Isointense	Isointense	Hypointense	Isointense

Note. - Intensities given are compared with adjacent tissue. Center = MR lesion intensity excluding periphery, Rim = MR intensity of lesion periphery.

4.5 Discussion

Our study evaluated several MR imaging methods for measuring iron in subcortical grey matter and for detecting iron within and surrounding MS lesions. $R_2^\star$ mapping had the highest correlation with iron staining in subcortical grey matter in each individual postmortem subject. R_2 mapping, phase imaging, and T_2-weighted fast SE MR appear to have comparable correlations with iron staining, which are moderate to strong. A weaker correlation with phase imaging may have been due to phase contrast dependence on structural shape and not exclusively iron content [39]. T_2-

weighted fast SE MR imaging may have had a weaker correlation because at high field strength, radiofrequency interference produces a spatial variation of flip angles. R_2 mapping may have had a weaker correlation because fewer measurements were obtained due to limited section coverage.

Compared with the subjects imaged postmortem, the subject imaged in vivo had substantially higher correlations to iron staining with $R_2^\star$ mapping, R_2 mapping, and phase imaging, but a similar correlation with T_2-weighted fast SE MR imaging. Anecdotal intersubject comparison was hampered by differences in disease manifestation, blood flow, and oxygenation and, for T_2-weighted fast SE MR imaging, by the fact that the transmit radiofrequency field may vary substantially between individuals at high field strength.

Previous studies have evaluated the correlation between MR imaging and quantitative iron measures, although not in MS. A study [21] similar to our own that focused on healthy individuals yielded higher correlations than we obtained for $R_2^\star$ and similar correlations for R_2 by using a quantitative spectroscopic method to provide total iron in limited sample volumes. In addition, an evaluation [15] of one patient with Alzheimer disease yielded a higher correlation for phase imaging by using x-ray fluorescence mapping for iron. These previous works detected total iron, but the MR imaging measures were mainly sensitive to ferric paramagnetic iron. In our study, Perls iron stain was used to provide a complete slice depiction of ferric iron variation. Although Perls iron staining is generally considered to be qualitative, results of one study [41] demonstrated strong correlations ($r = 0.945$) between quantitative chemical iron measures and similar optical density measures. In MS, macromolecular mass fraction could be altered as proteins or lipids are degraded or synthesized in response to disease activity, which can alter quantitative MR imaging values [14] without influencing iron staining. Also, prominent features of MS, such as inflammation, neuronal degeneration, demyelination, and cellular swelling, can affect each MR imaging method, but primarily T_2-weighted fast SE MR and R_2 imaging. These factors limit the ability to compare between cases. Furthermore, correlations may be different because whole-structure ROIs were used, similar to widely used in vivo analysis [16, 18, 42, 43], as opposed to multiple small territories within structures.

In MS lesions in our current study, a single MR imaging method alone could not adequately determine the presence of iron. This is contradictory to results of a previous study [44], which indicated that iron is the dominant source of phase contrast in MS lesions. The pathophysiology of lesions can involve several simultaneous processes [1, 22], which can have confounding effects on MR imaging. Myelin loss results in hypointensity on phase and $R_2^\star$ images, while iron accumulation results in hypointensity on phase images and hyperintensity on $R_2^\star$ images. Six nonstain-

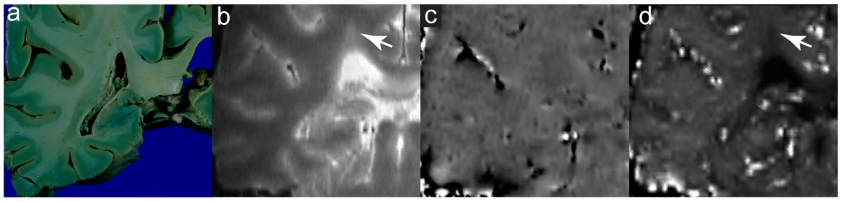

Figure 4.6: (a) Pathology specimen and (b-d) in situ postmortem MR images from subject 3 show evidence of shadow plaques as defined by pathologic findings. (a) Perls iron-stained 8-mm-thick coronal cerebral slice shows absence of macroscopically identifiable lesions. (b) T_2-weighted fast SE MR image shows an area of hyperintensity (arrow) corresponding to an MS lesion. (c) Phase image shows no visible lesion. (d) $R_2^\star$ map shows an area of hypointensity (arrow) corresponding to a lesion.

ing lesions in subject 1 demonstrated hypointensity on phase images both around the periphery and centrally. Therefore, hypointensity on phase images should not be interpreted as iron in MS lesions [45] since it can also arise from demyelination. $R_2^\star$ maps with lesions displaying a rim of hyperintensity were specific for iron, although not sensitive, and could represent infiltration of inflammatory cells containing iron [22] preceding edema and myelin loss. Subject 3 had shadow plaque MS lesions, which demonstrated no staining and were not visible on phase images, but appeared hypointense on $R_2^\star$ maps. This could indicate that $R_2^\star$ maps are more sensitive to myelin loss or dysfunction than are phase images when iron is absent.

Advantages of phase imaging include short imaging time, low specific absorption rate, and less sensitivity to water content changes. However, the method of postprocessing can affect the extent of background phase removal and contrast within large deep grey matter structures [40, 46, 47], where a Hanning filter may be suboptimal in both regards. Furthermore, external field effects from improper background removal or other nearby iron-containing structures could influence measured phase values; therefore, directly adjacent reference phase measures should be obtained. The $R_2^\star$ mapping protocol was also relatively time efficient; however, similar to phase imaging, it can be sensitive to susceptibility differences, such as near air-tissue interfaces or large venous structures. R_2 mapping uses SE to refocus the signal in these regions. However, to compensate for a high specific absorption rate, which is problematic at high field strength [48], a limited number of sections and long repetition times were used. Given these constraints, the R_2 method used thicker sections and slightly lower in-plane resolution than did the $R_2^\star$ method; thus, spatial resolution differences may have also played a role in the lower correlation with iron. T_2-weighted fast SE MR images were acquired at the highest spatial resolution (0.06 - 0.12 mm^3), which enabled high spatial specificity, but radiofrequency inhomogeneity and additional contrast mechanisms could lead to variable image contrast with this method.

There were several limitations associated with our study. Different parameters were chosen for each MR imaging method, including section thickness, in-plane resolution, and coverage, which could have made direct comparison between methods difficult. The optimal in vivo parameters for each method were used, and these parameters were chosen to achieve appropriate signal-to-noise ratio, image contrast, and imaging time [12]. Therefore, the results should have better applicability for in vivo use. An additional limitation is that MR images were acquired in the standard axial plane, while the attending neuropathologist preferred coronal sections in three cases, so MR image reformatting was necessary to achieve correspondence. However, since large ROIs were used around structural borders for quantitative measurements on both pathologic slices and MR images, resolution and original orientation of MR images should not have had a large influence on these measurements because many voxels were averaged. Independent regression analysis was conducted because of variable parameters, including brain duration in formalin and time after death of MR imaging, which precluded a single regression. Therefore, P values should be interpreted appropriately, as they have not been corrected for multiple comparisons. In subject 4, additional changes could have taken place over the year between imaging and death, which could affect correlation findings. Furthermore, changes occurring hours after death could also affect iron correlations in subjects 1-3.

In conclusion, subcortical grey matter measurement of transverse relaxation rates (ie, R_2 and $R_2^\star$) and phase imaging, as well as standard T_2-weighted fast SE MR imaging, provide good correlation with iron content as measured with Perls iron stain in subject with MS, with $R_2^\star$ having the highest correlation. The relationship between iron and MS lesion appearance on MR images was highly variable owing to the influence of complex pathophysiologic characteristics other than iron on image contrast.

4.6 Advances in Knowledge

- Transverse relaxation and phase measures have significant correlation to iron staining in subcortical grey matter of patients with multiple sclerosis (MS).

- $R_2^\star$ mapping has a higher correlation ($R^2 = 0.857, 0.628, 0.685$; all $P < .001$) to iron in subcortical grey matter structures in MS compared with R_2 mapping ($R^2 = 0.807, 0.615, 0.628, 0.489$; all $P \leq 0.034$), phase imaging ($R^2 = 0.672, 0.441, 0.596, 0.548$; all $P \leq 0.001$), and T_2-weighted imaging ($R^2 = 0.463, 0.582, 0.650, 0.511$; all $P < 0.001$).

- Hypointense MS lesions on phase images do not always contain iron and can result from demyelination.

- Hyperintense rims around MS lesions on $R_2^\star$ maps were only present in iron-staining lesions.

4.7 Implication for Patient Care

- In subcortical grey matter in MS, hypointensity with T_2-weighting, increases in transverse relaxation rate, and more negative phase can mainly be attributed to iron.

4.8 Acknowledgements

Supported by Natural Sciences and Engineering Research Council of Canada, Canadian Institutes of Health Research, and Multiple Sclerosis Society of Canada. A.J.W. supported by a Vanier Canada Graduate Scholarship and an Alberta Innovates Health Solutions MD/PhD studentship.

We thank Thomas Turner for his assistance with photography of the gross pathologic specimens.

Bibliography

[1] Williams R, Buchheit CL, Berman NE, LeVine SM. Pathogenic implications of iron accumulation in multiple sclerosis. Journal of neurochemistry 2012; 120(1):7–25.

[2] Craelius W, Migdal MW, Luessenhop CP, Sugar A, Mihalakis I. Iron deposits surrounding multiple sclerosis plaques. Archives of pathology & laboratory medicine 1982;106(8):397–9.

[3] LeVine SM. Iron deposits in multiple sclerosis and Alzheimer's disease brains. Brain Research 1997;760(1-2):298–303.

[4] Adams CW. Perivascular iron deposition and other vascular damage in multiple sclerosis. Journal of neurology, neurosurgery, and psychiatry 1988;51(2):260–5.

[5] Drayer B, Burger P, Hurwitz B, Dawson D, Cain J. Reduced signal intensity on MR images of thalamus and putamen in multiple sclerosis: increased iron content? AJR Am J Roentgenol 1987;149(2):357–63.

[6] Haacke EM, Cheng NY, House MJ, Liu Q, Neelavalli J, Ogg RJ, Khan A, Ayaz M, Kirsch W, Obenaus A. Imaging iron stores in the brain using magnetic resonance imaging. Magnetic Resonance Imaging 2005;23(1):1–25.

[7] Schenck JF, Zimmerman EA. High-field magnetic resonance imaging of brain iron: birth of a biomarker? NMR in biomedicine 2004;17(7):433–45.

[8] Ogg RJ, Langston JW, Haacke EM, Steen RG, Taylor JS. The correlation between phase shifts in gradient-echo MR images and regional brain iron concentration. Magn Reson Imaging 1999;17(8):1141–8.

[9] Shmueli K, de Zwart JA, van Gelderen P, Li TQ, Dodd SJ, Duyn JH. Magnetic Susceptibility Mapping of Brain Tissue In Vivo Using MRI Phase Data. Magnetic Resonance in Medicine 2009;62(6):1510–1522.

[10] Zhang Y, Zabad RK, Wei X, Metz LM, Hill MD, Mitchell JR. Deep grey matter "black T2" on 3 tesla magnetic resonance imaging correlates with disability in multiple sclerosis. Multiple sclerosis 2007;13(7):880–3.

[11] Khalil M, Langkammer C, Ropele S, Petrovic K, Wallner-Blazek M, Loitfelder M, Jehna M, Bachmaier G, Schmidt R, Enzinger C, Fuchs S, Fazekas F. Determinants of brain iron in multiple sclerosis: a quantitative 3T MRI study. Neurology 2011;77(18):1691–7.

[12] Lebel RM, Eissa A, Seres P, Blevins G, Wilman AH. Quantitative high-field imaging of sub-cortical gray matter in multiple sclerosis. Multiple sclerosis 2012;18(4):433–41.

[13] Ge Y, Jensen JH, Lu H, Helpern JA, Miles L, Inglese M, Babb JS, Herbert J, Grossman RI. Quantitative assessment of iron accumulation in the deep gray matter of multiple sclerosis by magnetic field correlation imaging. AJNR American journal of neuroradiology 2007;28(9):1639–44.

[14] Mitsumori F, Watanabe H, Takaya N. Estimation of Brain Iron Concentration In Vivo Using a Linear Relationship Between Regional Iron and Apparent Transverse Relaxation Rate of the Tissue Water at 4.7T. Magnetic Resonance in Medicine 2009;62(5):1326–1330.

[15] He X, Yablonskiy DA. Biophysical mechanisms of phase contrast in gradient echo MRI. Proc Natl Acad Sci U S A 2009;106(32):13558–63.

[16] Wharton S, Bowtell R. Whole-brain susceptibility mapping at high field: a comparison of multiple- and single-orientation methods. Neuroimage 2010; 53(2):515–25.

[17] Yao B, Li TQ, Gelderen P, Shmueli K, de Zwart JA, Duyn JH. Susceptibility contrast in high field MRI of human brain as a function of tissue iron content. Neuroimage 2009;44(4):1259–66.

[18] Wallis LI, Paley MN, Graham JM, Grunewald RA, Wignall EL, Joy HM, Griffiths PD. MRI assessment of basal ganglia iron deposition in Parkinson's disease. Journal of Magnetic Resonance Imaging 2008;28(5):1061–7.

[19] Hallgren B, Sourander P. The effect of age on the non-haemin iron in the human brain. Journal of neurochemistry 1958;3(1):41–51.

[20] Hopp K, Popescu BF, McCrea RP, Harder SL, Robinson CA, Haacke ME, Rajput AH, Rajput A, Nichol H. Brain iron detected by SWI high pass filtered phase calibrated with synchrotron X-ray fluorescence. Journal of Magnetic Resonance Imaging 2010;31(6):1346–54.

[21] Langkammer C, Krebs N, Goessler W, Scheurer E, Ebner F, Yen K, Fazekas F, Ropele S. Quantitative MR imaging of brain iron: a postmortem validation study. Radiology 2010;257(2):455–62.

[22] Bagnato F, Hametner S, Yao B, van Gelderen P, Merkle H, Cantor FK, Lassmann H, Duyn JH. Tracking iron in multiple sclerosis: a combined imaging and histopathological study at 7 Tesla. Brain : a journal of neurology 2011; 134(Pt 12):3602–15.

[23] Schrag M, McAuley G, Pomakian J, Jiffry A, Tung S, Mueller C, Vinters HV, Haacke EM, Holshouser B, Kido D, Kirsch WM. Correlation of hypointensities in susceptibility-weighted images to tissue histology in dementia patients with cerebral amyloid angiopathy: a postmortem MRI study. Acta neuropathologica 2010;119(3):291–302.

[24] Yao B, Bagnato F, Matsuura E, Merkle H, van Gelderen P, Cantor FK, Duyn JH. Chronic multiple sclerosis lesions: characterization with high-field-strength MR imaging. Radiology 2012;262(1):206–15.

[25] Dawe RJ, Bennett DA, Schneider JA, Vasireddi SK, Arfanakis K. Postmortem MRI of human brain hemispheres: T2 relaxation times during formaldehyde fixation. Magnetic Resonance in Medicine 2009;61(4):810–8.

[26] van Duijn S, Nabuurs RJ, van Rooden S, Maat-Schieman ML, van Duinen SG, van Buchem MA, van der Weerd L, Natte R. MRI artifacts in human brain tissue after prolonged formalin storage. Magnetic Resonance in Medicine 2011; 65(6):1750–8.

[27] Bischoff K, Lamm C, Erb HN, Hillebrandt JR. The effects of formalin fixation and tissue embedding of bovine liver on copper, iron, and zinc analysis. Journal of veterinary diagnostic investigation 2008;20(2):220–4.

[28] Shepherd TM, Flint JJ, Thelwall PE, Stanisz GJ, Mareci TH, Yachnis AT, Blackband SJ. Postmortem interval alters the water relaxation and diffusion properties of rat nervous tissue–implications for MRI studies of human autopsy samples. Neuroimage 2009;44(3):820–6.

[29] Schrag M, Dickson A, Jiffry A, Kirsch D, Vinters HV, Kirsch W. The effect of formalin fixation on the levels of brain transition metals in archived samples. Biometals : an international journal on the role of metal ions in biology, biochemistry, and medicine 2010;23(6):1123–7.

[30] Lebel RM, Wilman AH. Time-efficient fast spin echo imaging at 4.7 T with low refocusing angles. Magnetic Resonance in Medicine 2009;62(1):96–105.

[31] Lebel RM, Wilman AH. Transverse relaxometry with stimulated echo compensation. Magnetic Resonance in Medicine 2010;64(4):1005–14.

[32] Meguro R, Asano Y, Odagiri S, Li CT, Iwatsuki H, Shoumura K. Nonheme-iron histochemistry for fight and electron microscopy: a historical, theoretical and technical review. Archives of Histology and Cytology 2007;70(1):1–19.

[33] Rasband WS. ImageJ. US National Institutes of Health, Bethesda, Maryland, USA, 1997-2011;.

[34] Bizzi A, Brooks RA, Brunetti A, Hill JM, Alger JR, Miletich RS, Francavilla TL, Di Chiro G. Role of iron and ferritin in MR imaging of the brain: a study in primates at different field strengths. Radiology 1990;177(1):59–65.

[35] Vaughan JT, Garwood M, Collins CM, Liu W, DelaBarre L, Adriany G, Andersen P, Merkle H, Goebel R, Smith MB, Ugurbil K. 7T vs. 4T: RF power, homogeneity, and signal-to-noise comparison in head images. Magnetic Resonance in Medicine 2001;46(1):24–30.

[36] Baudrexel S, Volz S, Preibisch C, Klein JC, Steinmetz H, Hilker R, Deichmann R. Rapid single-scan T2*-mapping using exponential excitation pulses and image-based correction for linear background gradients. Magnetic Resonance in Medicine 2009;62(1):263–8.

[37] Du YPP, Jin ZY, Hu YZ, Tanabe J. Multi-Echo Acquisition of MR Angiography and Venography of the Brain at 3 Tesla. Journal of Magnetic Resonance Imaging 2009;30(2):449–454.

[38] Haacke EM, Xu Y, Cheng YC, Reichenbach JR. Susceptibility weighted imaging (SWI). Magnetic Resonance in Medicine 2004;52(3):612–8.

[39] Schafer A, Wharton S, Gowland P, Bowtell R. Using magnetic field simulation to study susceptibility-related phase contrast in gradient echo MRI. Neuroimage 2009;48(1):126–137.

[40] Walsh AJ, Eissa A, Blevins G, Wilman AH. Susceptibility phase imaging with improved image contrast using moving window phase gradient fitting and minimal filtering. Journal of magnetic resonance imaging 2012;36(6):1460–9.

[41] Masuda T, Kasai T, Satodate R. Quantitative measurement of hemosiderin deposition in tissue sections of the liver by image analysis. Analytical and quantitative cytology and histology / the International Academy of Cytology [and] American Society of Cytology 1993;15(6):379–82.

[42] Hammond KE, Lupo JM, Xu D, Metcalf M, Kelley DA, Pelletier D, Chang SM, Mukherjee P, Vigneron DB, Nelson SJ. Development of a robust method for generating 7.0 T multichannel phase images of the brain with application to normal volunteers and patients with neurological diseases. Neuroimage 2008; 39(4):1682–92.

[43] Pawate S, Wang L, Song Y, Sriram S. Analysis of T2 Intensity by Magnetic Resonance Imaging of Deep Gray Matter Nuclei in Multiple Sclerosis Patients: Effect of Immunomodulatory Therapies. Journal of neuroimaging 2011;.

[44] Haacke EM, Makki M, Ge YL, Maheshwari M, Sehgal V, Hu JN, Selvan M, Wu Z, Latif Z, Xuan Y, Khan O, Garbern J, Grossman RI. Characterizing Iron Deposition in Multiple Sclerosis Lesions Using Susceptibility Weighted Imaging. Journal of Magnetic Resonance Imaging 2009;29(3):537–544.

[45] Hagemeier J, Heininen-Brown M, Poloni GU, Bergsland N, Magnano CR, Durfee J, Kennedy C, Carl E, Weinstock-Guttman B, Dwyer MG, Zivadinov R. Iron deposition in multiple sclerosis lesions measured by susceptibility-weighted imaging filtered phase: A case control study. Journal of Magnetic Resonance Imaging 2012;.

[46] Schweser F, Deistung A, Lehr BW, Reichenbach JR. Quantitative imaging of intrinsic magnetic tissue properties using MRI signal phase: An approach to in vivo brain iron metabolism? Neuroimage 2011;54(4):2789–2807.

[47] Liu T, Khalidov I, de Rochefort L, Spincemaille P, Liu J, Tsiouris AJ, Wang Y. A novel background field removal method for MRI using projection onto dipole fields (PDF). NMR in biomedicine 2011;24(9):1129–36.

[48] Laule C, Kozlowski P, Leung E, Li DK, Mackay AL, Moore GR. Myelin water imaging of multiple sclerosis at 7 T: correlations with histopathology. Neuroimage 2008;40(4):1575–80.

Chapter 5

Longitudinal MRI of iron in multiple sclerosis: an imaging marker of disease [1]

5.1 Abstract

Purpose: To investigate over a two year period the relationship between MRI markers of iron and disease severity in patients with multiple sclerosis.

Materials and Methods: This prospective study was approved by the local ethics committee, and written informed consent was obtained from all participants. Seventeen multiple sclerosis subjects and 17 control subjects were examined twice, 2 years apart, using phase imaging and transverse relaxation ($R_2^\star$) mapping at 4.7 tesla. Quantitative iron differences between patients and controls were evaluated with repeated measures MANOVA separately for $R_2^\star$ mapping and phase imaging. Multiple regression analysis was used to evaluate correlations of MRI measures, both two year difference and single time point measurements, to baseline disease severity.

Results: $R_2^\star$ mapping using two year difference measurements had the highest correlation to disease severity (r=0.905, p<0.001) compared to $R_2^\star$ mapping using single time point measurements (r=0.560, p=0.019) and phase imaging using either single time point (r=0.539, p=0.026) or two year differences (r=0.644, p=0.005). Significant increases in $R_2^\star$ occur over 2 years in the substantia nigra (p<0.001) and globus pallidus (p=0.035) in patients compared to controls, which are both predictors of disease in regression analysis. There were group differences in the substantia nigra, globus pallidus, pulvinar nucleus, thalamus, and caudate nucleus

[1] A version of this section has been accepted for publication. Andrew J. Walsh, BSc, Gregg Blevins, MD, R. Marc Lebel, PhD, Peter Seres, MSc, Derek J. Emery, MD, and Alan H. Wilman, PhD. Longitudinal MRI of iron in multiple sclerosis: an imaging marker of disease. Radiology (Accepted)

compared to controls with $R_2^\star$ mapping ($p<0.05$) and group differences in the caudate nucleus and pulvinar nucleus compared to controls with phase imaging ($p<0.05$).

Conclusions: There are significant changes in deep grey matter iron content in multiple sclerosis over two years measured with MRI, changes that are strongly related to physical disability. Longitudinal measurements may produce a higher correlation to disease severity compared to single time point measurements because baseline iron content of deep grey matter is variable among subjects.

5.2 Introduction

Brain iron has been implicated in the pathophysiology of multiple sclerosis (MS) and might represent a marker of disease activity or contribute to disease progression [1]. Iron has been studied both histologically and with MRI in the deep grey matter and within lesions [2], and could contribute to disease through different mechanisms. MRI offers an in vivo approach for analyzing brain iron and has shown that iron levels are above normal in certain brain regions and that these iron measures in cross-sectional studies correlate with disease severity in MS [3][4][5]. However, the temporal course of brain iron is unknown and analysis of iron changes, rather than single time point measurements, could aid in understanding iron pathology in MS or represent a new method of classifying disease severity.

Iron is necessary for normal cellular function and is required in DNA synthesis, neurotransmitter production, and ATP generation [6]. In many brain regions, iron increases with age at different rates and there is substantial regional variation [7]. Deep grey matter typically contains the highest iron concentration possibly due to neurotransmitter metabolism or high energy requirements [8]. Although excess iron has been observed in MS, the pathological process is unclear. Excess or ill-stored iron can cause the formation of free radicals through the Fenton or Haber-Weiss reactions which can damage proteins, lipids, and DNA [9]. Alternatively, iron accumulation may be a byproduct of other processes such as mitochondrial or neuronal dysfunction [6]. Whether iron is a contributor to disease or a benign byproduct, it could serve as a biomarker of MS disease activity.

Current clinical MRI methods for the assessment of MS do not provide quantitative tissue contrast. Furthermore, many MRI methods of evaluating disease severity, such as measuring lesion load or counting new gadolinium enhancing lesions, do not significantly correlate with functional measures [10][11]. Longitudinal lesion analyses either show no correlation [10] or a moderate correlation to disability [11][12]. Iron measurement of deep grey matter using MRI might provide a method of predicting disease severity and therefore serve as a biomarker for disease progression. There are several MRI techniques which are sensitive to iron including the trans-

verse relaxation rates R_2 [13] and $R_2^\star$[14], and phase [15]. These methods indicate elevated iron in MS patients relative to healthy controls in many deep grey matter regions [4][5][16]. Furthermore, correlations have been demonstrated between these MRI methods and functional measures such as the Kurtzke Expanded Disability Status Scale (EDSS) [4], cognition [17], and disease duration [16]. However, the temporal relationship of iron accumulation in relapsing remitting MS (RRMS) is unknown from cross sectional MRI studies. A wide variation in normal iron content exists across individuals in deep grey matter [7] therefore single time point iron measurements may not be adequate to determine if iron is pathologically changing in individual patients. Longitudinal analysis would be more powerful in distinguishing abnormal brain iron in individual subjects.

Previous imaging studies have used non-quantitative, T_2-weighted fast spin echo methods in longitudinal iron analysis [18][19][20]. However, the contrast generated is dependent on imaging parameters which makes interstudy comparisons difficult. Furthermore, these investigations did not compare iron measurements to a control group. This is important as disease related iron accumulation must be differentiated from normal age related accumulation.

Phase imaging and $R_2^\star$ mapping are promising methods for iron evaluation in deep grey matter and hold several advantages over other MRI methods: contrast is less influenced by imaging parameters, imaging times are relatively fast, and data for both image types can be collected in the same sequence. Although many tissue components can influence the image contrast of phase imaging and $R_2^\star$ mapping, iron content contributes substantially in deep grey matter [21][22] and iron sensitivity increases with field strength [23]. This study uses these quantitative high field MRI methods to longitudinally evaluate iron accumulation in the deep grey matter in RRMS patients relative to controls. Therefore, the purpose of this work was to longitudinally investigate the relationship between imaging markers of iron and disease severity in patients with multiple sclerosis over a two-year period.

5.3 Materials and Methods

5.3.1 Subjects

Seventeen patients with RRMS and 17 age and gender matched controls were studied from June 2009 to December 2012 in this prospective study. Institutional ethical approval and informed consent were obtained from the subjects prior to the study. Each subject was imaged twice, 2 years apart. Inclusion criteria for patients were: a diagnosis of RRMS according to the 2005 McDonald criteria [24], and ambulatory without aid (EDSS < 6.0) at time of enrolment. Exclusion criteria for all subjects were: other neurological diseases and MRI contraindications. None of the patients

and volunteers who were enrolled and provided informed consent were subsequently excluded.

5.3.2 MRI Data Acquisition and Processing

Imaging was performed with a Varian Unity Inova 4.7T MRI system. Three-dimensional multi-echo-gradient echo $R_2^\star$ mapping was performed with parameters: TR, 44 msec; 10 echoes with 4.1 msec echo spacing; first echo, 2.93 msec; flip angle, 10°; FOV, 160.0 x 256.0 x 160.0 mm; voxel size, 1.0 x 1.0 x 2.0 mm; acquisition time, 9.4 min. Two-dimensional flow compensated single echo gradient echo phase imaging was performed with parameters: TR/TE, 1540 msec/15 msec; flip angle, 65°; 50 contiguous slices; FOV, 192.5 x 256.0 x 100.0 mm; voxel size, 0.5 x 0.75 x 2 mm; acquisition time, 6.6 min. A volumetric T_1-weighted acquisition was also performed to assess head position measured along the anterior commissure posterior commissure (AC-PC) line in the sagittal orientation.

$R_2^\star$ mapping used a weighted non-linear least-squares fit to a monoexponential signal decay versus echo time. Prior to fitting, source images were intensity corrected to compensate for large-scale air-tissue susceptibility effects [25]; weighting factors were inversely proportional to the intensity correction factor to account for noise amplification. Phase images were processed using two separate background phase removal methods: a standard high pass Hanning filter with filter width 0.125 [26] and moving window gradient fitting with filter width 0.0625 [27].

5.3.3 ROI Analysis

Region-of-interest (ROI) analysis using ImageJ [28] was conducted by separately obtaining two-dimensional ROIs from axial $R_2^\star$ maps and magnitude images from the phase acquisition. ROIs from $R_2^\star$ maps were subsequently verified on gradient echo magnitude images (TE=15ms) from the $R_2^\star$ mapping acquisition. Regions studied included the head of the caudate nucleus, putamen, globus pallidus, thalamus (excluding the pulvinar nucleus), pulvinar nucleus, substantia nigra, and red nucleus. The AC-PC angle was obtained in each subject prior to ROI placement and the correct slice for each structure was identified in the superior inferior direction relative to the standard. ROIs were standardized between subjects, based on axial deep grey matter orientation with the AC-PC line oriented at 0°. The standard orientation defines axial ROIs through the center slice of the putamen and from the caudate nucleus, globus pallidus, thalamus and pulvinar nucleus in the same slice and inferiorly ROIs were obtained through the center slice of the substantia nigra and through the red nucleus in the same slice (Fig 5.1).

In phase images, the effects of nonlocal external field effects were mitigated by obtaining reference phase measurements from nearby normal appearing white

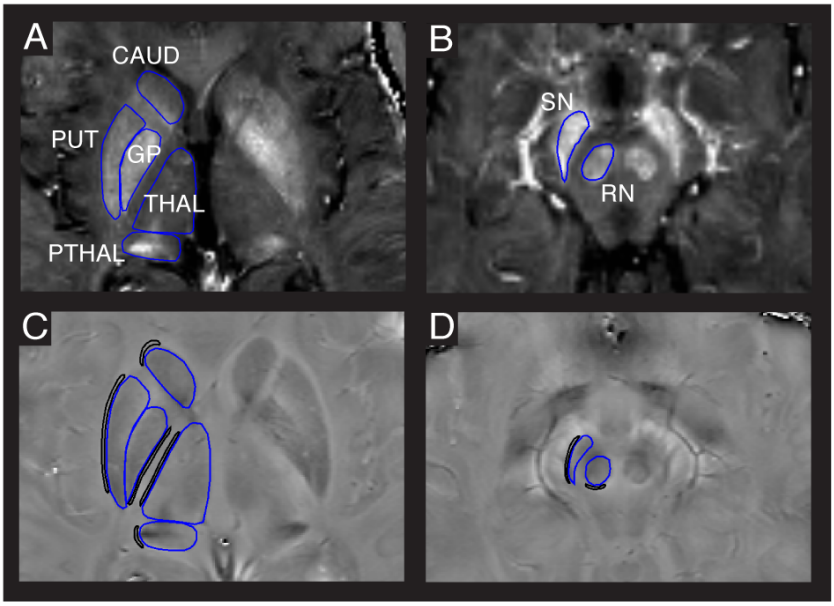

Figure 5.1: ROI placement (blue outline) for the seven deep grey matter structures from a 36 year old female MS patient (EDSS 5.0) drawn on $R_2^\star$ maps (A,B) and separately on gradient echo magnitude images; the latter are transferred to the corresponding phase images (C,D). Baseline phase measurements (black outline) are obtained directly adjacent to structures to minimize nonlocal field effects and separately in white matter for reliability comparison for phase images (not shown in figure). CAUD: head of caudate nucleus, PUT: putamen, GP: globus pallidus, THAL: thalamus excluding the pulvinar nucleus, PTHAL: pulvinar nucleus, SN: substantia nigra, RN: red nucleus.

matter [22] both directly adjacent to each structure and separately in frontal and posterior white matter (Fig 5.1).

5.3.4 Statistical Analysis

MRI markers of iron were evaluated longitudinally in each structure using separate repeated measures MANOVA with a Wilks Lambda test in SPSS (IBM,Armonk, NY). Parameter values were averaged within each 2D ROI then averaged between hemispheres. Group differences were evaluated between MS subjects and controls as a between subjects effect and changes over time were evaluated as a within subjects effect.

Multiple regression analysis was conducted to determine the correlation between two year changes in deep grey matter iron content and the baseline MS Severity Score (MSSS) [29] independently with both phase and $R_2^\star$ measurements. A separate multiple regression analysis was performed to determine if measurements using a single time point, from the second MRI in each subject, are an effective predictor of MSSS.

For both tests, a backwards elimination model was used with F=0.1 for removal with seven deep grey matter regions included as variables (Fig 5.1). A neurologist who specializes in MS measured EDSS for each subject. Baseline disability which was not influenced by an acute relapse was obtained by measuring EDSS close in time to the second MRI fulfilling two criteria: 1) EDSS measured at the time of study MRI if last relapse occurred more than four months before study MRI, or if last relapse occurred less than four months before study MRI and EDSS returned to prior baseline 2) EDSS measured prior to relapse if relapse occurred less than four months before study MRI and EDSS at time of study MRI increased from baseline. EDSS values and disease duration were input into the MSSStest program [29] to obtain MSSS values.

Table 5.1: Subject Demographics

	MS patients	Controls	p-value
Gender F/M	13/4	13/4	-
Age: Overall (yrs) (mean, range)	37.1	36.5 (25.4 - 54.5)	0.38
Age: Males (yrs) (mean, range)	37.6 (27.3 - 51.4)	35.3 (27.9 - 46.5)	0.22
Age: Females (yrs) (mean, range)	37.0 (27.8 - 50.5)	36.8 (25.4 - 54.5)	0.85
Time between imaging (weeks)	106 ± 22	107 ± 23	0.24
EDSS (median, range)	2.5 (1.0 - 6.0)		
MSSS	4.58 ± 2.42		
Disease Duration (yrs)	5.77 ± 2.77		
Time between MRI and EDSS measurement (weeks)	2.6 ± 7.8		

p-value obtained using a repeated measures Student's t-test.
Disease duration measured from index event to second study MRI.

To establish intrasubject variance of the quantitative MRI methods with 2D ROI analysis, a reliability test was performed on 4 healthy individuals ages 24-50 yrs that underwent the same MRI protocol, twice in the same day.

5.4 Results

5.4.1 Subjects

The control subjects compared to the patients with MS had no significant differences in age or in the time between MRI measurements (Table 5.1). There were no significant differences in head angle as measured with the AC-PC lines between patients 6.0 ± 7.1° and controls 3.0 ± 6.8° (p=0.29 paired) or difference in the head angle as measured over two years in individual subjects between patients 0.96 ± 0.74° and controls 1.21 ± 1.14° (p=0.34 paired).

Table 5.2: Same day scan-rescan test: percent variation of $R_2^\star$ and phase and measured head angle

Method	Subjects			
	1	2	3	4
$R_2^\star$ (%)	1.9 ± 1.3	2.4 ± 1.7	1.8 ± 1.6	1.2 ± 0.8
Phase - Gradient method with adjacent background (%)	10.4 ± 6.3	11.2 ± 8.3	8.4 ± 4.7	7.4 ± 5.0
Phase - Gradient method (%)	19.3 ± 26.1	19.6 ± 22.7	11.0 ± 9.3	27.5 ± 40.5
Phase - Standard high pass method with adjacent background (%)	21.6 ± 17.5	14.9 ± 15.1	11.2 ± 8.6	11.3 ± 7.4
Phase - Standard high pass method (%)	22.4 ± 22.4	17.9 ± 15.6	12.4 ± 13.6	12.4 ± 15.7
Head Angle 1 (°)	10.0	3.8	-2.6	0.9
Head Angle 2 (°)	8.5	4.7	-0.9	0.9

Measurements averaged bilaterally in 7 deep grey matter structures then averaged in each subject.
Percentages quoted with standard deviation.

5.4.2 Reliability

In the reliability assessment, the gradient phase processing method with adjacent background phase measurements [27] had the lowest intrasubject variability compared to the other phase processing methods and was selected for subsequent phase analysis (Table 5.2). $R_2^\star$mapping had substantially lower intrasubject variability compared to phase imaging.

5.4.3 Iron Differences

The multivariate Wilks Lambda test for $R_2^\star$ mapping was significant as a between subjects effect for Group (p=0.004) and as a within subjects effect for Time (p=0.017) and Time * Group (p=0.004), whereas phase was only significant as a between subjects effect for Group (p=0.037) and not as a within subjects effect for Time (p=0.094) or Time*Group (p=0.723). This indicates overall group differences across two measurement times between MS and control subjects using either phase imaging or $R_2^\star$ mapping, overall changes in $R_2^\star$ over time across groups, and changes between MS subjects relative to controls over time using $R_2^\star$ mapping. For $R_2^\star$ mapping, significant within subjects effects, using Greenhouse-Geisser tests, showed increases in $R_2^\star$ in MS patients over time relative to controls in the substantia nigra and globus pallidus (Table 5.3, Fig 5.2, Fig 5.3). As between subject effects, $R_2^\star$ mapping showed significantly larger values in MS patients compared to controls in five structures: substantia nigra, pulvinar nucleus, thalamus, caudate nucleus, and globus pallidus. Phase measurements showed significant between subject effects with lower phase values in MS patients for only the pulvinar nucleus and caudate nucleus.

5.4.4 Deep Grey Matter Regression to MSSS

Using multiple regression analysis with all deep grey matter structures included as variables, two-year difference measurements with $R_2^\star$ mapping had a high correlation to MSSS (r=0.905, p<0.001, MSSS = 0.232 SN - 0.348 Thal + 0.279 GP + 1.816) with the substantia nigra (SN), thalamus (Thal), and globus pallidus (GP) included in the regression (Fig 5.4). Two-year difference measurements with phase imaging correlated to MSSS with the substantia nigra as a predictor (r=0.644, p=0.005, MSSS=0.161 SN + 4.4652). Single time point measurements with $R_2^\star$ mapping correlated to MSSS with the pulvinar nucleus (pThal) as a predictor (r=0.560, p=0.019, MSSS = 0.264 pThal - 4.557). Singe time point measurements with phase imaging correlated to MSSS with the substantia nigra as a predictor (r=0.539, p=0.026, MSSS= 0.086 SN + 6.951). MSSS is normally distributed across the 17 patients with the Shapiro-Wilk test (p=0.388).

Independent regressions showed correlations to MSSS in several structures with

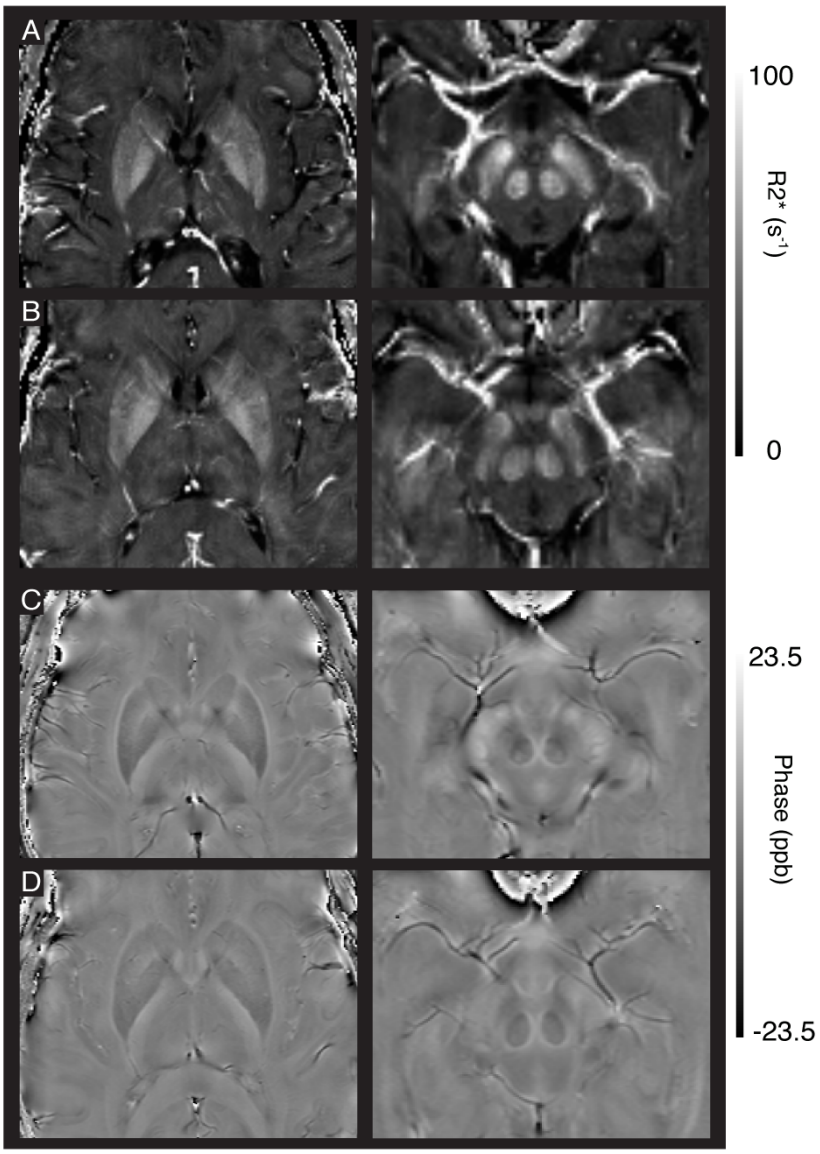

Figure 5.2: $R_2^\star$ maps and phase images from a 30 year old female MS patient (A,C) (EDSS 1.0) and a 30 year old female control subject (B,D). The substantia nigra of the MS patient is more hyperintense in the phase image and $R_2^\star$ map compared to the control subject. Furthermore, in the MS patient the pulvinar nucleus is more hypointense in the phase image and hyperintense in the $R_2^\star$ map.

$R_2^\star$ mapping and phase imaging, both as single time point measurements and difference measurements. Two year difference measurements using $R_2^\star$ mapping and phase imaging showed more deep grey matter regions had a significant correlation to MSSS compared to single time point measurements with either MRI method (Table 5.4, Fig 5.5).

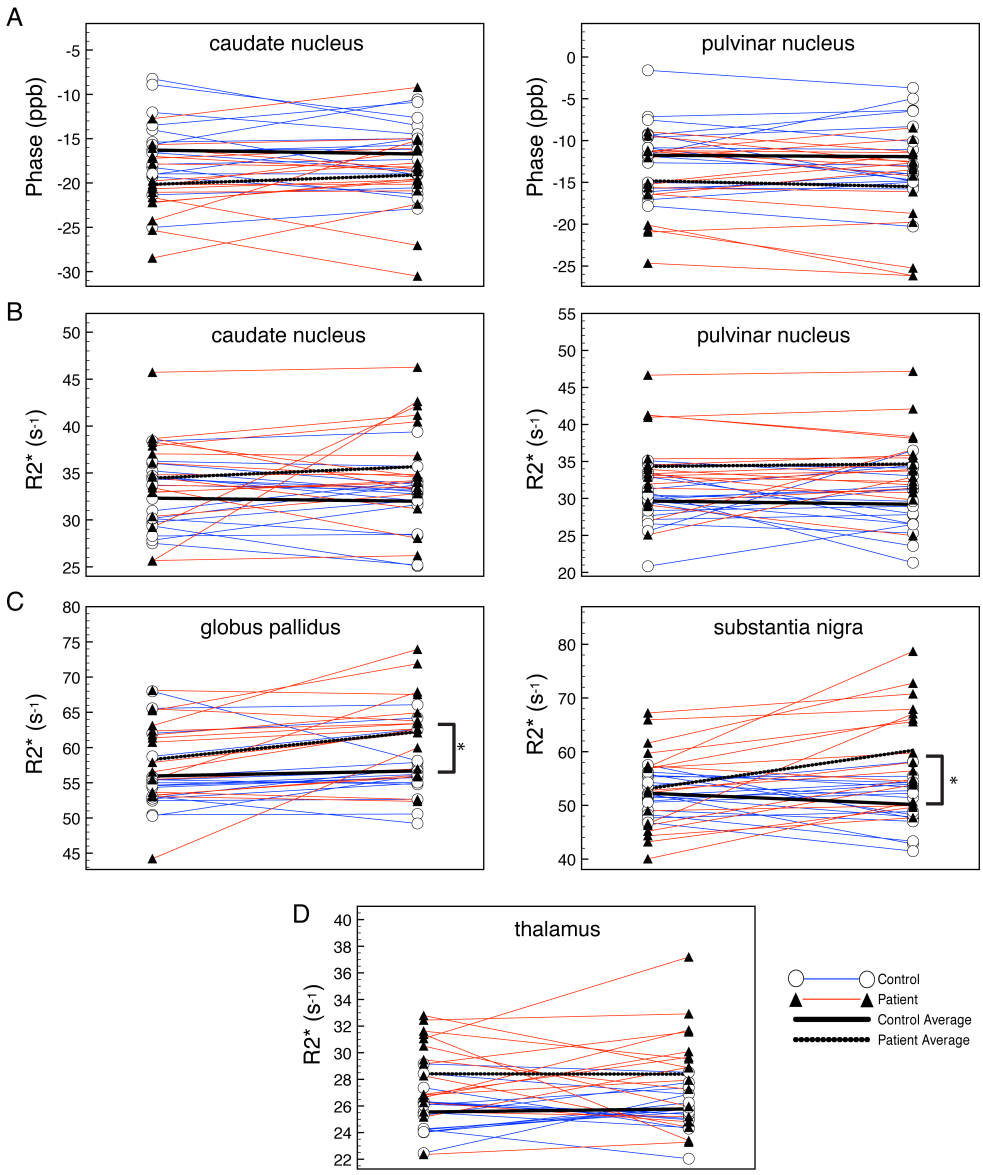

Figure 5.3: Deep grey matter measurements over two years using phase imaging (A) and $R_2^\star$ mapping (B-D). Individual subjects connected by solid lines (red: patients, blue: control) and group averages for MS subjects and controls represented by dotted and solid thick black lines respectively. All structures shown have a significant between groups effect ($p<0.05$) indicating an overall difference in iron between MS subjects and controls and structures with (*) have a significant within subjects effect ($p<0.05$) indicating a change over time in iron content between MS subjects and controls.

5.5 Discussion

In the current study we demonstrated that longitudinal changes in MRI markers of iron strongly correlated with disability in MS over a short duration of measure-

ment. These changes were relatively large and are above and beyond age-related iron changes.

The substantia nigra and globus pallidus showed increases in iron over time relative to controls as measured with $R_2^\star$ mapping during the 2-year interval. This could indicate that ongoing iron accumulation occurs primarily in certain structures during this stage of disease. The globus pallidus and substantia nigra are similar in that subdivisions of these nuclei serve as output of the basal ganglia and these nuclei contain the highest iron concentration in the brain [7]. Increased iron concentration in these nuclei in RRMS could arise from different mechanisms including altered neurotransmitter metabolism of dopamine or glutamate [8], activation of NMDA receptors which could enhance iron uptake [30], or altered local energy demands [1].

Multiple regression analysis of $R_2^\star$ mapping to MSSS produced a strong correlation and could provide a new way of following RRMS with imaging. Longitudinal phase and $R_2^\star$ measurements were stronger predictors of MSSS than single time point measurements, possibly because single time point measurements may be insufficient to discriminate elevated iron levels in RRMS from baseline iron variability among subjects [7]. Multiple regression analysis may have a higher correlation to MSSS compared to single regression analysis as various deep grey matter structures could have iron changes that relate to different aspects of disease. Iron accumulation within structures might not be a slow steady process and could be dynamic with disease progression as iron could increase in certain structures and decrease in others. Although thalamic iron in MS patients is increased overall compared to controls, the negative correlation of iron measured in the thalamus to MSSS in the multiple $R_2^\star$ regression might represent iron efflux. A similar iron decrease is observed in healthy individuals between ages 30-60 within the thalamus [7]. Phase analysis produces weaker, although still significant correlations using either single time point measurements or difference measurements over time, possibly because of the lower reliability of phase imaging. Although phase measurements have been negatively correlated with iron in most deep grey matter structures, a positive correlation is observed in the center axial slice of the substantia nigra due to shape effects on phase contrast [31]. Since $R_2^\star$ mapping had a high correlation to disease, future studies could investigate longitudinal $R_2^\star$ measurements for monitoring treatment or for predictive value of disease progression in individual patients. To better understand the biological process of deep grey iron changes in MS, human histology studies or in vitro analysis could offer detailed and unique information.

Table 5.3: Differences over two years of deep grey matter structures between MS patients and control subjects using Greenhouse-Geisser tests

Region	Group	$R_2^\star$ (sec^{-1})		Difference over time (p-value)	Group difference (p-value)	Phase (ppb)		Difference over time (p-value)	Group difference (p-value)
		Yr 0	Yr 2			Yr 0	Yr 2		
Globus Pallidus	Patient	58.3	62.2	0.035*	0.028*	-30.2	-30.1	0.223	0.244
	Control	56.0	56.7			-29.5	-27.1		
Putamen	Patient	41.2	42.7	0.765	0.069	-19.0	-20.1	0.937	0.275
	Control	38.9	39.9			-16.5	-17.6		
Caudate Nucleus	Patient	34.4	35.7	0.311	0.033*	-20.2	-19.1	0.203	0.023*
	Control	32.3	32.0			-16.3	-16.7		
Thalamus	Patient	28.4	28.4	0.808	0.001*	-14.2	-14.1	0.837	0.250
	Control	25.5	25.8			-12.9	-12.9		
Pulvinar Nucleus	Patient	34.3	34.7	0.600	0.001*	-14.8	-15.5	0.590	0.043*
	Control	29.6	29.2			-11.8	-11.9		
Substantia Nigra	Patient	53.1	60.2	<0.001*	0.016*	-26.9	-27.3	0.843	0.225
	Control	52.3	50.2			-31.8	-31.5		
Red Nucleus	Patient	47.8	50.0	0.131	0.338	-27.0	-27.7	0.782	0.530
	Control	47.6	47.0			-25.9	-25.9		

Note. * indicates significance with $p<0.05$.

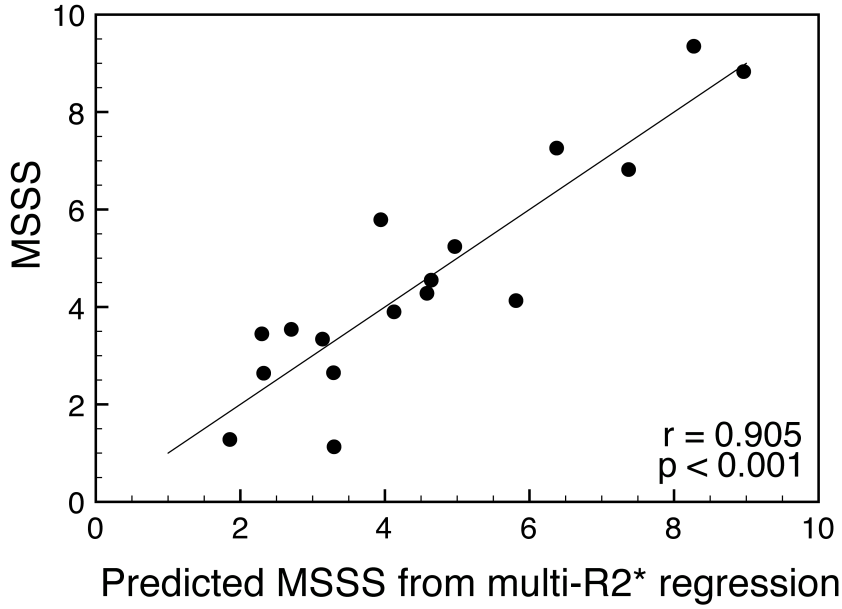

Figure 5.4: Predicted MSSS using $R_2^\star$ multiple regression analysis compared to measured MSSS. Two year $R_2^\star$ difference measurements from substantia nigra, globus pallidus, and thalamus are included in the regression model.

Measurements from $R_2^\star$ maps had higher scan-rescan reliability than measurements from phase images. The intrasubject reliability of phase is lower than $R_2^\star$ mapping, possibly due to phase filtering effects with the standard phase method [22] and head angle differences which can affect phase measurements [32]. Head angle correction methods or standardization could improve significance and reliability of phase imaging analysis. These issues are less problematic for $R_2^\star$ mapping. Furthermore, differences in the results between phase imaging and $R_2^\star$ mapping could be attributed to physical mechanisms behind image contrast. Phase image contrast not only depends upon iron content but also structure shape which causes local and non-local field effects [31]. $R_2^\star$ decay is also affected by other mechanisms such as dipole-dipole interactions. Multicomponent exponential $R_2^\star$ decay is possible in deep grey matter but is likely more representative of signal decay in highly compartmentalized white matter [33]. Furthermore, $R_2^\star$ decay may be non exponential due to areas of background magnetic gradients, vascular networks, or a highly compartmentalized iron distribution [34]. These factors are likely minimal in deep grey matter because a monoexponential model produces a high correlation to iron in both healthy controls and patients with MS in validation studies[21][22].

Deep grey matter structures including the globus pallidus, caudate nucleus, thalamus, pulvinar nucleus, and substantia nigra showed group differences in $R_2^\star$ measurements between RRMS patients and the control group which agree with results from previous studies [3][4]. Therefore, iron concentration within these structures

Table 5.4: Correlation of deep grey matter structures to MSSS

	Two year difference (r) (p-value)		Singe time point (r) (p-value)	
Structure	$R_2^\star$	phase	$R_2^\star$	phase
Substantia Nigra	0.715 (0.001)*	0.644 (0.005)*	0.345 (0.175)	0.539 (0.026)*
Red Nucleus	0.317 (0.215)	-0.521 (0.032)*	0.363 (0.153)	-0.259 (0.315)
Pulvinar Nucleus	0.484 (0.049)*	-0.506 (0.038)*	0.560 (0.019)*	-0.247 (0.339)
Thalamus	-0.151 (0.562)	-0.375 (0.138)	0.004 (0.987)	0.260 (0.313)
Caudate Nucleus	-0.044 (0.868)	0.088 (0.736)	0.210 (0.418)	0.137 (0.600)
Putamen	0.045 (0.862)	-0.049 (0.851)	0.160 (0.541)	0.038 (0.885)
Globus Pallidus	0.484 (0.049)*	-0.333 (0.192)	0.247 (0.340)	-0.028 (0.915)

Note. * indicates significance with $p<0.05$.

likely increases early in the disease course and may subsequently plateau or slowly increase in regions other than the globus pallidus and substantia nigra. Some studies have shown differences between CIS subjects and controls using T_2 hypointensity measurements [18], yet there is conflicting evidence as to whether the extent of hypointensity, measured at one timepoint, is a predictor of disease severity. Phase measurements showed fewer differences compared to $R_2^\star$ mapping with only two structures being significantly different as a between subjects effect. Since other studies have shown phase differences in the deep grey matter in MS [4][16], iron changes in MS measured with phase may require larger groups to find equivalent statistical significance to $R_2^\star$ mapping differences with smaller groups. The caudate nucleus, thalamus, and pulvinar nucleus could have early iron changes in MS due to axonal degeneration from cumulative damage during acute inflammation. These nuclei have more extensive anatomical connections throughout the cerebrum and spinal cord compared to other deep grey matter nuclei. Iron changes could oc-

cur in white matter, however image contrast in both phase images and $R_2^\star$ maps is more complex in white matter compared to deep grey matter and may require advance-processing techniques to assess tissue iron [35].

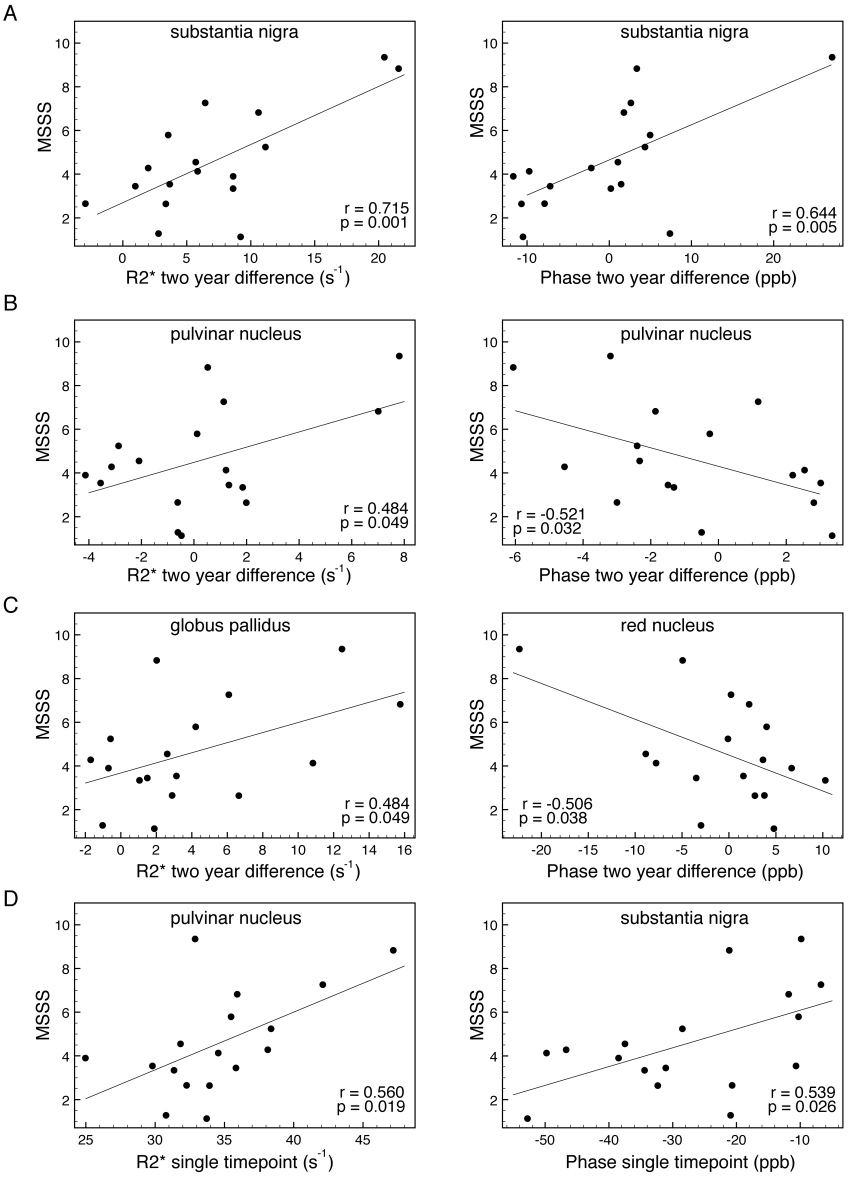

Figure 5.5: Regressions of deep grey matter MRI to MSSS using two year differences with $R_2^\star$ mapping measurements (A-left,B-left,C-left) and two year differences with phase measurements (A-right,B-right,C-right). Single time point measurements using $R_2^\star$ mapping (D-left) and phase imaging (D-Right).

The correlation of iron measurements in deep grey matter to disease severity is superior to the correlation of lesion volume changes to disease severity [10][11][12]. Iron concentration within deep grey matter may represent global CNS dysfunction while focal white matter hyperintensity can represent local aspects of the disease

including both dysfunction and repair. Grey matter atrophy measurements have been used to show group differences between MS patients and controls with moderate correlation to disease. However, average grey matter volume changes are small 0.3-1.1% per year [36][37] compared to 3.3-6.7% per year iron marker changes in the globus pallidus and substantia nigra and therefore atrophy may not be as powerful as a biomarker of disease progression in individual subjects or in population studies of shorter duration. In addition, atrophy measures require precise definition of structural borders which may be ill-defined, while $R_2^\star$ mapping is less dependent on precise edge determination.

Although age has been previously correlated with histologically determined iron [7] or quantitative phase and $R_2^\star$ MRI measurements [38], there was no correlation between $R_2^\star$ and age in the control group in this study, and a moderate correlation between $R_2^\star$ and age only in the head caudate nucleus in the patient group (r=0.63, p=0.007). This discrepancy is likely due to a smaller age range (25-54 yrs) and substantially fewer subjects in this study compared to the other two studies where more deep grey regions had significant correlations to age. The patient group $R_2^\star$ correlation to age in the caudate nucleus has little impact on the results of this study as MRI measurements in the caudate nucleus did not correlate to disease severity.

There are several limitations with this work. More longitudinal studies, with multiple time points and various disease severities, are needed to clarify temporal iron accumulation in specific deep grey matter structures. Measurements in early disease could distinguish which structures are the first to show iron changes with MRI; however, the rate of regional iron accumulation in MS might vary depending on disease duration and disease subtype. This study used a high field strength of 4.7 T which has the benefit of high iron sensitivity, however there are several limitations. It remains to be determined whether progression of disease would be as well correlated with different field strengths. As well, T_1 weighted images have poor deep grey matter contrast at high field strength mainly due to longer tissue T_1 relaxation times [39]. This makes atrophy measurements based on current automatic segmentation methods such as FSL FIRST unreliable at this field strength. Longitudinal atrophy measurements in relation to MRI measures of iron require further investigation as iron increases measured with $R_2^\star$ could be in part due to volume reduction [3]. However, $R_2^\star$ changes in deep grey matter are greater than atrophy changes indicating that other factors are likely involved.

5.5.1 Conclusion

MRI markers of iron in deep grey matter are easily measurable and show significant and substantial changes over two years that strongly correlate with disease severity. $R_2^\star$ and phase measurements compared over two years are a more effective predictor

of disease severity than single time point measurements. In conclusion, $R_2^\star$ mapping has a strong correlation to disease and a high intrasubject reliability, therefore this method could be useful as a surrogate marker to follow disease disability over short intervals in individuals or populations.

5.5.2 Advances in Knowledge

- Two year difference measurements of deep grey matter using $R_2^\star$ mapping have a high correlation to physical disability in multiple sclerosis (r=0.905, p<0.001).
- Differences in $R_2^\star$ measured over two years have a higher correlation to disease (r=0.905, p<0.001) than single time point measurements (r=0.560, p=0.019).
- $R_2^\star$ mapping of deep grey matter has high intra-subject scan-rescan reliability (1.8 ± 1.3 % variation).

5.5.3 Implications for Patient Care

- Quantitative iron evaluation of deep grey matter, based on $R_2^\star$ MRI measurements, have a high correlation to physical disability and could be useful as a surrogate marker to follow disease disability over short intervals in individuals or populations.

5.6 Acknowledgements

Supported by Canadian Institutes of Health Research, and Multiple Sclerosis Society of Canada. A.J.W. supported by a Vanier Canada Graduate Scholarship and an Alberta Innovates Health Solutions MD/PhD studentship.

Bibliography

[1] Williams R, Buchheit CL, Berman NE, LeVine SM. Pathogenic implications of iron accumulation in multiple sclerosis. Journal of neurochemistry 2012; 120(1):7–25.

[2] Bagnato F, Hametner S, Yao B, van Gelderen P, Merkle H, Cantor FK, Lassmann H, Duyn JH. Tracking iron in multiple sclerosis: a combined imaging and histopathological study at 7 Tesla. Brain : a journal of neurology 2011; 134(Pt 12):3602–15.

[3] Khalil M, Langkammer C, Ropele S, Petrovic K, Wallner-Blazek M, Loitfelder M, Jehna M, Bachmaier G, Schmidt R, Enzinger C, Fuchs S, Fazekas F. De-

terminants of brain iron in multiple sclerosis: a quantitative 3T MRI study. Neurology 2011;77(18):1691–7.

[4] Lebel RM, Eissa A, Seres P, Blevins G, Wilman AH. Quantitative high-field imaging of sub-cortical gray matter in multiple sclerosis. Multiple sclerosis 2012;18(4):433–41.

[5] Zhang Y, Zabad RK, Wei X, Metz LM, Hill MD, Mitchell JR. Deep grey matter "black T2" on 3 tesla magnetic resonance imaging correlates with disability in multiple sclerosis. Multiple sclerosis 2007;13(7):880–3.

[6] Benarroch EE. Brain iron homeostasis and neurodegenerative disease. Neurology 2009;72(16):1436–40.

[7] Hallgren B, Sourander P. The effect of age on the non-haemin iron in the human brain. Journal of neurochemistry 1958;3(1):41–51.

[8] Drayer B, Burger P, Hurwitz B, Dawson D, Cain J. Reduced signal intensity on MR images of thalamus and putamen in multiple sclerosis: increased iron content? AJR Am J Roentgenol 1987;149(2):357–63.

[9] Meguro R, Asano Y, Odagiri S, Li C, Shoumura K. Cellular and subcellular localizations of nonheme ferric and ferrous iron in the rat brain: a light and electron microscopic study by the perfusion-Perls and -Turnbull methods. Archives of Histology and Cytology 2008;71(4):205–22.

[10] Miki Y, Grossman RI, Udupa JK, Wei L, Polansky M, Mannon LJ, Kolson DL. Relapsing-remitting multiple sclerosis: longitudinal analysis of MR images–lack of correlation between changes in T2 lesion volume and clinical findings. Radiology 1999;213(2):395–9.

[11] Brex PA, Ciccarelli O, O'Riordan JI, Sailer M, Thompson AJ, Miller DH. A longitudinal study of abnormalities on MRI and disability from multiple sclerosis. The New England journal of medicine 2002;346(3):158–64.

[12] Rudick RA, Lee JC, Simon J, Fisher E. Significance of T2 lesions in multiple sclerosis: A 13-year longitudinal study. Annals of Neurology 2006;60(2):236–42.

[13] Gelman N, Gorell JM, Barker PB, Savage RM, Spickler EM, Windham JP, Knight RA. MR imaging of human brain at 3.0 T: preliminary report on transverse relaxation rates and relation to estimated iron content. Radiology 1999;210(3):759–67.

[14] Haacke EM, Cheng NY, House MJ, Liu Q, Neelavalli J, Ogg RJ, Khan A, Ayaz M, Kirsch W, Obenaus A. Imaging iron stores in the brain using magnetic resonance imaging. Magnetic Resonance Imaging 2005;23(1):1–25.

[15] Ogg RJ, Langston JW, Haacke EM, Steen RG, Taylor JS. The correlation between phase shifts in gradient-echo MR images and regional brain iron concentration. Magn Reson Imaging 1999;17(8):1141–8.

[16] Hammond KE, Metcalf M, Carvajal L, Okuda DT, Srinivasan R, Vigneron D, Nelson SJ, Pelletier D. Quantitative In Vivo Magnetic Resonance Imaging of Multiple Sclerosis at 7 Tesla with Sensitivity to Iron. Annals of Neurology 2008; 64(6):707–713.

[17] Brass SD, Benedict RHB, Weinstock-Guttman B, Munschauer F, Bakshi R. Cognitive impairment is associated with subcortical magnetic resonance imaging grey matter T2 hypointensity in multiple sclerosis. Multiple sclerosis 2006; 12(4):437–444.

[18] Neema M, Arora A, Healy BC, Guss ZD, Brass SD, Duan Y, Buckle GJ, Glanz BI, Stazzone L, Khoury SJ, Weiner HL, Guttmann CR, Bakshi R. Deep gray matter involvement on brain MRI scans is associated with clinical progression in multiple sclerosis. Journal of neuroimaging 2009;19(1):3–8.

[19] Zhang Y, Metz LM, Yong VW, Mitchell JR. 3T deep gray matter T2 hypointensity correlates with disability over time in stable relapsing-remitting multiple sclerosis: a 3-year pilot study. Journal of the neurological sciences 2010;297(1-2):76–81.

[20] Bermel RA, Puli SR, Rudick RA, Weinstock-Guttman B, Fisher E, Munschauer r F E, Bakshi R. Prediction of longitudinal brain atrophy in multiple sclerosis by gray matter magnetic resonance imaging T2 hypointensity. Arch Neurol 2005;62(9):1371–6.

[21] Langkammer C, Krebs N, Goessler W, Scheurer E, Ebner F, Yen K, Fazekas F, Ropele S. Quantitative MR imaging of brain iron: a postmortem validation study. Radiology 2010;257(2):455–62.

[22] Walsh A, Lebel R, Eissa A, Blevins G, Catz I, Lu J, Resch L, Johnson E, Emery D, Warren K, Wilman A. Multiple Sclerosis: Validation of MR Imaging for Quantification and Detection of Iron. Radiology 2013;(In Press).

[23] Peters AM, Brookes MJ, Hoogenraad FG, Gowland PA, Francis ST, Morris PG, Bowtell R. T2* measurements in human brain at 1.5, 3 and 7 T. Magnetic resonance imaging 2007;25(6):748–53.

[24] Polman CH, Reingold SC, Edan G, Filippi M, Hartung HP, Kappos L, Lublin FD, Metz LM, McFarland HF, O'Connor PW, Sandberg-Wollheim M, Thompson AJ, Weinshenker BG, Wolinsky JS. Diagnostic criteria for multiple sclerosis: 2005 revisions to the "McDonald Criteria". Annals of Neurology 2005; 58(6):840–6.

[25] Du YPP, Jin ZY, Hu YZ, Tanabe J. Multi-Echo Acquisition of MR Angiography and Venography of the Brain at 3 Tesla. Journal of Magnetic Resonance Imaging 2009;30(2):449–454.

[26] Haacke EM, Xu Y, Cheng YC, Reichenbach JR. Susceptibility weighted imaging (SWI). Magnetic Resonance in Medicine 2004;52(3):612–8.

[27] Walsh AJ, Eissa A, Blevins G, Wilman AH. Susceptibility phase imaging with improved image contrast using moving window phase gradient fitting and minimal filtering. Journal of magnetic resonance imaging 2012;36(6):1460–9.

[28] Rasband WS. ImageJ. US National Institutes of Health, Bethesda, Maryland, USA, 1997-2011;.

[29] Roxburgh RH, Seaman SR, Masterman T, Hensiek AE, Sawcer SJ, Vukusic S, Achiti I, Confavreux C, Coustans M, le Page E, Edan G, McDonnell GV, Hawkins S, Trojano M, Liguori M, Cocco E, Marrosu MG, Tesser F, Leone MA, Weber A, Zipp F, Miterski B, Epplen JT, Oturai A, Sorensen PS, Celius EG, Lara NT, Montalban X, Villoslada P, Silva AM, Marta M, Leite I, Dubois B, Rubio J, Butzkueven H, Kilpatrick T, Mycko MP, Selmaj KW, Rio ME, Sa M, Salemi G, Savettieri G, Hillert J, Compston DA. Multiple Sclerosis Severity Score: using disability and disease duration to rate disease severity. Neurology 2005;64(7):1144–51.

[30] Cheah JH, Kim SF, Hester LD, Clancy KW, Patterson r S E, Papadopoulos V, Snyder SH. NMDA receptor-nitric oxide transmission mediates neuronal iron homeostasis via the GTPase Dexras1. Neuron 2006;51(4):431–40.

[31] Walsh AJ, Wilman AH. Susceptibility phase imaging with comparison to R2 mapping of iron-rich deep grey matter. Neuroimage 2011;57(2):452–61.

[32] Schafer A, Wharton S, Gowland P, Bowtell R. Using magnetic field simulation to study susceptibility-related phase contrast in gradient echo MRI. Neuroimage 2009;48(1):126–137.

[33] Du YP, Chu R, Hwang D, Brown MS, Kleinschmidt-DeMasters BK, Singel D, Simon JH. Fast multislice mapping of the myelin water fraction using multi-compartment analysis of T-2* decay at 3T: A preliminary postmortem study. Magnetic Resonance in Medicine 2007;58(5):865–870.

[34] Yablonskiy DA, Haacke EM. Theory of NMR signal behavior in magnetically inhomogeneous tissues: the static dephasing regime. Magnetic resonance in medicine 1994;32(6):749–63.

[35] Sati P, van Gelderen P, Silva AC, Reich DS, Merkle H, de Zwart JA, Duyn JH. Micro-compartment specific T relaxation in the brain. Neuroimage 2013;.

[36] Dalton CM, Chard DT, Davies GR, Miszkiel KA, Altmann DR, Fernando K, Plant GT, Thompson AJ, Miller DH. Early development of multiple sclerosis is associated with progressive grey matter atrophy in patients presenting with clinically isolated syndromes. Brain : a journal of neurology 2004;127:1101–1107.

[37] Bendfeldt K, Hofstetter L, Kuster P, Traud S, Mueller-Lenke N, Naegelin Y, Kappos L, Gass A, Nichols TE, Barkhof F, Vrenken H, Roosendaal SD, Geurts JJ, Radue EW, Borgwardt SJ. Longitudinal gray matter changes in multiple sclerosis-differential scanner and overall disease-related effects. Human brain mapping 2012;33(5):1225–45.

[38] Haacke EM, Miao Y, Liu M, Habib CA, Katkuri Y, Liu T, Yang Z, Lang Z, Hu J, Wu J. Correlation of putative iron content as represented by changes in R2* and phase with age in deep gray matter of healthy adults. J Magn Reson Imaging 2010;32(3):561–76.

[39] Rooney WD, Johnson G, Li X, Cohen ER, Kim SG, Ugurbil K, Springer J C S. Magnetic field and tissue dependencies of human brain longitudinal 1H2O relaxation in vivo. Magnetic resonance in medicine 2007;57(2):308–18.

Chapter 6

Conclusion

The main goals of this thesis were to investigate MRI methods which can evaluate brain iron, primarily in deep grey matter, and their application to multiple sclerosis. There was a substantial focus on gradient echo imaging using susceptibility phase imaging and R2* mapping.

Quantitative phase imaging is a relatively new MRI method, especially when used for iron quantification in deep grey matter. There are substantial obstacles to obtain consistent and accurate results as many variables can influence the measured phase. These include ROI placement, method of background phase removal, and location of background field measurement. The first study in this thesis addressed all three of these issues in an effort to establish a consistent and reliable method of measuring phase in deep grey matter using a standard high pass Hanning filter method. A simulation component and in vivo experiments explored different issues of quantitative phase imaging. A standard low pass Hanning filtered image, divided into the original complex image, with a larger frequency cutoff provides less phase suppression in large structures but preserves unwanted background fields from both distant air tissue interfaces and nearby deep grey matter. However this tradeoff must be weighed for different applications and suggestions are presented for deep grey matter imaging at 3T for standard SWI echo times. The best ROI placement was established in each structure along with the best filter strength to maximize the correlation to R2* mapping, which are different for each deep grey matter region. Baseline measurements are best obtained directly adjacent to structures, especially when weaker filters are used.

Background phase removal is required for quantitative measurements or for visual analysis of phase images. A new method was developed that improves upon standard high pass filtering. Unlike other background phase removal methods, it does not require unwrapping which can fail in areas of rapidly changing background phase or low SNR. The method is more accurate in simulation compared to the standard method, with only subtle differences from ideal phase. Furthermore, greater

contrast is obtained in images with lesions in MS and in deep grey matter.

Although some iron sensitive methods have been evaluated for measuring brain iron in postmortem studies, these methods have not been evaluated in MS. Furthermore, many postmortem studies use extracted, formalin fixed brain tissue which produces image contrast that does not closely resemble in vivo tissue contrast. Four MRI methods were applied to four postmortem patients with MS to evaluate the correlation between quantitative MRI and histologically determined iron content. Iron accounts for most of the variation in regression analysis indicating that it dominates contrast in deep grey matter in MS using high field MRI. However, iron within MS lesions does not consistently produce the same image contrast, possibly due to the relative contribution of myelin which is much greater in white matter compared to grey matter. A rim of $R_2^\star$ hyperintensity was only present in lesions which stained for iron, possibly indicating locally increased iron without substantial myelin pathology around lesion edges (Fig 1.15). However, this finding was not present in all lesions that stained for iron.

The temporal course of deep grey matter iron changes in RRMS were investigated in a two year longitudinal study using iron sensitive MRI. This type of analysis has not previously been conducted using quantitative MRI methods or using a high field system or in comparison to matched controls. The results indicate that iron sensitive MRI measurements over time are a strong predictor of baseline disease severity. These measurements correlate more strongly than other imaging markers of disease such as atrophy or T2 lesion volume. This is important as current clinical MRI is useful in establishing a diagnosis of MS but the role of following disease for prognostic value or treatment decisions is currently unclear. This finding could be an important first step in developing a new imaging biomarker of disease for evaluating individual patients.

6.1 Limitations

Current phase imaging has many shortcomings. A careful balance must be weighed between maximum structure contrast, extent of phase wrap removal, and pervasiveness of background field effects. While the first study explored potential tradeoffs of some these aspects, there could have been a further exploration of variables in phase imaging to more clearly establish a standard method for evaluating deep grey matter. Different territories could have been examined in both the simulation and in vivo including the caudate nucleus and thalamus. The simulation was relatively simplistic with homogeneous susceptibility assigned to each structure. The effects of heterogeneous susceptibility could have been examined, especially due to blood vessels or compartmentalization of tissue iron. Although angulation effects in phase

images have been tested in simulation [1], a more thorough analysis of these effects could have been explored, specifically for deep grey matter. Slight variations in head angle could produce changes both within structures and external field effects, both of which could substantially alter measured phase. Phantom experiments could have been performed as an intermediate step between simulation and in vivo imaging to examine more complicated aspects of deep grey matter iron quantification such as heterogeneous iron distribution [2] or the effects of partial volume on phase.

Although the gradient phase removal method showed improvement in terms of contrast and tissue visualization compared to the standard method, it was not evaluated against newer phase removal methods such as SHARP[3] and PDF[4]. The gradient removal method is somewhat heuristic in removing slow varying background fields while SHARP and PDF utilize a more mathematical approach based on Maxwell's equations of electromagnetism.

Aspects of the first two studies could have been taken one step further and been evaluated in conjunction with susceptibility mapping [5]. This method, in theory, should eliminate some complications of obtaining quantitative measurements from phase images such as background field effects and head angle effects. However, susceptibility mapping requires a phase image as an input with the background field removed yet a standardized, reliable method of phase removal has not been established. Different phase removal methods, including the standard method with different filter strength and the gradient method could have been tested to evaluate their usefulness in susceptibility mapping.

The postmortem study had numerous issues. Different sequence parameters were used in each subject making intersubject comparison more difficult as quantitative measurements may depend on such things as interecho spacing, and voxel size. The pathological sectioning was inconsistent as 3 brains were sectioned in the coronal orientation while one was sectioned in the axial orientation. MRI images had to be interpolated and rotated to precisely match the pathological specimens which could have introduced voxel averaging effects. Although Perls iron staining is specific for ferric iron, a different measure of iron could have been used in conjunction with staining for verification. Furthermore, optical density measurements have been used to quantify Perls iron staining but with slightly different methods. Therefore a direct comparison of the optical density method used to measure tissue iron would have been beneficial. Other tissue components can influence signal contrast and these should have been investigated. Major contributors could be myelin, calcium, and deoxyhemolobin [6]. A microscopic analysis with different staining and immunohistochemistry methods could have provided additional information about these components. Deoxyhemoglobin could have influenced the MRI measurements and would not have affected staining as blood is removed from vessels prior to staining.

Methods to overcome the blood contribution could have included imaging several days or weeks prior to patient death however there are ethical and logistical issues in dealing with patients with end stage MS. Alternatively, post processing methods could have been used to identify larger vessels and remove their contribution to MRI measurements.

There are several areas that could have been improved in the longitudinal assessment of deep grey matter in MS. Other imaging markers of disease could have been evaluated and compared to deep grey matter measurements. Atrophy is commonly used as a marker of disease in treatment studies and this was not assessed, mainly due to poor contrast and segmentation results with T1 weighted images at high field. Furthermore, T2 lesion volume measurements are a commonly used marker of disease severity and could have been compared in this study. The difference in head angle for individual subjects over time and between subjects is an issue for the standardization of 2D ROI placement and angle effects in phase images. 3D ROIs would make angle dependence less of an issue for R2* mapping however automatic alignment and segmentation software had only a 70% success rate. Susceptibility mapping could reduce the angle effect in phase images however a standard method has not been clearly established. EDSS is the most commonly used clinical measurement of disease severity however there are certain shortcomings. EDSS is mainly an indicator of physical disability and intrasubject variations over time in the absence of disease activity are common. Therefore determining a baseline EDSS that is not influenced by acute relapse is not standardized. Other aspects of disease such as cognition, fine motor skills, and ambulation, could have been quantitatively tested with cognitive batteries or MSFC testing.

High field MRI, which is more sensitive for iron in deep grey matter compared to lower field systems, was used in this thesis, therefore the results of this work may not be directly applicable to lower field clinical systems. Phase imaging should scale directly with field strength but CNR is decreased at lower field therefore acquisition and analysis may be slightly different. The sensitivity of transverse relaxometry to iron is directly proportional to field strength [7] making R2* mapping over three times less sensitive for iron at 1.5 T. Higher resolution analysis with high field MRI, could produce differences in quantitative measurements due to partial volume effects especially in smaller structures such as the substantia nigra.

6.2 Future Direction

Phase imaging has numerous drawbacks including dependency on object shape, rotation in a magnetic field, effects from other susceptibility sources, and background phase removal. Because of this, standardized methods of using phase for quantifica-

tion will require more thorough investigation. Alternatively, susceptibility mapping can remove many ill effects in phase imaging. However, susceptibility mapping techniques are far from being standardized and exhibit numerous problems. As a first step, susceptibility maps require a processed phase image with the background field removed. This is problematic as the results of susceptibility mapping greatly depend on the method of background phase removal. Furthermore, susceptibly mapping is an ill posed problem. Solutions include regularization methods [8], thresholding k-space [5], or acquiring multiple images with different head angles to B_0 [9]. In addition, there is considerable smoothing and ghosting in the final images based on the choice of parameters used which is moderately predictable in normal individuals but possibly not with concurrent pathology.

Although the implementation is heuristic, the gradient phase processing method is reliable and improves tissue contrast. Therefore, it could be used for imaging pathologies that are evident in SWI images to potentially improve diagnostic capabilities. These include intracranial hemorhage, vascular malformations, venous thrombosis, focal demyelination, infection, and neoplasm [10]. Since phase imaging is difficult to standardize and quantitative contrast depends on many variables, phase imaging will likely not be a prominent method in the future for quantifying iron in deep grey matter. Likely, R2* mapping and R2 mapping will be used for iron quantification because they have demonstrated high correlations to iron and have few variables in their implementation.

Although quantitative MRI methods show strong correlations to iron in deep grey matter, other biological components can influence quantitative measures. In order to distinguish other major contributions to quantitative MRI, histological analysis should be compared to MRI with the identification of cell types and abundance of cellular components such as proteins and lipids. It may be possible to separate some of these components with imaging methods; transverse relaxometry in combination with either phase imaging or susceptibility mapping could potentially distinguish the relative abundance of myelin and iron. Although this could aid in iron quantification in gray matter, this technique could be especially important in white matter MS lesions because analysis with a single method is unable to clearly identify iron status of lesions [12]. An accurate determination of lesion iron status could represent a new method of classifying lesions. Iron status within lesions could indicate stage or aggressiveness of lesions which could relate to local or overall disease activity. However, iron pathophysiology within MS lesions is unclear and could indicate damage with iron ladened macrophage infiltration or, alternatively, excess iron could indicate tissue repair with iron uptake during remeylination.

The macroscopic abundance of cells and cellular components affect quantitative MRI measurements, however there are several studies that investigate the mi-

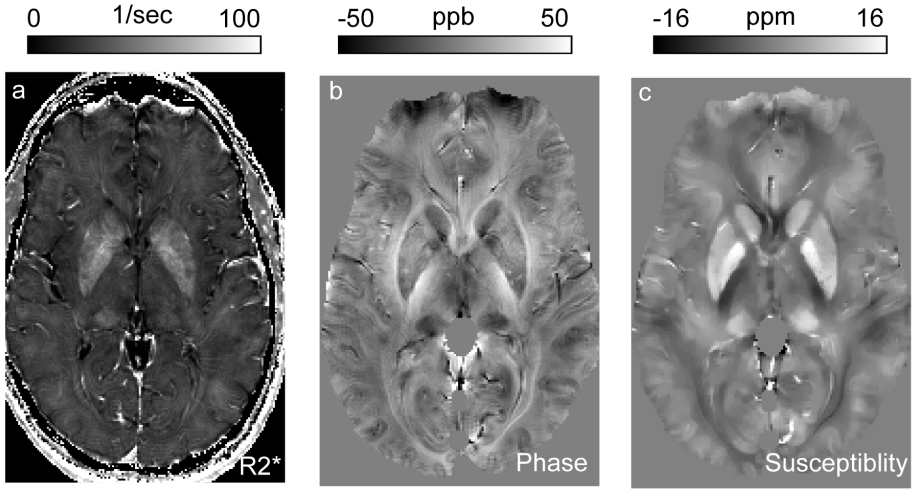

Figure 6.1: MRI images from a 45 year old healthy male of deep grey matter including the head of the caudate nucleus, globus pallidus, and putamen. a) R2* map b) phase image processed with SHARP and c) susceptibility map using L2 regularization. Hyperintense phase surrounds the putamen, globus pallidus and head of the caudate in the phase image due to external field effects from these structures. The outer surface of the brain is removed using the SHARP method. Tissue is smooth in the susceptibility map due to regularization parameters while the same regions are heterogeneous in the R2* map. Images obtained from a multi-echo gradient echo sequence using a 4.7T system [11].

crostructural properties of brain tissues and the effect on phase and relaxation. Different physical components of tissues have been modelled and related to MRI measurements either individually or in combination and include susceptibility anisotropy [13], microstuctural geometry [14], packing geometry [15]. Although much of the current research applies to highly organized white matter and cortical grey matter, correction methods could aid in iron measurements of deep grey matter. Throughout these studies, R2* generally does not vary substantially unless highly organized tissue is rotated more than 40 degrees which supports the use of R2* mapping for iron quantification in deep grey matter even with slight head angulation between subjects. However iron pathology in deep grey matter is not well understood and tissue organization might be critical if iron has certain microscopic distributions.

More basic science experiments are needed to investigate the issues and causes of iron misregulation in MS. Studies in this area are difficult because animal models of the disease mainly evaluate the acute inflammatory component of MS while iron accumulation may be related to other aspects such as neurodegeneration. Human tissue is difficult to obtain and is often from SPMS patients making results less applicable to the RRMS stage where iron changes are already apparent with MRI. Knowledge of normal iron physiology is lacking and is necessary to contextualize

iron in pathology [16]. Current research has focused on iron transporters on cell surfaces but iron transportation and utilization within and between cells is poorly understood.

Longitudinal analysis of deep grey matter in RRMS using iron sensitive MRI is a much better indicator of disease severity compared to single time point measurements. Further studies must be conducted to establish the best approach for longitudinal analysis and to examine how deep grey matter imaging relates to disease. Different stages of MS should be examined to clearly identify temporal iron changes. Particularly, the predictive value of these markers should be evaluated with early disease measurements compared to disease status at a later time. Currently, treatment efficacy is determined with absence of gadolinium enhancing MRI lesion, no activity with T2W MRI and no clinical history of relapse. This process can often take months or years to clearly identify non responders to treatment. Therefore, future studies should examine the effect of treatment on deep grey matter iron as current imaging methods for following response to treatment show poor utility.

Iron sensitive MRI of the deep grey matter could have many useful indications clinically. However current studies have only begun to explore the utility of these methods and their appropriate use in patients. Deep grey matter iron measured with MRI must be clearly established as a biomarker of disease which requires large multi-site clinical studies. In order for the imaging methods to be used clinically, they must be fast, available on clinical systems, and iron measurements techniques must be standardized.

Bibliography

[1] Schafer A, Wharton S, Gowland P, Bowtell R. Using magnetic field simulation to study susceptibility-related phase contrast in gradient echo MRI. Neuroimage 2009;48(1):126–137.

[2] Ye FQ, Martin WR, Allen PS. Estimation of brain iron in vivo by means of the interecho time dependence of image contrast. Magnetic resonance in medicine 1996;36(1):153–8.

[3] Schweser F, Deistung A, Lehr BW, Reichenbach JR. Quantitative imaging of intrinsic magnetic tissue properties using MRI signal phase: An approach to in vivo brain iron metabolism? Neuroimage 2011;54(4):2789–2807.

[4] Liu T, Khalidov I, de Rochefort L, Spincemaille P, Liu J, Tsiouris AJ, Wang Y. A novel background field removal method for MRI using projection onto dipole fields (PDF). NMR in biomedicine 2011;24(9):1129–36.

[5] Shmueli K, de Zwart JA, van Gelderen P, Li TQ, Dodd SJ, Duyn JH. Magnetic Susceptibility Mapping of Brain Tissue In Vivo Using MRI Phase Data. Magnetic Resonance in Medicine 2009;62(6):1510–1522.

[6] He X, Yablonskiy DA. Biophysical mechanisms of phase contrast in gradient echo MRI. Proc Natl Acad Sci U S A 2009;106(32):13558–63.

[7] Peters AM, Brookes MJ, Hoogenraad FG, Gowland PA, Francis ST, Morris PG, Bowtell R. T2* measurements in human brain at 1.5, 3 and 7 T. Magnetic resonance imaging 2007;25(6):748–53.

[8] de Rochefort L, Liu T, Kressler B, Liu J, Spincemaille P, Lebon V, Wu JL, Wang Y. Quantitative Susceptibility Map Reconstruction from MR Phase Data Using Bayesian Regularization: Validation and Application to Brain Imaging. Magnetic Resonance in Medicine 2010;63(1):194–206.

[9] Wharton S, Bowtell R. Whole-brain susceptibility mapping at high field: a comparison of multiple- and single-orientation methods. Neuroimage 2010; 53(2):515–25.

[10] Robinson RJ, Bhuta S. Susceptibility-weighted imaging of the brain: current utility and potential applications. Journal of neuroimaging 2011;21(4):e189–204.

[11] Sun H, Wilman A. Background field removal using spherical mean value filtering and Tikhonov regularization. Magnetic resonance in medicine 2013;(In press).

[12] Walsh A, Lebel R, Eissa A, Blevins G, Catz I, Lu J, Resch L, Johnson E, Emery D, Warren K, Wilman A. Multiple Sclerosis: Validation of MR Imaging for Quantification and Detection of Iron. Radiology 2013;(In Press).

[13] Li S, Wu Z, Lei J, An D, Haacke EM. Evaluation of Traumatic Subarachnoid Hemorrhage Using Susceptibility-Weighted Imaging. American Journal of Neuroradiology 2010;31(7):1302–1310.

[14] Yablonskiy DA, Haacke EM. Theory of NMR signal behavior in magnetically inhomogeneous tissues: the static dephasing regime. Magnetic resonance in medicine 1994;32(6):749–63.

[15] Chen WC, Foxley S, Miller KL. Detecting microstructural properties of white matter based on compartmentalization of magnetic susceptibility. Neuroimage 2013;70:1–9.

[16] Benarroch EE. Brain iron homeostasis and neurodegenerative disease. Neurology 2009;72(16):1436–40.